ELECTRON IRRADIATION INDUCED CHANGES OF THE ELECTRICAL TRANSPORT PROPERTIES OF GRAPHENE

A Dissertation

by

SUNG OH WOO

Submitted to the Office of Graduate and Professional Studies of
Texas A&M University
in partial fulfillment of the requirements for the degree of

DOCTOR OF PHILOSOPHY

Chair of Committee,	Winfried Teizer
Committee Members,	Joseph H. Ross Jr.
	Haiyan Wang
	Artem G. Abanov
Head of Department,	George R. Welch

August 2014

Major Subject: Physics

ABSTRACT

This research investigates the effect of electron irradiation on transport properties in graphene Field Effect Transistor (FET) devices. Upon irradiation, graphene is doped with electrons and adsorbs molecules by transfer of accumulated electrons in graphene to environmental molecules, resulting in the deterioration of transport properties. Molecules adsorbed after electron irradiation in ambient condition were observed by Atomic Force Microscopy (AFM). In-situ transport properties were measured in a vacuum after electron irradiation. In addition, hysteresis in the transport properties appeared as a result of electron irradiation. The origin of the hysteresis was investigated by exposing the electron beam irradiated graphene to ambient condition. As environmental molecules are adsorbed on graphene, the hysteresis disappears. In addition, annealing in a vacuum also removes the hysteresis. We conclude that the hysteresis is the result of polar adsorbates on graphene induced by electron irradiation.

In addition, the effect of electron irradiation on a PMMA (Poly Methyl Methacrylate)/Graphene bilayer was studied. We observed a deterioration of the electrical transport properties of a graphene FET. Prior to electron irradiation, we observed that the PMMA layer on graphene did not degrade the carrier transport of graphene but improved its electrical properties instead. As a result of the electron irradiation on the bilayer, defects could be observed by Raman spectroscopy. We

suggest that the degradation of the transport behavior originates from the binding of atoms or molecules generated by the PMMA backbone secession process.

ACKNOWLEDGEMENTS

I would like to thank my committee chair, Dr. Winfried Teizer, and my committee members, Dr. Joseph H. Ross Jr., Dr. Artem G. Abanov, and Dr. Haiyan Wang for their guidance and support throughout the course of this research.

Thanks also go to my friends, Dr. Hangil Lee and Dr. Kyoungwan Kim for their support and advice and the nanolab members, Jinseon Park, Wonbae Bang, Andrew Liao, Kelley T. Reaves, Esma Eryilmaz, Bin Yang, and Jaehyoung Son.

I also want to extend my gratitude to my mother in law and brother in law for standing by me and my wife. And, thanks to my brother, mother, and father for their encouragement and to my wife for her patience and love.

Finally, this dissertation is dedicated to my late father in law.

TABLE OF CONTENTS

Page

Page

LIST OF FIGURES

Page

CHAPTER I

INTRODUCTION

Graphene is a single layer of carbon atoms with a honeycomb network structure. Because it had originally been believed that this 2-Dimensional material cannot exist in the real world due to its instability [1], it had only been studied theoretically [2-5]. Experimental studies in graphene began with a breakthrough report, the successful isolation of graphene on SiO_2/Si substrates by mechanical exfoliation and fabrication of FET devices in 2004 [6] by Geim and Novoselov who won the Nobel prize in 2010 for their contributions to graphene research. Thanks to its extraordinary electronic, mechanical, optical, thermal, and chemical properties, graphene became a promising material in academia and industry.

Graphene exhibits high speed electronic performance. The mobility of electrons in suspended graphene reaches 200,000 ~ 600,000 cm^2/Vs at low temperature [7, 8], and the Fermi velocity of graphene is 10^6 m/s, which is the highest value ever known. At room temperature, the mobility of graphene on a SiO_2/Si substrate is revealed to be more than 10^4 cm^2/Vs, which is one or two orders of magnitude higher than the value for silicon.

Graphene is one of the strongest materials ever known [9]. Even when graphene contains crystallographic defects, its stiffness is equivalent to single crystalline graphene [10], indicating that polycrystalline graphene grown by CVD is as strong as the single

crystalline graphene. Another remarkable mechanical property of graphene is its tunable resonance frequency by applying gate voltage, which can be readout electrically. Tension of graphene membrane can be controlled by applying gate voltage, resulting in variation of resonance frequency from 20MHz to 80MHz. [11], which allows graphene a promising candidate for nano and micro meter-size scale electromechanical resonators. Because the resonance frequency responds to the externally applied force and mass attached to graphene, it can be applied as force detection sensors in AFM and mass detection sensors [11].

High thermal conductivity of graphene makes it more attractive to scientists and materials engineers than traditional materials. Heat management in integrated circuits (IC) has emerged as a critical issue in the miniaturization of electronic devices in IC chips because heat dissipated from highly integrated devices increases the operation temperature in ICs and degrades device performance. A material with high thermal conductivity is advantageous in suppressing temperature by transferring heat through the material. Room temperature thermal conductivity of graphene has been recorded up to 5300 $W/m \cdot K$, which is higher than copper and single-wall CNTs and is the highest value ever recorded [12-14].

Graphene is optically transparent. Optical transmittance of a graphene monolayer reaches 0.977 [15]. Although a monolayer of carbon atoms is transparent, graphene on SiO_2/Si substrates is visible by optical microscope with white light due to interference

effects. By selecting a proper thickness of the oxide layer on top of silicon, the absorption of graphene can be increased up to 0.15 [16].

Graphene interacts chemically with various atoms or molecules such as H, K, NO_2, NH_3, and OH [17-23] which modify its electronic properties. Molecules adsorbed on graphene act as electronic donors or acceptors, shifting the CNP (Charge Neutral Point or Dirac Point, V_D), which is the value of the gate voltage applied at minimum conductivity. In general, these molecules can be absorbed on graphene by exposing it to the relevant gases and desorbed by annealing. More importantly, the surface state of graphene can be sensed by FET operation, which allows for graphene to be operated as a gas sensor. In particular, graphene hydrogenation is of interest for hydrogen sensors or storage [22, 24]. Moreover, biological materials can be detected and the applications of graphene might be expanded to biology [25].

This dissertation is composed of seven chapters, starting with the introduction. In Chapter II, the theoretical background is described to introduce readers to the basic properties of graphene. The crystal structure is introduced, and the electronic energy band is calculated by the tight binding approximation. In addition, the fundamental theory of relativistic particles and Klein tunneling are added to explain massless Dirac fermions in graphene. Moreover, the principles of graphene FET operation and Boltzmann theory are presented to give an overall idea of electrical transport properties to readers.

Chapter III demonstrates the fabrication of graphene FET devices and characterization by AFM, Raman spectroscopy, and electrical transport measurement. The main experimental results are described in Chapter IV and V. Chapter IV contains the electrical transport properties of graphene after electron beam irradiation on a PMMA/graphene bilayer and subsequent removal of PMMA. In chapter V, the electrical transport properties of graphene in vacuum as affected by electron irradiation are described. The electrical transport properties of irradiated graphene after exposure to ambient air are shown and are related to surface adsorbates on graphene. Gate voltage hysteresis of graphene induced by electron beams irradiation is also described in this chapter. The last chapter will provide an overall guide to this thesis, a summary, and the conclusions. Further works and more issues related to this work will also be mentioned.

CHAPTER II

BACKGROUND

2.1 Crystal structure

Graphene is entirely composed of carbon atoms with an electronic structure $1s^2 2s^2 2p^2$. Carbon has six electrons and is a member of group IV in the periodic table. Carbon atoms in the graphene lattice have three sp hybrid electronic orbitals, which is the result of mixing of s and p orbitals into the same energy level. The way a carbon atom bonds with its neighbor is different from material to material. In diamond, four electrons per atomic carbons contribute to bond with four neighboring carbons. However, only three electrons contribute to covalent bonding with other nearby atoms in graphene and CNT. The electronic orbital of atomic carbon in graphene is shown in Figure 1 (a). A carbon in graphene has three in-plane sp^2 orbitals for covalent bonding and one out of plane p orbital which remains without bonding. The uncoupled p-orbital provides a free electron which contributes to conductivity by hopping.

Carbon atoms in graphene arrange themselves in a honeycomb lattice structure. Most of the extraordinary physical properties, such as the massless Dirac fermionic behavior, originate from the 2-Dimensional honeycomb sturcture which has two sub-lattices named A and B in the unit cell. The shaded area including A and B lattices in Figure 1(b) is the unit cell of graphene. The two vectors shown in equations 2.1 and 2.2, $\vec{a}_1$ and $\vec{a}_2$, are translational vectors, and a is the distance between nearest neighbors.

$$\vec{a}_1 = \frac{3a}{2}\hat{x} + \frac{\sqrt{3}a}{2}\hat{y} = \alpha\hat{x} + \beta\hat{y}, \tag{2.1}$$

$$\vec{a}_2 = \frac{3a}{2}\hat{x} - \frac{\sqrt{3}a}{2}\hat{y} = \alpha\hat{x} - \beta\hat{y}. \tag{2.2}$$

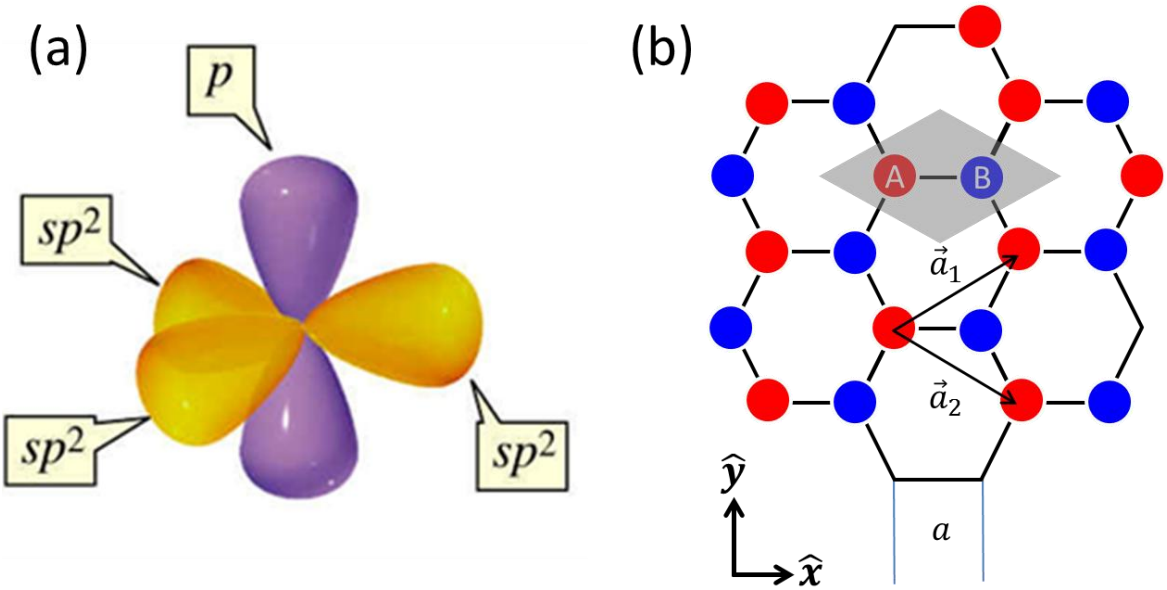

Figure 1 Crystal structure of graphene. (a) Electronic structure of the carbon atom in graphene. Three in-plane sp-hybridized orbitals and one out of plane p orbital are shown. (b) Honeycomb lattice structure with two sublattices labeled A and B. The unit cell is marked by a shadow.

2.2 Energy band structure[1] [26]

Graphene reveals a characteristic energy band with linear dispersion relation near K and K' in the momentum space. The unique electronic property stems from the existence of two sub-lattices in a unit cell, resulting in two non-equivalent valleys in reciprocal space. This extraordinary energy band of graphene can be calculated by tight binding theory, which is a theoretical method used to calculate band structure for tightly bound electrons on their atoms [27]. Because graphene has two sub-lattices in the unit cell, the wave function is a form of 2-component spinor, resulting in a 2 by 2 matrix Hamiltonian. The energy band can be calculated by solving the eigenvalue problem with the Hamiltonian in equation 2.3:

$$H(\vec{k}) = \begin{bmatrix} \epsilon & t \\ t & \epsilon \end{bmatrix} + \begin{bmatrix} 0 & 0 \\ t & 0 \end{bmatrix} e^{i\vec{k}\cdot\vec{a}1} + \begin{bmatrix} 0 & 0 \\ t & 0 \end{bmatrix} e^{i\vec{k}\cdot\vec{a}2} + \begin{bmatrix} 0 & t \\ 0 & 0 \end{bmatrix} e^{-i\vec{k}\cdot\vec{a}1} + \begin{bmatrix} 0 & t \\ 0 & 0 \end{bmatrix} e^{-i\vec{k}\cdot\vec{a}2}. \quad (2.3)$$

The first term in the equation 2.3 describes the hopping element within the unit cell, where ϵ and t are the on-site energy and the hopping energy between two lattices in the unit cell, respectively. The following four terms describe the hopping elements between the unit cell, which is the shadow area in Figure 2 (a), and the nearest neighbors marked with numbers from 1 to 4. The Hamiltonian can be simplified to a single 2 by 2

[1] Energy band calculation described in this section is based on the lecture (Reference 26) provided by Professor Supriyo Datta at Purdue University.

matrix, as shown in equation 2.4, where $h_0 = h_0(\vec{k}) = t(1 + e^{i\vec{k}\cdot\vec{a}_1} + e^{i\vec{k}\cdot\vec{a}_2})$ and ${h_0}^*$ is a complex conjugate of $h_0(\vec{k})$, and the eigenvalue equation results in 2.5.

$$H(\vec{k}) = \begin{bmatrix} \epsilon & {h_0}^* \\ h_0 & \epsilon \end{bmatrix}, \tag{2.4}$$

$$\begin{vmatrix} -E & {h_0}^* \\ h_0 & -E \end{vmatrix} = 0 \rightarrow E(\vec{k}) = \pm|\, h_0(\vec{k})|. \tag{2.5}$$

By combining equations 2.1, 2.2, and 2.5, and $\vec{k} = k_x\hat{x} + k_y\hat{y}$, $h_0(\vec{k})$ can be simplified as a function of the wave vector as shown in 2.6.

$$h_0(\vec{k}) = t\left(1 + 2e^{-i\alpha k_x}cos(\beta k_y)\right) \tag{2.6}$$

The expression of the energy in terms of the wave vector is derived as

$$E(\vec{k}) = |\, h_0(\vec{k})| = t\sqrt{1 + 4cos(\alpha k_x)cos(\alpha k_y) + \{4cos(\beta k_y)\}^2}. \tag{2.7}$$

In order to convert the Hamiltonian in terms of Pauli spin matrices, equation 2.6 can be expressed in bases of k_x and k_y near two valley points.

$$\begin{gathered} h_0 = Ck_x + D\, k_y, \\ C = \frac{\partial\, h_0}{\partial k_x}, D = \frac{\partial\, h_0}{\partial k_y}. \end{gathered} \tag{2.8}$$

At the valley K, the two coefficients C and D in equation 2.8 can be expressed in terms of lattice constant (a). Finally, the Hamiltonian can be expressed as a function of the wave vector as described in 2.9.

$$H = at\begin{bmatrix} 0 & -ik_x + k_y \\ ik_x + k_y & 0 \end{bmatrix}. \tag{2.9}$$

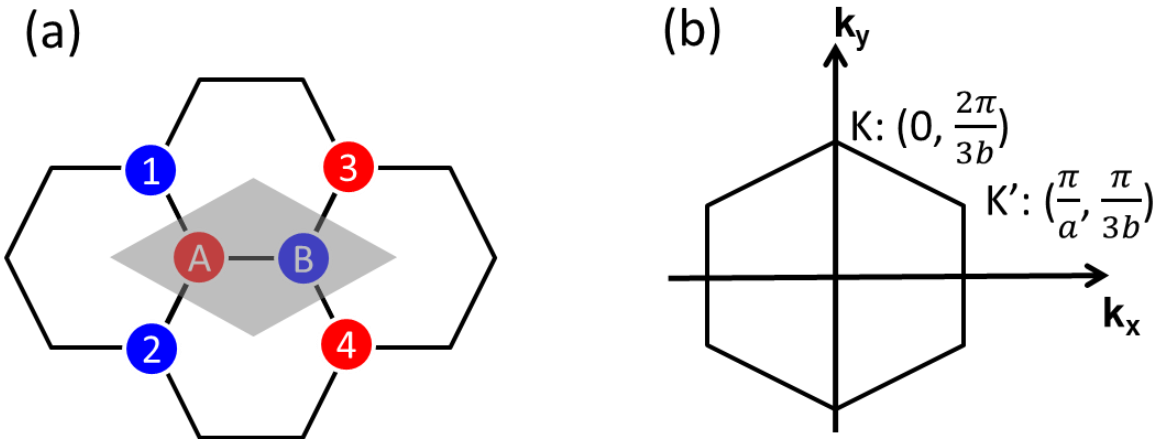

Figure 2 (a) Four neighboring lattices are marked by numbers around the unit cell of graphene to calculate the energy band structure. (b) Two non-equivalent valleys (K and K') are indicated in the First Brillion Zone.

2.3 Relativistic Dirac Fermions

The motion of classical particles is described by Newton's laws with energy being defined as $E = \frac{\vec{p}^2}{2m} + V$, where V is the potential energy of the particles. In quantum theory, the Schrödinger equation describes the equation of motion, where corresponding operators replace energy and momentum, $\vec{p} \to -i\hbar\nabla, E \to i\hbar\frac{\partial}{\partial t}$.

$$i\hbar\frac{\partial\psi}{\partial t} = \left[-\frac{\hbar^2}{2m}\nabla^2 + V\right]\psi \tag{2.10}$$

Here, $\psi = \psi(\vec{r}, t)$ is a wavefunction. On the other hand, the energy of relativistic free particles is described by $E^2 = m^2c^4 + \vec{p}^2c^2$, which transforms into the Klein Gordon equation:

$$-\hbar^2\frac{\partial^2\psi}{\partial t^2} = (-\hbar^2c^2\nabla^2 + m^2c^4)\psi, \tag{2.11}$$

However, in order to satisfy the fundamental assumption, *conservation of probability*, the second order time derivative equation 2.11 should be reduced to a first order differential equation [28]. Dirac first attempted to modify the Klein Gordon equation to describe the relativistic particles by introducing a matrix form as shown as 2.12 and 2.13.

$$E^2 = \begin{pmatrix} mc^2I & c\vec{\sigma}\cdot\vec{p} \\ c\vec{\sigma}\cdot\vec{p} & -mc^2I \end{pmatrix}\begin{pmatrix} mc^2I & c\vec{\sigma}\cdot\vec{p} \\ c\vec{\sigma}\cdot\vec{p} & -mc^2I \end{pmatrix} \tag{2.12}$$

$$E = \begin{pmatrix} mc^2I & c\vec{\sigma}\cdot\vec{p} \\ c\vec{\sigma}\cdot\vec{p} & -mc^2I \end{pmatrix}. \tag{2.13}$$

The energy square can be expressed as an inner product of two identical matrices, where $\vec{\sigma} = \begin{pmatrix} -\vec{\tau} & 0 \\ 0 & \vec{\tau} \end{pmatrix}$ is the Pauli matrix with its elements $\sigma_1 = \begin{pmatrix} 0 & 1 \\ 1 & 0 \end{pmatrix}$, $\sigma_2 = \begin{pmatrix} 0 & -i \\ i & 0 \end{pmatrix}$, and $\sigma_3 = \begin{pmatrix} 1 & 0 \\ 0 & -1 \end{pmatrix}$. Equation (2-11) describes the free relativistic particle, and the eigenstate of the eigenvalue equation, ψ, is a 4 component-spinor which is composed of $\psi_{+,\uparrow}(\vec{r}, t)$ $\psi_{+,\downarrow}(\vec{r}, t)$, $\psi_{-,\uparrow}(\vec{r}, t)$, and $\psi_{-,\downarrow}(\vec{r}, t)$. The eigenvalues of 2.10

can be positive or negative values. The subscripts '+' and '−' indicate positive and negative eigenenergies, and the arrows '↑' and '↓' indicate spin up and down, respectively. In this theory, $\psi_{+,\uparrow}(\vec{r},t)$ and $\psi_{+,\downarrow}(\vec{r},t)$describe spin ½ fermions, and $\psi_{-,\uparrow}(\vec{r},t)$, and $\psi_{-,\downarrow}(\vec{r},t)$ are anti-fermions. For the massless Dirac fermions, the Hamiltonian 2.13 transforms into 2.14 by removing mass,

$$H = \begin{pmatrix} 0 & c\vec{\sigma}\cdot\vec{p} \\ c\vec{\sigma}\cdot\vec{p} & 0 \end{pmatrix}. \tag{2.14}$$

Under the condition $c \to v_f$ and $p_z \to 0$, the expression 2.14 represents the Hamiltonian of 2-D massless Dirac fermions which is the same form as 2.9. Considering 2.9 and 2.14, the hopping energy can be determined as $t = \frac{v_f \hbar}{a}$, and the Hamiltonian can be written as equation 2.15.

$$H = \hbar v_f \vec{\sigma}\cdot\vec{k}. \tag{2.15}$$

2.4 Klein tunneling

In classical mechanics, a particle is confined when its energy is less than a potential barrier height (V_0). In non-relativistic quantum mechanics, there is a chance for a particle to transit through the classically forbidden region by quantum tunneling. In this process, the transmission probability (T) is determined mainly by the potential barrier height and width [29]. For a Dirac particle, however, T weakly depends on V_0 and even approaches unity while increasing the potential barrier height [30, 31]. This

relativistic process is referred to as Klein tunneling and is attributed to the fact that a strong potential barrier is repulsive for electrons but attractive for holes.

Outside the barrier, the Fermi energy lies above the origin and an electron approaches the barrier without obstruction. Inside the potential barrier, the Fermi energy is pulled down to the negative side as shown in Figure 3, but it still remains aligned with the Fermi energy levels of electrons on both ends.

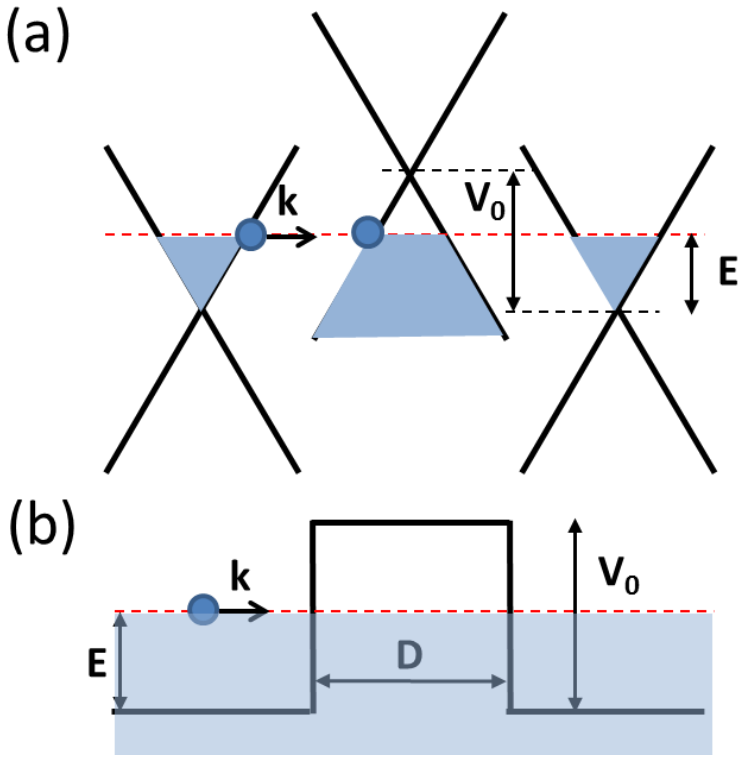

Figure 3 Schematic diagram of a Klein tunneling junction. (a) Fermi energy levels are dotted line in (a) and (b). (a) Energy bands of graphene corresponding to outside and inside of a potential barrier in (b). (b) Square potential barrier of width D and height V_0.

The moment the electron arrives at the boundary of the barrier, the hole, instead of the electron, propagates in the barrier. In this respect, both electrons and holes, together, contribute to conduction across the high potential barrier. Thanks to the Klein tunneling process, electrical carriers in graphene contribute to the conduction even in the case of an extremely high potential barrier. This effect was further confirmed by solving the transmission coefficent for graphene in n-p junction problems [32, 33].

2.5 Electrical transport properties of graphene

2.5.1 Carrier conduction behavior near the Dirac point

In normal metals, the conductivity goes to zero as the carrier density approaches zero. If graphene obeys the same rules as normal metals, the conductivity of graphene at V_D should be zero. Many experimental results, however, have shown that the conductivity in graphene did not drop to zero at V_D, which is the gate voltage value leading the carrier concentration to zero, but approaches the universal minimum conductivity [6, 7, 30, 34, 35].

In order to investigate this unusual electronic behavior theoretically, a simple graphene FET device model was introduced [36]. It has a graphene strip and two metal electrodes, one at each end, which are considered infinite potential barriers [36]. In this configuration, the conduction problem can be replaced with a p-n-p Klein tunneling junction problem as shown in Figure 4.

The solution of the Klein tunneling junction problem can be obtained by solving the Dirac equation with boundary conditions in equation 2.16 [36, 37].

$$\left[vp_x\tau_x + vp_y\tau_y + v^2M(y)\tau_z + \mu(x)\right]\psi(r) = \epsilon\psi(r),$$
$$\psi_1|_{y=0} = \psi_2|_{y=0}, \psi_1|_{y=W} = -\psi_2|_{y=W}. \tag{2.16}$$

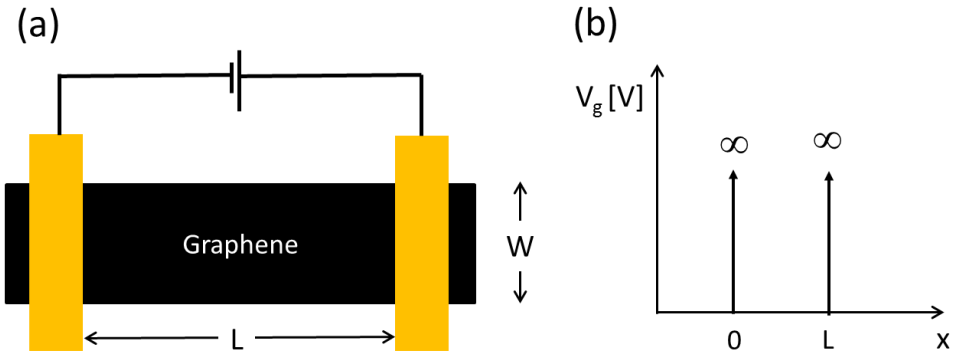

Figure 4 (a) Schematic diagram of a graphene FET device. The graphene strip is contacted by two metal electrodes. The width and length of the device are W and L, respectively. (b) A diagram of potential barriers of the graphene device shown in (a) is displayed. The potential between two electrodes (0<X<L) is μ, and otherwise it is infinite.

The resultant conductivity is expressed as in equation 2.17.

$$\sigma = \frac{L}{W}\frac{4e^2}{h}\sum_{n=1}^{N} T_n \tag{2.17}$$

Here, ψ is a two-component wavefunction (ψ_1, ψ_2), which is originated from two sub-lattice sites A and B in the unit cell, τ_i is Pauli matrix component, μ is the potential energy, and v is the velocity of a Dirac electron. The mass M(y) is zero in the

graphene strip region and is considered as ∞ outside of graphene strip. In equation 2.17, T_n is the transmission probability through the barrier and n is the conduction channel mode. Under the condition, N>>1 and W>>L, the conductivity (2-16) reduces to σ_{min} as shown in equation 2.18.

$$\sigma_{min} = \frac{4e^2}{\pi h} \tag{2.18}$$

2.5.2 Carrier conduction behaviors far from the Dirac point

Far from the V_D, electrical transport properties can be described by the semi-classical Boltzmann theory [27, 38-43]. In this theory, the rate of collision is described by partial derivatives of the distribution function (f) with respect to time, position, and momentum as described in equation 2.19.

$$\left(\frac{df}{dt}\right)_{coll} = \frac{\partial f}{\partial t} + \vec{v} \cdot \frac{\partial f}{\partial \vec{r}} + \vec{F} \cdot \frac{\partial f}{\partial \vec{p}} \tag{2.19}$$

To calculate the conductivity, the relaxation time (τ) is required, which can be derived from the equation 2.19 with the three conditions described below. Conditions 2.20) and 2.21 imply near equilibrium and a steady state of the distribution function, respectively. If no magnetic field is applied, the force is expressed only a function of an electric field, as shown in equation 2.22.

$$\frac{\partial f}{\partial \vec{r}} \approx \frac{\partial f_0}{\partial \vec{r}}, \frac{\partial f}{\partial \vec{p}} \approx \frac{\partial f_0}{\partial \vec{p}}. \tag{2.20}$$

$$\frac{\partial f}{\partial t} \to 0. \tag{2.21}$$

$$\vec{F} \to -\mathrm{e}\vec{E}. \tag{2.22}$$

Under the three conditions, the relaxation time can be approximated as shown in equation 2.23,

$$-\frac{\delta f}{\tau} = \vec{v} \cdot \frac{\partial f_0}{\partial \vec{r}} - e\vec{E} \cdot \frac{\partial f_0}{\partial \vec{p}}. \tag{2.23}$$

Here, f is the Fermi-Dirac distribution function, and f_0 is the Fermi-Dirac function at zero Kelvin. After some algebra, δf can be derived as the following equation,

$$\delta f \ = -e\tau\left(-\frac{\partial f_0}{\partial E}\right)\vec{v} \cdot \vec{E}. \tag{2.24}$$

Plugging equation 2.24 into the current density equation 2.25, the conductivity far from the V_D can be expressed as a function of a charge concentration and a relaxation time as shown in equation 2.26.

$$\vec{j} = \frac{1}{A}\sum_{k} -ev(\delta f) = \sigma\vec{E} \tag{2.25}$$

$$\boldsymbol{\sigma} = \frac{v_f \tau e^2}{\hbar}\sqrt{\frac{n}{\pi}} = \frac{n\tau e^2}{m^*} \tag{2.26}$$

Equation 2.26 results in the Drude model, where $k = \sqrt{n\pi}$ and $m^* = \hbar k / v_f$.

In general, the semi-classical theory of conduction describes the electronic collision as random and uncorrelated events. The Relaxation Time Approximation (RTA)

can be derived from those two assumptions. This approximation assumes that the non-equilibrium distribution function has no effect either on the rate of collisions or on the distribution function prior to the collision. However, the rate of collisions critically depends on the distribution function before the collision. Furthermore, the RTA overlooks the fact that the nature of the scattering strongly depends on the non-equilibrium distribution function. Therefore, the RTA is valid only when the collision process is clearly of little consequence. For example, in the case of high intensity or high frequency of external electric field approximations, conductivity can be derived by the RTA [27]. When the scattering process becomes dominant, the specific scattering mechanism should be considered when calculating the scattering probability. The total collision rate is described by the equation 2.27 [27],

$$\left(\frac{df(\boldsymbol{k})}{dt}\right)_{coll} = -\int d\boldsymbol{k}' \{W_{\boldsymbol{k},\boldsymbol{k}'} f(\boldsymbol{k})[1 - f(\boldsymbol{k}')] - W_{\boldsymbol{k}',\boldsymbol{k}} f(\boldsymbol{k}')[1 - f(\boldsymbol{k})], \tag{2.27}$$

where $W_{\boldsymbol{k},\boldsymbol{k}'}$ is a quantity related to the scattering probability and depends on the particular scattering mechanism. Again, the scattering rate can be related to the RTA and the relaxation time can be calculated as shown in equation 2.28,

$$\left(\frac{df(\boldsymbol{k})}{dt}\right)_{coll} = -\frac{\delta f}{\tau(\epsilon_k)}. \tag{2.28}$$

In summary, the conductivity in specific cases should be calculated from equations 2.25, 2.27, and 2.28.

2.5.3 Various carrier conduction theories far from the Dirac point

The electrical transport properties of graphene far from V_D are not yet clearly understood. As shown in equation 2.28, the transport mechanism depends on the scattering of carriers and varies according to the type of scattering.

The first theoretical calculation of the conductivity of graphene in this region was undertaken by Shon et al. [44]. In their calculation, the conductivity which is dominated by short-range disorder was constant. The calculation revealed that the conductivity did not depend on the concentration of the disorder but did depend on the scattering length of scatterers as shown in 2.29, indicating that it is constant when a certain type of scatterer is fixed.

$$\boldsymbol{\sigma} = \frac{Ae^2}{h\pi^2} \tag{2.29}$$

In equation 2.29, a coefficient (A) is a dimensionless parameter characterizing the scattering length.

However, recent experimental results have shown different conduction behaviors in that the conductivity is linearly proportional to the carrier density [45, 46]. To explain a linear dependence of the conductivity on the carrier concentration, long-range disorder was introduced while successfully elucidating the conduction behavior [47-52]. The final result of the conductivity is described by equation (2.30),

$$\boldsymbol{\sigma} = \frac{Ce^2}{h}\left|\frac{n}{n_i}\right|, \tag{2.30}$$

where C is the product of mobility and density, a constant related to the scattering strength, and n_i is the impurity concentration. Equation 2.30 also predicts that the mobility is inversely proportional to the concentration of the impurity, n_i, which is in agreement with experimental results [46, 53] of linear dependence of the conductivity on carrier concentration.

Recently, equation 2.30 was modified to 2.31 by taking into account electron-hole correlations [54] or by including the current-current correlation function [55] for calculating the conductivity, which is consistent with the minimum conductivity revealed in experiments.

$$\boldsymbol{\sigma} = \frac{Ce^2}{h}\left|\frac{n}{n_i}\right| + \boldsymbol{\sigma}_{res} \tag{2.31}$$

Although equation 2.31 sufficiently explains the transport properties far from V_D when charged impurities dominate, it is not the best theory under other circumstances, such as when defects are generated by ion irradiation. As a result of Ar^+ ion irradiation on graphene, defects, for example single and multiple vacancies, are generated, and the conduction mechanism is better explained by the strong disorder model [56]:

$$\sigma = \frac{4e^2}{h}\frac{n}{n_i}(ln\sqrt{n\pi}R_0)^2, \tag{2.32}$$

where R_0 is the radius and n_i is the concentration of the disorder. Adam et al. [57] considered a Gaussian potential varying smoothly on the scale of the lattice constant and predicted a dependence of σ on $n^{3/2}$, but so far no corresponding experimental result has

been reported. Currently, the conduction mechanism far from the V_D can be explained mainly by long-range coulomb scattering due to charge impurities. In order to explain the electrical transport properties dominated by defects, which are induced by ion irradiation, the equation 2.32 is a better model than the equation 2.31. The theory from [57] might work for conduction induced by other kind of defects. It is important to realize that different extrinsic properties affect the transport of charge carriers in different ways.

2.6 Irradiation of graphene by electron beams

Irradiation experiments of graphene with various radiation sources such as ions, photons, and electrons have been conducted extensively because irradiating graphene changes its chemical, physical, and surface properties.

First of all, irradiation experiments with various light sources have been conducted. By exposing graphene to energetic UV, its electronic properties, chemical doping, and surface morphology are modified. The resistance of graphene due to the UV exposure is degraded [58], and the work function of the graphene FET device can be tuned [59]. In addition, the chemical doping behavior of graphene can also be changed by UV exposure [60]. High energy photons physically damage graphene. For example, a multi-layered graphene film was damaged by exposure to a 10keV X-ray source [61]. As a result of the photon irradiation, the surface layer of graphene was peeled off as shown by optical microscopy. In other experiments, graphene has been oxidized as a result of 10keV and 1MeV X-ray exposure [61, 62].

Heavy ions are another irradiation source that can damage graphene. Previously, artificially induced structural defects had been studied by exposing graphene, carbon nanotubes or graphite to energetic ions or electrons. As 500eV Ne^+ ions were irradiated on graphene, a Raman 'D' band, a signature of structural defects, appeared [63]. As a result of the structural defects induced by the ion irradiation, the electrical transport properties were degraded [63]. An image of a single defect created by Ar^+ ion bombardment on graphene [64] and on a graphite surface were reported [65].

Interaction of graphene with energetic electron beams is another interesting research field, which has been studied intensively. Because there is a great chance of graphene to be exposed to electron beams during fabrication and characterization processes by EBL, SEM, or TEM. A TEM image of a point defect on a graphene layer was first reported with electron energy of 120keV [66]. The theoretically calculated threshold energy for carbon atom ejection from graphene is around 86keV [67]. In a recent experiment, however, single and multiple defects as a result of 80keV-electron irradiation on graphene were observed by TEM [68]. According to their experiment, focused electron beams with a slightly lower threshold energy generated single and multiple defects by increasing the electron dosage. In another experiment with 60keV electron beam energy, a reduction in width of a graphene nano ribbon was observed [69].

The idea that defects can be generated by energetic electrons with energy around or higher than the knock-on acceleration voltage is proven by experiments [66] and

theory [67]. However, the effect of electron irradiation on graphene is controversial. Electrical transport properties of graphene on SiO_2/Si are modified after irradiation with electron beams with energy less than 30keV, which is far less than the threshold energy of displacement of carbon atoms. Although no direct experimental observation in atomic level has been reported yet, low energy electron beams (<30keV) generate defects in graphene, resulting in a deterioration of the transport properties. With regard to electron irradiation on graphene with electron beam energy less than 30keV, there have been a number of experimental and theoretical advances [70-85]. According to the theoretical and experimental results so far reported, the minimum threshold energy of electrons to eject a carbon atom in graphene is around 80keV. Irradiation of electron beams with energy less than 30keV revealed a Raman 'D' band, which is a signal that graphene contains defects, even though it is not clear yet whether the signals indicate atomic displacement of carbon or other types of defects such as molecular absorption. Recently, Xu et al. [70] showed that not only carbon atoms but also the entire graphene device can be etched by 10keV electron irradiation by AES. In two irradiation experiments with less electron energy than the threshold energy [68, 70], a removal of atomic carbon was observed by increasing the electron dosage. However, a relationship between the electron energy and the dosage leading to eject the carbon atoms from the lattices has not been studied yet.

CHAPTER III

GRAPHENE DEVICE FABRICATION AND CHARACTERIZATION

3.1 Graphene device fabrication

The graphene flakes were transferred from the 'ZYA' grade HOPG onto SiO_2/Si substrates with pre-patterned markers by mechanical exfoliation [6, 35]. The so called 'scotch tape' method was used, which was the technique that Geim and Novoselov first used to fabricate a graphene FET device. They won the Nobel Prize in 2010 for their realization of a real 2D graphene device. Even though graphene flakes are transparent, the contrast of the graphene strongly depends on the thickness of the oxide layer. In order to maximize the visibility of graphene flakes, a 285nm-thick thermally grown oxide layer was employed [16] as a gate dielectric material. For back gate operation, heavily doped silicon wafers were selected. When graphene flakes are transferred onto substrates, multiple layers of graphene stacks or graphite can be screened by optical microscopy. Finally, a single layer of graphene is identified by Raman spectroscopy. Electrodes were defined by EBL, followed by thermal evaporation of Cr and Au. Searching for a perfectly isolated graphene is not always straightforward since other unwanted flakes or thick graphite interferes with the graphene FET device. In that case, graphene or graphite that interferes with device fabrication can be selectively removed by Reactive Ion Etch (RIE) by using a PMMA mask.

3.1.1 A reference marker pattern

The first step to fabricate graphene FET devices is to make reference patterns on substrates prior to transferring graphene flakes from the HOPG. To fabricate the electrodes on graphene for transport measurements, pre-patterned markers are necessary in order to define the relative position of graphene flakes with respect to the reference pattern. It is because they are not visible during the FET device fabrication process. In addition, during electron beam lithography process, as an electron beam approaches the graphene flakes to find them, PMMA around it should be damaged, disrupting the electrode fabrication process. Therefore, to prevent unintended exposure of an electron beam on PMMA, the reference patterns are required. In particular, the pre-patterned reference marker structures serve as x and y axes in the substrates, which are necessary to calculate the position in the optical coordinate system.

A schematic diagram of the reference pattern on substrates, and individual geometry are shown in Figure 5. The 1.5mm square area of the reference pattern was centered on substrates as displayed in Figure 5 (a). Pre-patterned markers were created in 1.5mm square area with coordinate numbers to avoid confusion during the EBL process as shown in Figure 5 (b) and (c). After transferring graphene flakes, the only ones distributed near the reference patterns could be selected for device fabrication. The optimized marker pattern reveals 150μm inter-distance and 20μm width of each marker. The entire reference pattern could be written by EBL followed by successive evaporation of Cr and Au.

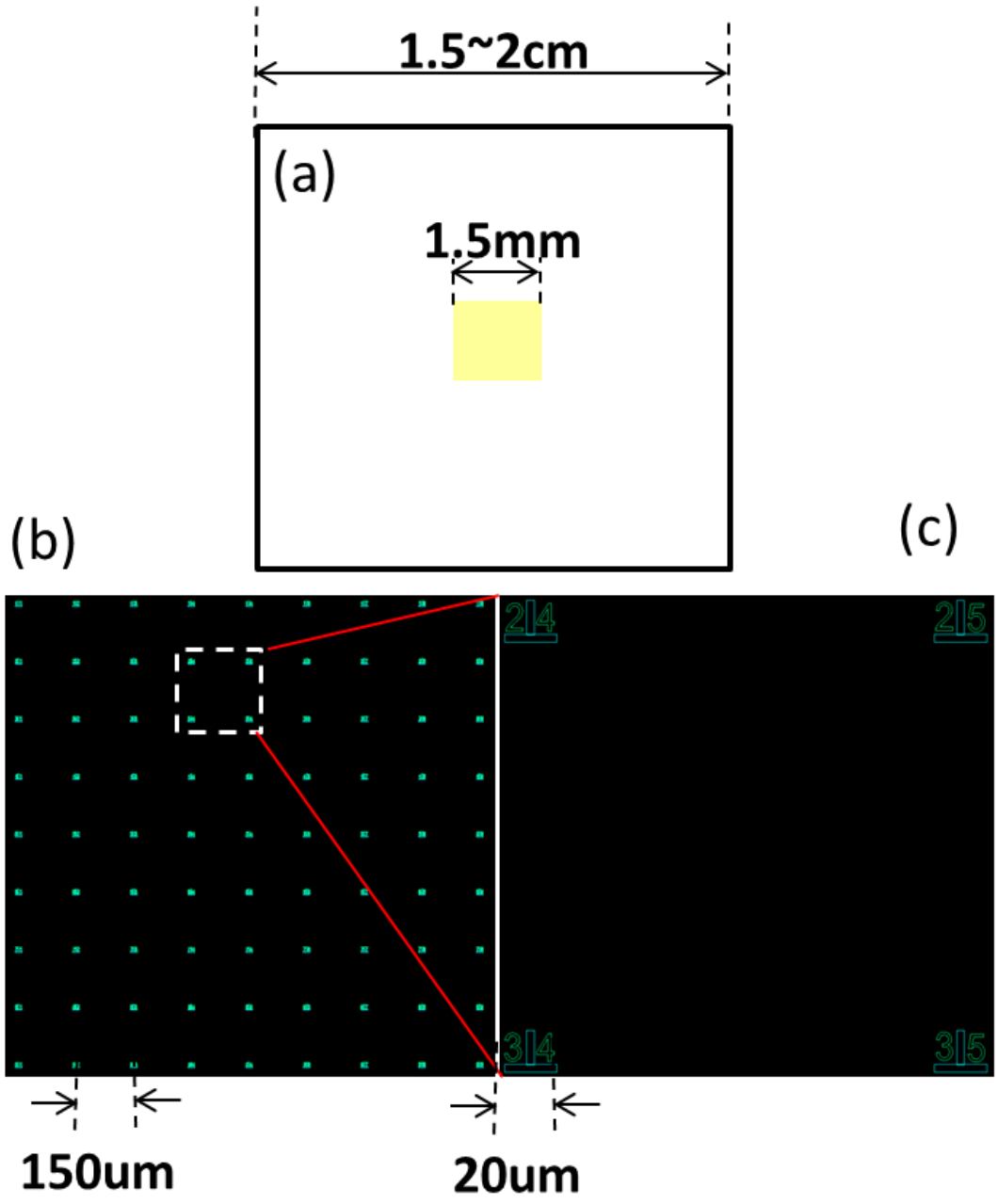

Figure 5 Schematic diagrams of the reference patterns on substrate. (a) The reference patterns with area of 1.5*1.5mm^2 are fabricated on the center of SiO_2/Si substrates. (b) The patterned area is composed of 9 by 9 arrays with spacing 150μm. (c) Individual array is composed of two perpendicular bars with coordinate numbers.

In the usual EBL process, alignment of an electron beam and focusing on the PMMA surface are critical to make fine structures. In particular, the quality of the pattern written by the EBL depends critically on a good focus. To gain a good focus on the surface, a scratch mark from edge of the substrate to center has been used because the actual EBL pattern can be written near the scratch after focusing on the scratch.

Instead of traditional focusing process, which requires the artificial scratch mark, in this graphene project, focusing on PMMA surface was done at the edge of substrates. Once a contamination spot, which is a signature of good focusing on PMMA surface, was confirmed at the edge of the substrate, we operated the EBL stage to move to the center of the substrate with the electron beam turned off. Then, the testing spot was made by adjusting the focusing knob. Because the center of the substrate is far from the edge, the electron beam loses its focus, which should be adjusted on the center of the substrate again. However, at that moment, only fine adjustment was enough to recover the focus. The electron beam current and dosage during e-beam writing were 500pA and 300μC/cm^2, respectively. When the EBL process was successful, the pattern defined by the EBL was metallized by thermal evaporation. .

3.1.2 Graphene flakes transfer

Graphene flakes were transferred from the HOPG onto substrates that have array of pre-patterned markers using a sticky tape. In order to peel off the graphene from the HOPG, the sticky side of the tape was put on HOPG. Then, a large amount of graphene was taken to the tape. Graphene or graphite on the tape could be removed by putting the

tape on the other tape. This process had been repeated until a proper amount of graphene remained on the tape as shown in Figure 6 (a).

In order to transfer graphene from the tape onto SiO_2/Si substrates, the sticky side of the tape was put down on the substrate as shown in Figure 6 (b). When the tape was removed after rubbing the tape gently, various graphene or multi-layer of graphene flakes were transferred and remained on the substrates as shown in Figure 6 (c).

After removal of the tape, substrates were cleaned with acetone, IPA, and DI water to remove residue of sticky materials. Because the contrast of the single layer of graphene on SiO_2 (285nm) reaches up to 0.15 [16], a single layer graphene flake could be searched by an optical microscope. Candidates of single layer of graphene flakes could be identified using Raman spectroscopy [86].

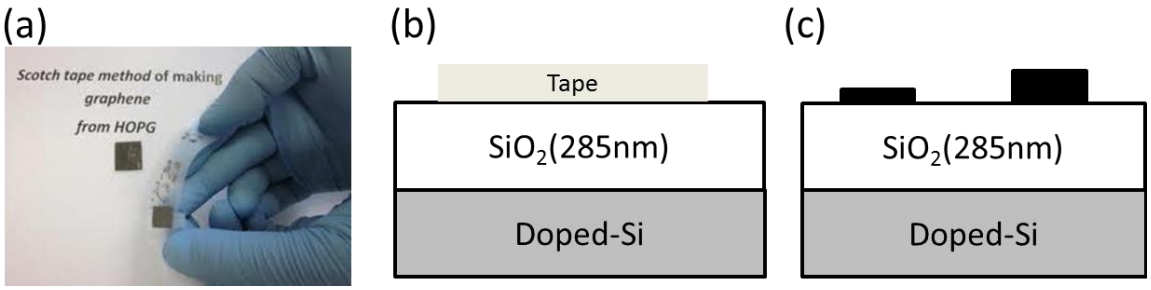

Figure 6 Graphene transfer from HOPG onto substrates. (a) Peeling off the bulk graphite from HOPG by the sticky tape. (b) Transferring graphene or graphite from the tape to substrate by rubbing gently on the tape. (c) Various single and few layers of graphene remain on substrates after removing the tape.

3.1.3 Electrical contact pads by electron beam lithography

Electrical contact pads were defined by EBL, which is an important tool to fabricate micron or nanometer scale devices. In addition, it provides fast way to make complex and small patterns with high reliability [87]. In addition to those advantages, the EBL process makes it possible to do lithography without any mask while a photolithography process requires a mask. Another great advantage of the EBL is that it is simple to change pattern, which is critically important to fabricate graphene devices by the mechanical exfoliation technique because graphene flakes are randomly distributed through substrates.

In order to define electrical contact pads for graphene devices, reference patterns were defined prior to the contact pads fabrication process. The reference pattern is required to define relative location of a graphene flake with respect to the reference marker to avoid damage of PMMA during the EBL process. Prior to the EBL process after transferring graphene flake onto substrates, SEM pictures of graphene near the reference pattern were obtained to find the relative location of graphene with respect to the reference pattern. An individual reference pattern is composed of two perpendicular rectangles to define the x and y axis within the substrate as shown in Figure 7.

During the EBL process, there should be two different coordinate systems. A schematic diagram of the relationship between two coordinate systems is shown in Figure 7. One is the ‘Stage axis’ that defines a rectangular coordinate system. In this coordinate system, the x and y axes are aligned to the stage movement axes. The other is

the ‘Optical axis’ that is defined by the reference pattern as shown in Figure 7. Because the stage of EBL moves along the ‘Stage axis’, the position of the graphene flake with respect to the reference in the ‘optical axis’ coordinate system should be transformed to the new coordinate, r(x, y), in the ‘stage axis’ coordination by equation 3.1 and 3.2.

$$x = r\cos(\theta + \theta') \tag{3.1}$$

$$y = r\sin(\theta + \theta') \tag{3.2}$$

Here, θ is an angle between two different coordinate systems, and θ' is an angle from the x axis to the graphene flake in polar coordinate system in the ‘optical axis’ as described in Figure 7. Both angles are obtained by equation 3.3.

$$\theta = \tan^{-1}\frac{y_2 - y_1}{x_2 - x_1}$$
$$\theta' = \tan^{-1}\frac{y}{x} \tag{3.3}$$

Here, (x_1, y_1) and (x_2, y_2) are two points at corners in the reference patterned as marked in Figure 7 and can be obtained from the controller of the EBL stage. Once the location of the graphene in the ‘Stage axis’ is found, contact pads can be defined.

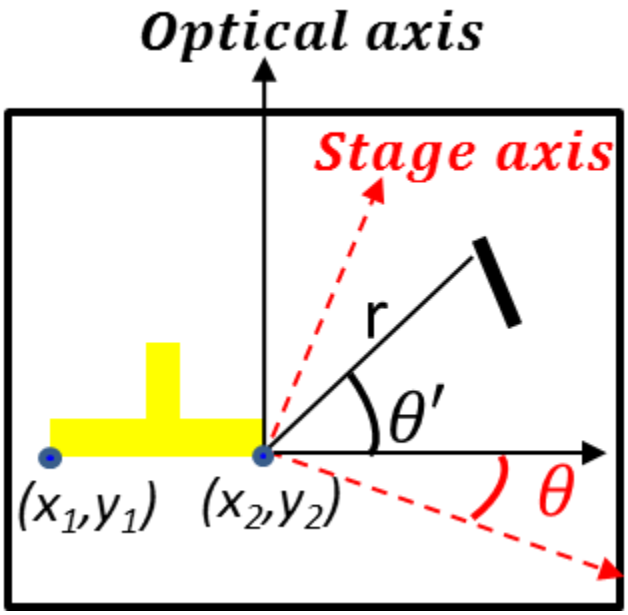

Figure 7 Geometry of graphene flake with respect to an individual marker after transferring of graphene from HOPG onto the substrate. Optical axes (black arrows) are defined within the substrate to locate the graphene flake relative to the reference. Stage axes (red dotted arrows) are defined along the stage movement directions.

At a result of the EBL process, electrodes on graphene could be defined as shown in Figure 8 (a). In general, the EBL process allows making patterns in the area less than 2mm square area. Because the electrode patterns defined by EBL were not large enough to make contact for wires, they were enlarged by an additional EBL process prior to metallization. In the second EBL process, additional extension legs and large contact pads to bond wires for transport measurements were patterned as shown in Figure 8 (b). Fabrication of graphene FET devices can be competed after metal deposition and lift off process.

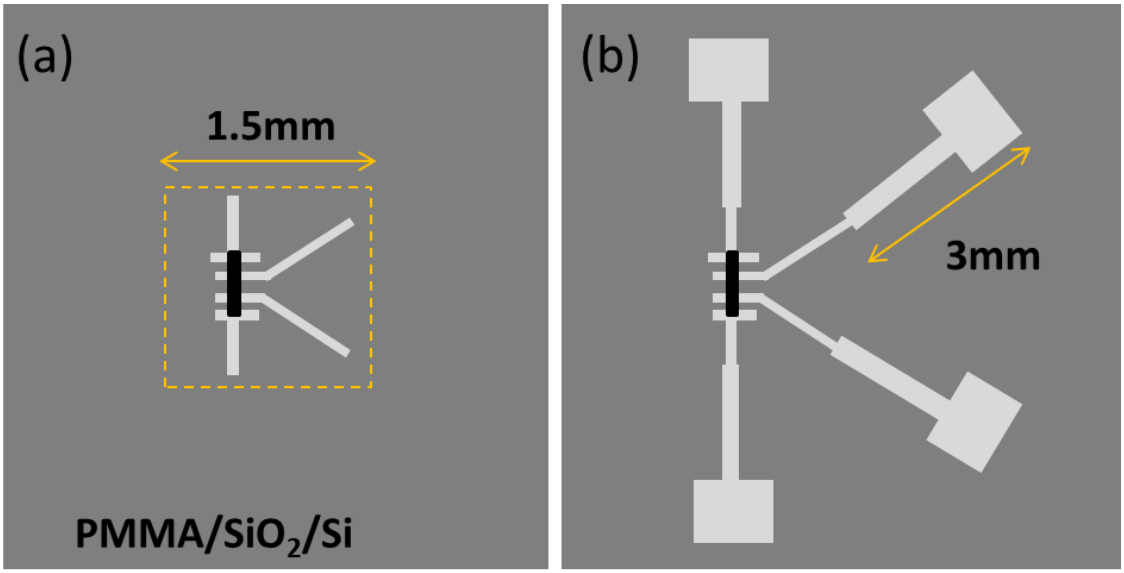

Figure 8 Electrical electrodes defined on graphene by EBL after development but before metallization. (a) Electrodes patterns as a result of the first E-beam lithography. The biggest patterned area by the EBL is 1.5mm square. (b) Extensions and large contact pads with additional EBL processes.

3.1.4 Graphene etch

Graphene flakes are distributed through substrates when graphene is transferred from the HOPG by the mechanical exfoliation method. In other words, it is difficult not only to control specific locations of graphene flakes but also to find perfectly isolated graphene flakes near the pre-patterned markers. To enhance the yield of the graphene devices, a technique for selective removal of a single layer of graphene or graphite should be introduced.

Reactive Ion Etch (RIE) is one way to etch materials with a dry gas. Thick graphene stacks or graphite can be etched out by the RIE with a PMMA mask. The RIE

process is conducted in a vacuum chamber as shown in Figure 9. Usually, a RF frequency electromagnetic field is applied between a substrate and an electrode to generate ions. Near the top electrodes, marked by green area in Figure 9, neutral molecules such as O_2 or CF_4 are ionized by oscillating electrical field. Electrons, which are generated in the RIE chamber and adsorb on inner wall of the chamber, are fed out to ground. However, electrons near substrates remain in the flatter under the substrate, generating a DC electric field. Due to the DC field, ionized molecules drift to the substrate and hit the surface of materials. Because graphene consists of a single layer of carbon atoms, it is easily removed by physical bombardment of oxygen ions.

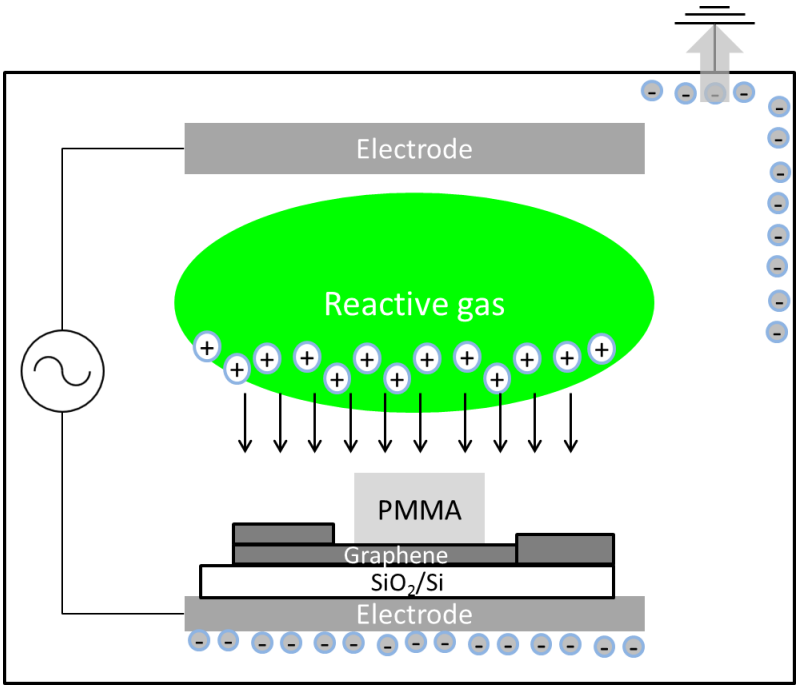

Figure 9 Schematic diagram of Reactive Ion Etch operation to etch graphene.

SEM images of the graphene device before and after the RIE etching process are shown in Figure 10. The graphene device was interfered with unintended flakes after fabrication of the device as shown in Figure 10 (a). The redundant graphite was etched out by RIE with the PMMA mask. As a consequence of RIE etching, only the selected area is etched, resulting in a graphene FET device as shown in Figure 10 (b).

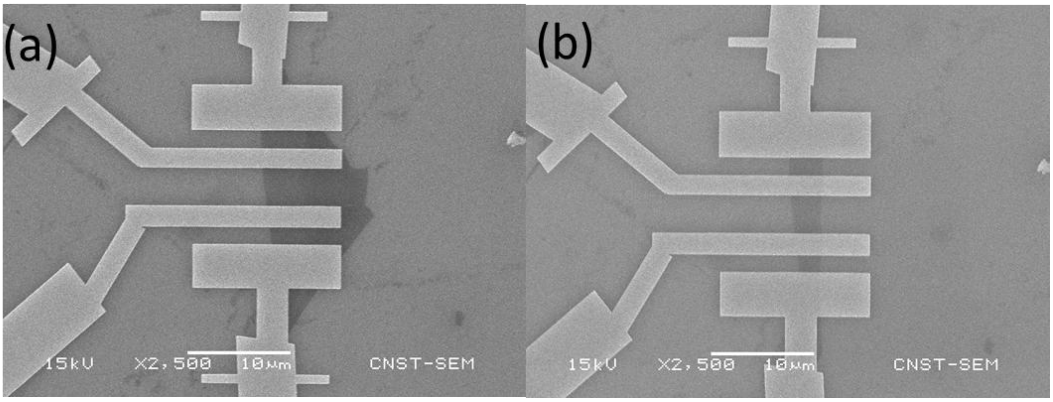

Figure 10 SEM images of graphene devices (a) before and (b) after RIE etching

A flow diagram to make the PMMA mask for a RIE etching process is illustrated in Figure 11. The graphene flake chosen for device fabrication interfered with other graphene or thin graphite is shown in Figure 11 (a). Prior to RIE etching, the graphene flake chosen for device fabrication should be masked by PMMA and graphene or graphite which interfere with device fabrication should be irradiated by electron beams to remove the PMMA, which can be completed by EBL (Figure 11 (b)). After

development, the only area which will be etched during the RIE process is exposed to air and removed by RIE. In the RIE process as shown in Figure 11 (c), both graphene and PMMA are etched out together but different etch rates. To avoid the entire removal of the graphene and PMMA, proper RIE power and time must be selected. In this project, the etching process was conducted with a power ranging from 20 to 50 watts for 40 seconds. The graphene device after removal of redundant graphite is shown in Figure 11 (d). Finally, residual PMMA can be cleaned off in acetone.

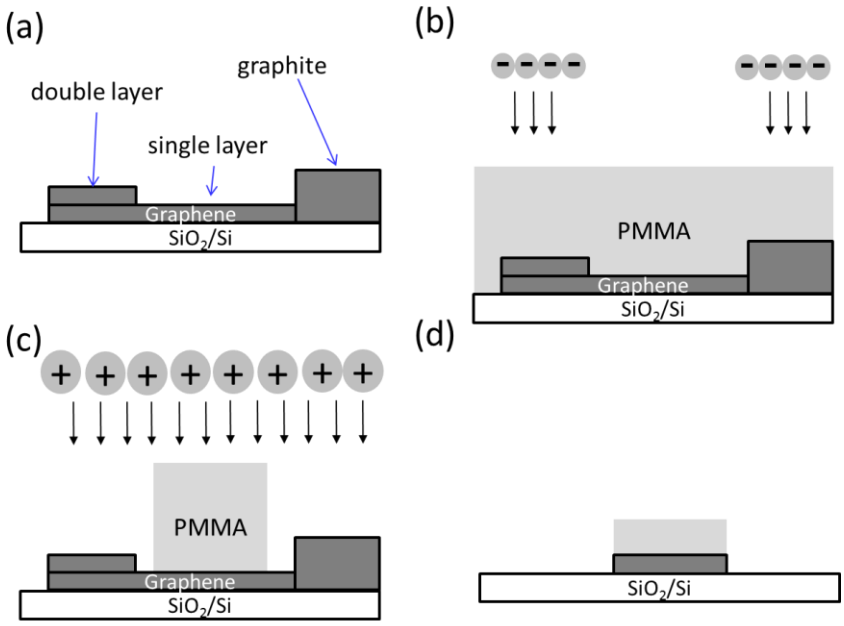

Figure 11 The schematic diagram of reactive ion etch process of graphene. (a) A graphene flake is interfered with other graphene or graphite. (b) Making a PMMA mask by EBL. After EBL process, the only actual graphene device area is covered with PMMA. (c) In RIE, ions are accelerated to substrates and etch both PMMA and graphene and graphite. (d) The only graphene underneath PMMA remains with covered with PMMA which can be removed by acetone.

3.1.5 Suspended Graphene

In order to investigate the influence of the oxide layer on a hysteresis and a n-type doping behavior as a result of electron beam irradiation, suspended graphene devices were fabricated. Suspension of the graphene devices was achieved from the supported graphene on SiO_2/Si by etching the oxide layer underneath the graphene as shown in Figure 12. The oxide layer was etched out in Buffered Oxide Etchant (BOE) which is a mixture of diluted HF (55%) and NH_4F (40%) in DI water. The graphene devices on SiO_2/Si were immerged in BOE for 10 minutes, and stayed in DI water for 5minutes. When the etchant was washed out by the DI water, the water was replaced with IPA keeping the device wet. In order to avoid the collapse of graphene during drying process due to surface tension of the liquid, a critical point dryer was employed. The suspended graphene device is shown in Figure 12 which clearly reveals that oxide layer under the graphene was fully removed, and the graphene is attached to the electrodes.

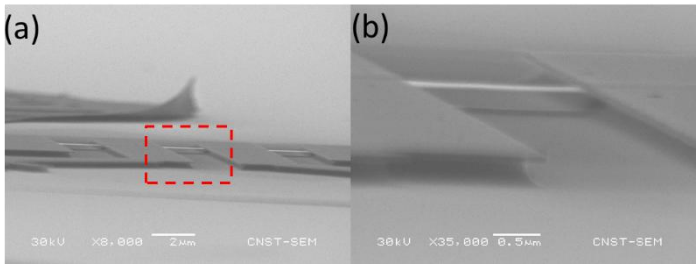

Figure 12 (a) Suspended graphene. (b) Magnified image of the suspended graphene zoomed into red dotted square in (a)

3.2 Fabrication and characterization tools

3.2.1 Electron Beam Lithography

The entire electron beam lithography procedure follows multiple steps introduced in block diagram in Figure 13. The first step of the lithography is to deposit PMMA, which is a commonly used electron resist material. This process is achieved by spinning substrates in the spin coater. The thickness of PMMA can be controlled by spin coating parameters such as spinning time and speed. PMMA concentration is also important to determine its thickness. In our experiments, 2% PMMA diluted in chlorobenzene was spun on substrates with a spinning speed of 4000rpm for 50 seconds, resulting in a PMMA film slightly higher than 100nm-thick. Soft baking is followed at 165°C for 1 minute to dry the solvent.

After soft baking, PMMA is exposed to an electron beam controlled by a Nanometer Pattern Generating System, which is the software to control the electron beams for specific irradiation dosage provided by the EBL manufacturer. During e-beam writing, energetic electrons irradiated on PMMA break long back-bone polymer chains into small pieces, but PMMA is still covered on the substrate. The fragmented pieces of PMMA as a consequence of the electron beam exposure are resolved in the developer, a mixture of MIBK/IPA, resulting in exposure of irradiated area into ambient air. After development, metallization is completed by metal deposition and lift-off.

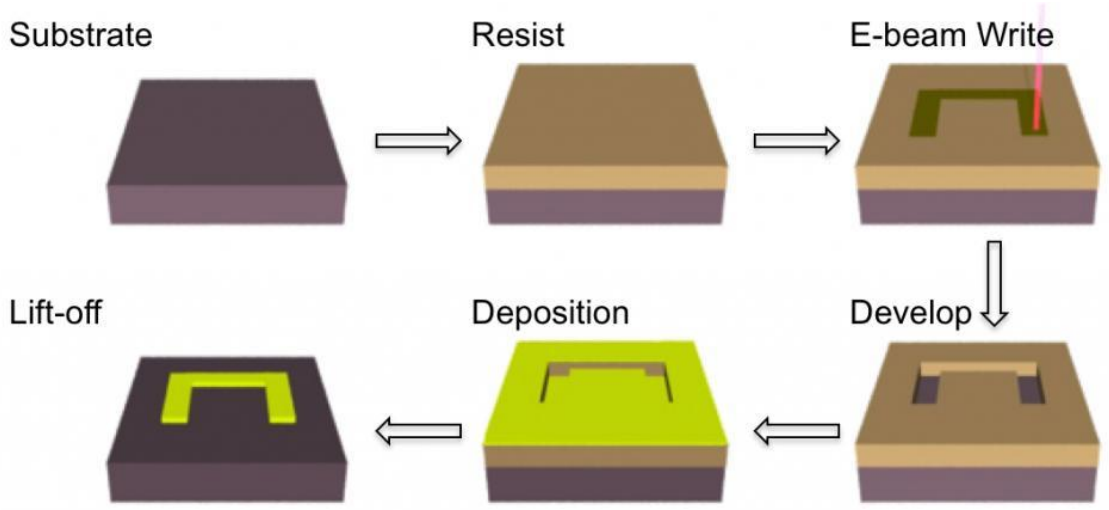

Figure 13 Schematic diagram of the electron beam lithography process

3.2.2 Raman spectroscopy

Raman spectroscopy is an important technique to study graphene. In particular, the technique provides a reliable method to distinguish a single layer of graphene from multiple layers of graphene or graphite [86, 88]. In addition, the Raman signals provide a method to investigate defects generated in graphene such as atomic vacancies or molecular adsorption [74, 77, 79, 81, 89].

When a light, which is an oscillating electric field, incidents into materials the electric field interacts with atoms in the materials. The electric field is expressed in terms of sinusoidal waves with its oscillating frequency by equation 3.4.

$$E = E_0 \sin \omega_i t, \tag{3.4}$$

where ω_i is the frequency of the incident light and E_0 is the amplitude of the electric field. As a consequence of the interaction between the incident light and atoms in the materials, the incident light experiences elastic or inelastic scatterings in materials. Due to the scattering of the light with phonons, the polarizability of the material is determined by the phonon frequency as shown in equation 3.5.

$$\alpha = \alpha_0 + \alpha_1 \sin \omega_q t, \tag{3.5}$$

where α_0 and α_1 are constants related to the characteristics of the material, and ω_q is phonon frequency of the solid. Combining equations 3.4 and 3.5, the polarization can be expressed in terms of ω_i and ω_q, which is shown in equation 3.6,

$$\begin{aligned} P = \alpha E = E_0[\alpha_0 \sin \omega_i t + \frac{1}{2}\alpha_1 \cos(\omega_i - \omega_q)t \\ - \frac{1}{2}\alpha_1 \cos(\omega_i + \omega_q)t. \end{aligned} \tag{3.6}$$

As a result of the interaction between the incident light with frequency of ω_i and a phonon with frequency of ω_q, the resulting lights have frequencies with ω_i and $\omega_i \pm \omega_q$ by creating (negative sign, the Stokes process) or destroying (positive sign, the anti-Stokes process) phonons as shown in equation 3.6. In the Raman scattering experiments, atomic or molecular vibrational modes of materials can be studied by detecting ω_q, which is called a Raman shift.

A typical Raman spectrum of the single layer of the graphene that has defects is shown in Figure 14 (a). The peak around 1320cm^{-1} marked 'D', which originates from 'Disorder', appears only when the symmetry of the $A1_g$ vibrational mode is broken as presented in Figure 14 (c) [90]. For example, the Raman 'D' band appears when defects such as inhomogeneous adsorption of molecules or atomic vacancies in graphene make the $A1_g$ mode vibration asymmetric in the honeycomb lattice. Unlike the disorder peak, the 'G' peak comes from the intrinsic E_{2g} vibrational mode, which is a lateral vibrational mode as depicted in Figure 14 (d). This vibrational mode is doubly degenerated along the x and y axis.

A single layer of graphene can be identified by analyzing the '2D' peak, which is also named 'G``. Unlike other Raman bands, this band occurs as a result of a 2nd order process named Double Resonance (DR) process as shown in Figure 14 (e). In this DR process, the excited electrons by incident light can be coupled with phonons. While these excited electrons scatter with phonons, they transit between K and K' valleys in a reciprocal space, which is called inter-valley scattering. The scattered electron comes back its original position in a reciprocal space to conserve energy. During the DR process, only one possible energy state is available in the K and K' valleys, indicating that only one possible Raman peak can be allowed. Therefore, the single 2D band of the Raman spectrum is a signature of the one atomic layer of carbons. In bilayer graphene, however, the valleys in the unit cell are doubled and the possible energy states can be increased up to four, indicating that the Raman 2D band is broadened by overlapping of

the four sub-peaks. With increasing layers of graphene, the number of energy states of electron during DR process increases, resulting in broadening of the 2D peak. In this sense, a single layer graphene can be distinguished from multilayers, and Raman spectroscopy provides a reliable and nondestructive method to identify the single layer graphene [86, 91].

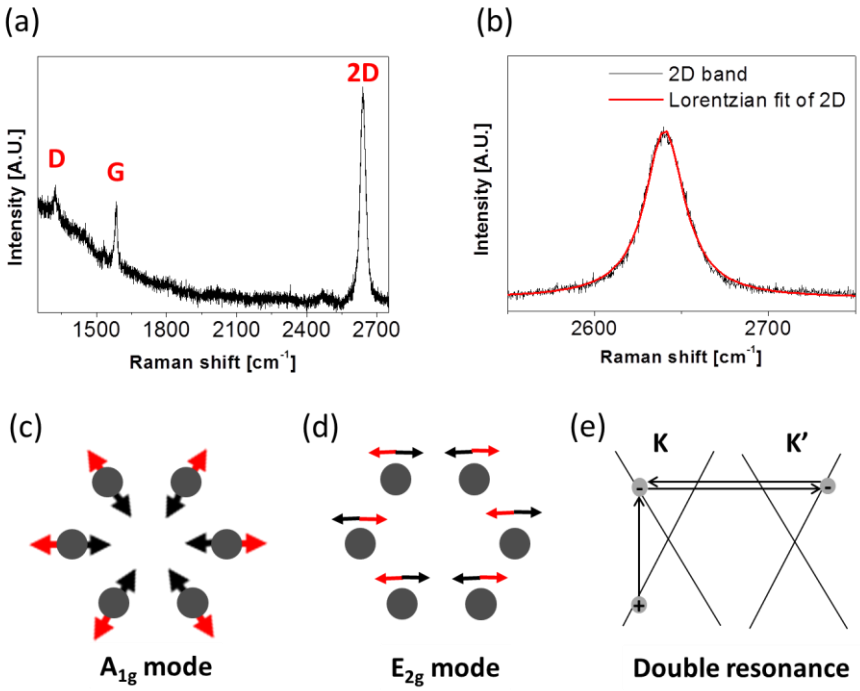

Figure 14 Raman spectrum of a single layer graphene. (a) Typical Raman spectrum of a graphene which includes defects. In the spectrum, each band is indicated D, G, and 2D (b) 2D band of the Raman spectrum and Lorentzian fitting with Full Width Half Maximum less than 30cm$_{-1}$, a signature of single layer of the graphene. Schematic diagram of the vibrational modes of (c) A_{1g} and (d) E_{2g} are shown, which corresponding to D and G bands in (a). Arrows indicate the direction of vibration at lattice points. (e) Schematic diagram of double resonance for the 2D band.

3.2.3 Atomic Force Microscopy

Atomic Force Microscope (AFM) is a scanning microscope to sense the force between the sharp tip and a surface of material. There are two operational modes, contact and non-contact. In contact mode, the tip scans the sample by touching the surface, and the tip is deflected according to the force between the tip and sample. The deflection of the cantilever is monitored by the laser and the proper position of the tip is adjusted by a feedback signal. In non-contact mode, the AFM cantilever oscillates with its free amplitude (A) and resonance frequency (ω_0). As the tip approaches the sample, the amplitude or the frequency is changed. The feedback signal adjusts the vertical position of the tip, recovering the amplitude or frequency of the tip. The feedback system records the vertical distance from the sample and provides a map of surface morphology. Not only topography but also a phase change of the oscillating cantilever reveals important information to figure out the surface of materials. To understand the phase shift of non-contact mode (tapping mode), it is important to know how the phase angles of cantilever oscillation are related to the force between the cantilever and sample. The motion of the oscillating cantilever derived by sinusoidal electrical signals in AFM is equivalent to the forced harmonic oscillator [92, 93]. The phase (ϕ) of the freely oscillating cantilever can be expressed as

$$\phi = \tan^{-1}\left(\frac{m\omega\omega_0}{Q(k - m\omega^2)}\right), \tag{3.7}$$

where m is mass, ω_0 is resonance frequency of the cantilever, ω is vibrating frequency of the cantilever when the tip interacts with a sample, and Q is the quality factor or Q value. The ϕ varies from $-\frac{\pi}{2}$ to $\frac{\pi}{2}$ depending on the argument in arctangent function in equation (3-7) and is $\frac{\pi}{2}$ for $\omega = \omega_0$. When the oscillating cantilever approaches the material surface, as a result of the interaction between the tip and the surface, the spring constant k is replaced with $k_{eff} = k + \sigma$. Here, k_{eff} is effective spring constant, and σ is the force derivatives with respect to the vertical distance as shown by

$$\sigma = \frac{dF}{dz}, \tag{3.8}$$

where F represents forces from the tip-sample interaction, and z is the vertical distance between the tip and the sample surface [92]. The ϕ changes to ϕ_0 due to tip-sample interaction, and ϕ_0 simplified to equation 3.9 under the condition, $\sigma << k$,

$$\phi_0 = \tan^{-1}\left(\frac{m\omega\omega_0}{Q(k + \sigma - m\omega^2)}\right) \rightarrow \tan^{-1}\left(\frac{k}{Q\sigma}\right). \tag{3.9}$$

The phase shift ($\Delta\phi$) measured from the AFM is the phase difference between the phase in free oscillation ϕ ($\omega = \omega$) = $\pi/2$ and ϕ_0, which can be simplified for small σ such as

$$\Delta\phi = \frac{\pi}{2} - \tan^{-1}\left(\frac{k}{Q\sigma}\right) \sim \frac{Q\sigma}{k}. \tag{3.10}$$

The phase shift is a function of σ, which is the result of the tip-sample interaction. According to equations 3.9 and 3.10, a positive (repulsive force) and a negative (attractive force) σ values induce a positive and a negative phase shift, respectively. In tapping mode, Δϕ is determined by σ, which is approximated to the stiffness (S) of surface by equation 3.11,

$$\Delta\phi \approx \frac{Q}{k} < S >, \tag{3.11}$$

where <S> indicates the time-averaged value of the stiffness of the sample surface [92, 94]. Equation 3.11 reveals that Δϕ is determined by the stiffness of the sample, indicating that the phase shift data from AFM is corresponding to the stiffness of the surface. The phase shift does not depend on the sample morphology but depends on the materials properties such as chemical composition or physical hardness. Because the morphology and phase signals are originated from different characteristics of materials, they are complementing each other to understand the surface properties of a certain material.

The AFM images of the morphology and the phase shift from graphene surface are shown in Figure 15. In particular, the surface morphology and the phase shift images of graphene zoomed into the red dotted square area are shown from (b) to (e). In a certain circumstance, the morphology images as shown in Figure 15 (b) and (d) alone do not provide useful information because the height contrast on the materials is negligible. With the help of the phase data shown in Figure 15 (c) and (e), however, the existence of

adsorbates on the graphene becomes clear because adsorbates are chemically different from graphene. Furthermore, the phase images allow us to observe the development of the surface state due to electron irradiation. In investigating nanometer scale structure or different chemical composite, for example biological materials or organic-inorganic interfaces, the phase images provide clear insight into the surface of materials. In particular, the phase shift mappings from biological or chemical surfaces reveal clear images even though the morphology images are blurry [92, 95].

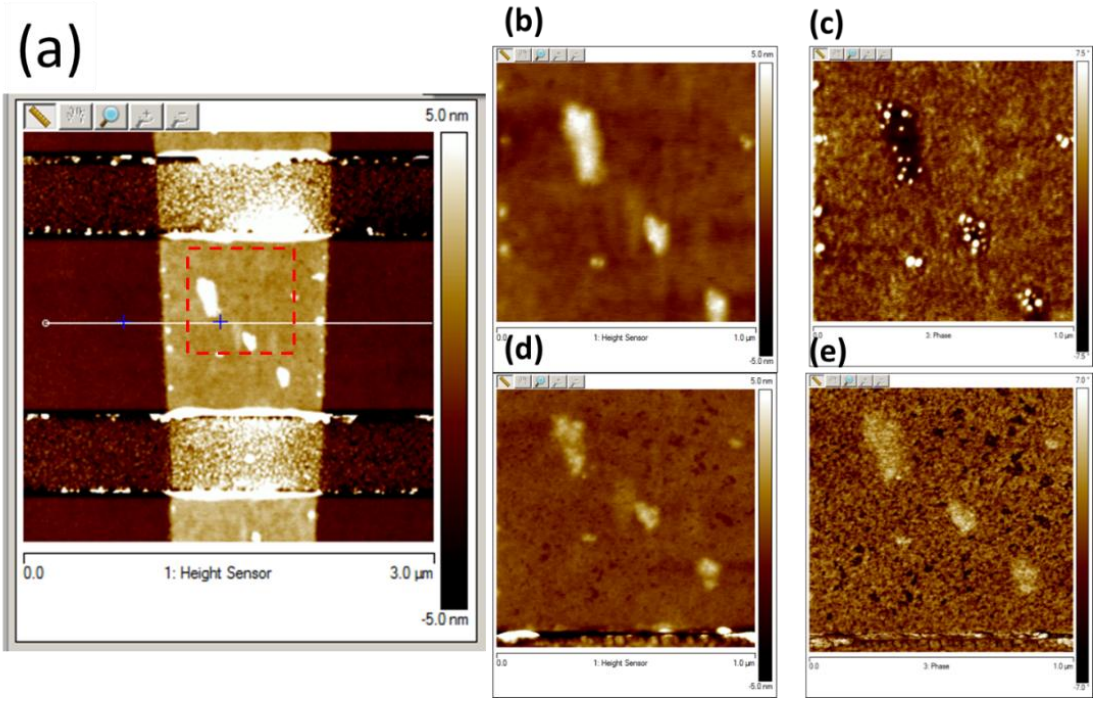

Figure 15 AFM images of graphene FET device. (a) Morphology of graphene FET device. (b) Morphology and (c) Phase shift of pristine graphene zoomed into red dotted square area. (d) Morphology and (e) Phase shift after electron irradiation of 2mC/cm^2.

3.2.4 Electrical transport properties

The transport properties measurement system was designed to conduct measurement while the graphene device was stayed in the EBL chamber (JSM-6460) to investigate the effect of electron irradiation on graphene as shown in Figure 16. An electrical heater (Ultramic 600 heater) was installed to clean pristine graphene and study the annealing effects of graphene FET devices after electron irradiation. The transport properties of graphene FET devices were measured at room temperature in a high vacuum environment. While the transport measurements were conducted, gate voltage was applied between the I- electrode and the silicon substrate. Both resistance and gate voltage signals were received by two voltmeters (HP 3478A and KE 199), which were connected to a computer by General Purpose Interface Bus (GPIB) cable. Both signals from voltmeters were handled by the Labview and saved in a computer simultaneously.

During transport measurement, a small signal, ~100nA of Vp to Vp sinusoidal wave, is generally recommended as the excitation current in order not to induce local heating, which alters carrier transport behavior in graphene. In this small scale of electronic signal, the amplification of the small signal and filtration of background noise is required. To satisfy those requirements, a lock-in amplifier (PAR, 124A) is employed for transport measurements. A block diagram of transport measurement by a lock-in amplifier is shown in Figure 17. The AC excitation current is generated by the lock-in amplifier and induced to graphene through electrodes I+ and I- in Figure 16. At the same

time, potential difference (V_{in} = V+ - V-) goes to a lock-in amplifier passing through a pre-amplifier.

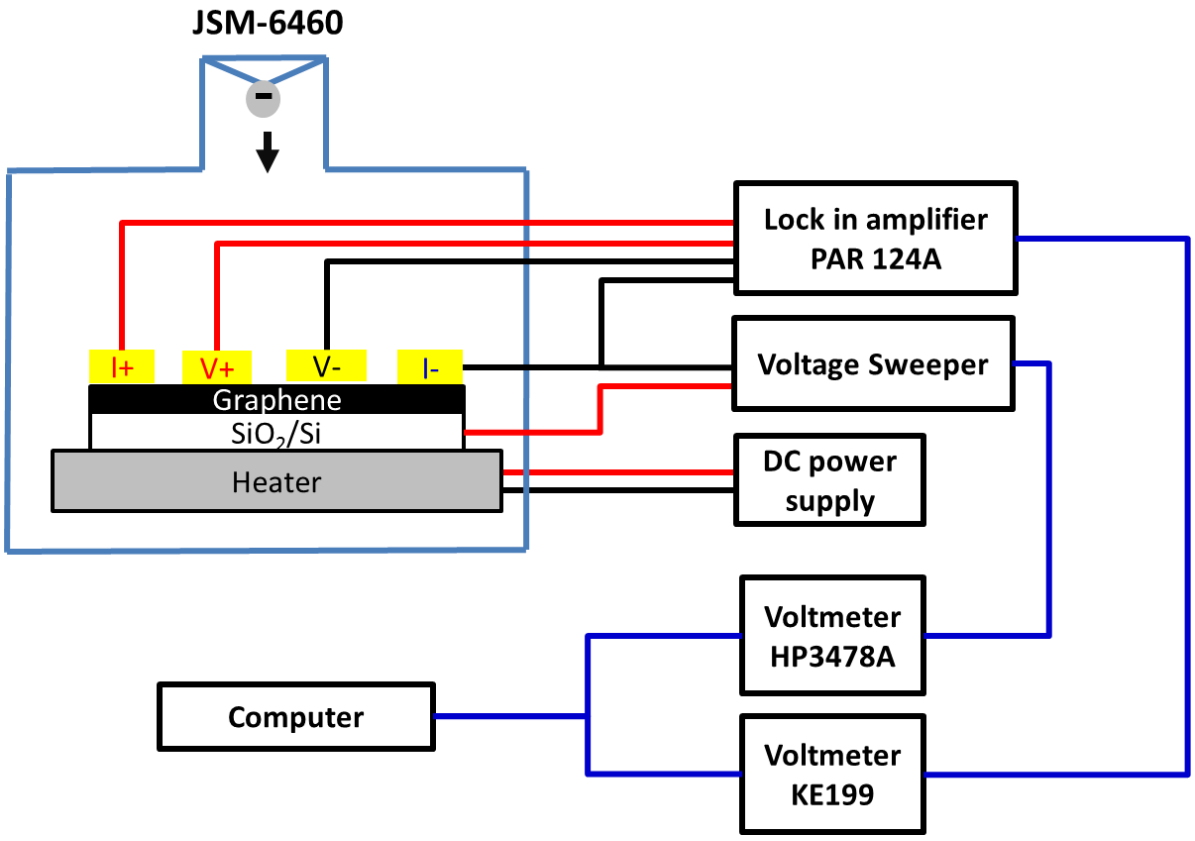

Figure 16 Blcok diagram of in-situ transport measurement system in a vacuum after electron beam irradiation. Graphene device stays on an electrical heater. Electrical wires are connected through a vacuum feedthrough.

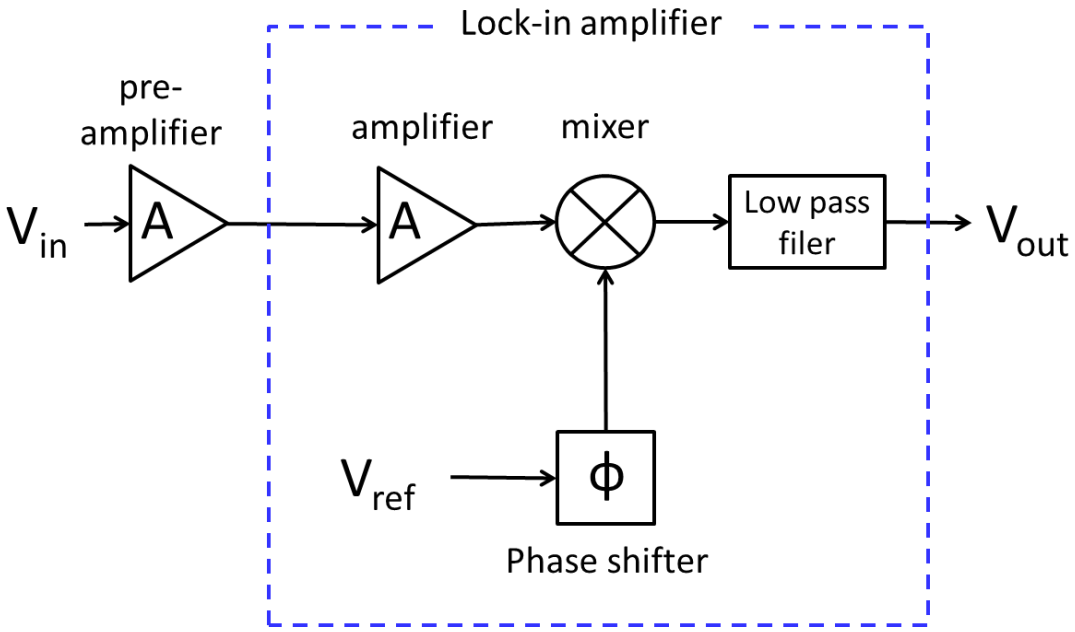

Figure 17 Block diagram of a lock-in amplifier. Blue dotted box represents lock-in amplifier. Pre-amplifier is attached to input channel to amplify signal and reduce noise.

V_{ref} and V_{in} are sinusoidal waves represented by equation 3.12 and 3.13.

$$V_{ref} = \sqrt{2}V_R \cos(\omega_R t + \emptyset_R) \tag{3.12}$$

$$V_{in} = \sqrt{2}V_I \cos(\omega_I t + \emptyset_I) + n(t) \tag{3.13}$$

Here, subscripts I and R represent 'in' and 'ref', and V, $\omega, \emptyset$ indicate amplitudes, angular frequency, and the phase of signals, respectively. n(t) represents random noises due to noise and electrical interference. After V_{in} passes through the mixer in the lock-in amplifier, the intermittent signal is represented by a multiple of V_{in} and V_{ref} shown by

$$
\begin{aligned}
&V_{ref} \times V_{in} \\
&= V_R \cos(\omega_R t + \emptyset_R) \times V_I \cos(\omega_I t + \emptyset_I) + V_{ref} \times n(t) \\
&= V_R V_I \cos[(\omega_R + \omega_I)t + \emptyset_I + \emptyset_{ref}] + V_R V_I \cos[(\omega_R - \omega_I)t + \\
&\emptyset_I - \emptyset_{ref}]
\end{aligned} \tag{3.14}
$$

The product $V_{ref} \times n(t)$ is always zero in the final output because the average value of a sinusoidal function is zero. A low pass filter cuts off at a frequency less than ω_R, which indicates that the high frequency component should be disappeared in the out signal. When the $\Delta\omega = \omega_R - \omega_I$ is zero, the resulting V_{out} has only the DC component, which is proportional to the amplitude of input voltage (V_I) and depends on phase difference between input and reference signals ($\emptyset$) as shown in equation 3.15,

$$V_{out} = V_R V_I \cos(\emptyset_I - \emptyset_{ref}) \propto V_I \cos(\emptyset). \tag{3.15}$$

Another important feature that the AC measurement technique allows us is to test the contact state between graphene and electrodes. Because the lock-in amplifier uses the AC current through graphene devices, it provides the phase shift with respect to the reference signal. Therefore, a measurement between a pair of electrodes, which is shown in Figure 18 (a), reveals the phase shift, a measure of contact between graphene and electrodes. The value of the phase shift changes to -90° with increasing the capacitive component in the electrical circuit, which mainly originates from the insulating layer between graphene and electrodes. In this project, the phase shift within 3° is tolerated. Therefore, only the devices showing good contact are allowed to do electrical transport

measurement. In order to improve electrical contacts, wide electrodes are beneficial. Although the width of electrodes depends on each device, width of electrodes of V+ and V- is increased and reached up to 1um for certain devices. The length of the graphene to convert from a resistance to a resistivity is measured between centers of the potential probes as shown in Figure 18 (b).

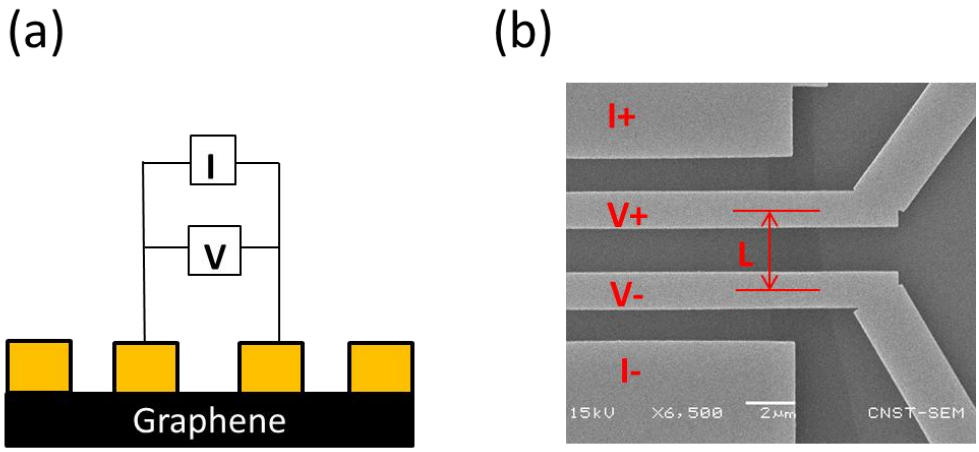

Figure 18 (a) Schematic diagram of contact states verification. (b) Definition of the channel length of graphene.

In actual transport measurements, a graphene FET device was wired to a lock-in amplifier, which makes it possible to extract small signals in the presence of noise. In order to prevent local heating of graphene by the excitation current during the transport measurement, 100nA was induced through graphene. The four-probe measurement

technique was introduced to remove the contact resistance between electrodes and graphene as shown in Figure 19 (a). The AC current was induced between the I+ and the I- electrodes, and the voltage between two potential probes was measured and converted to resistance by ohm's law. A Resistance was measured during carrier concentration, which was modulated by the gate voltage as shown in Figure 19 (b).

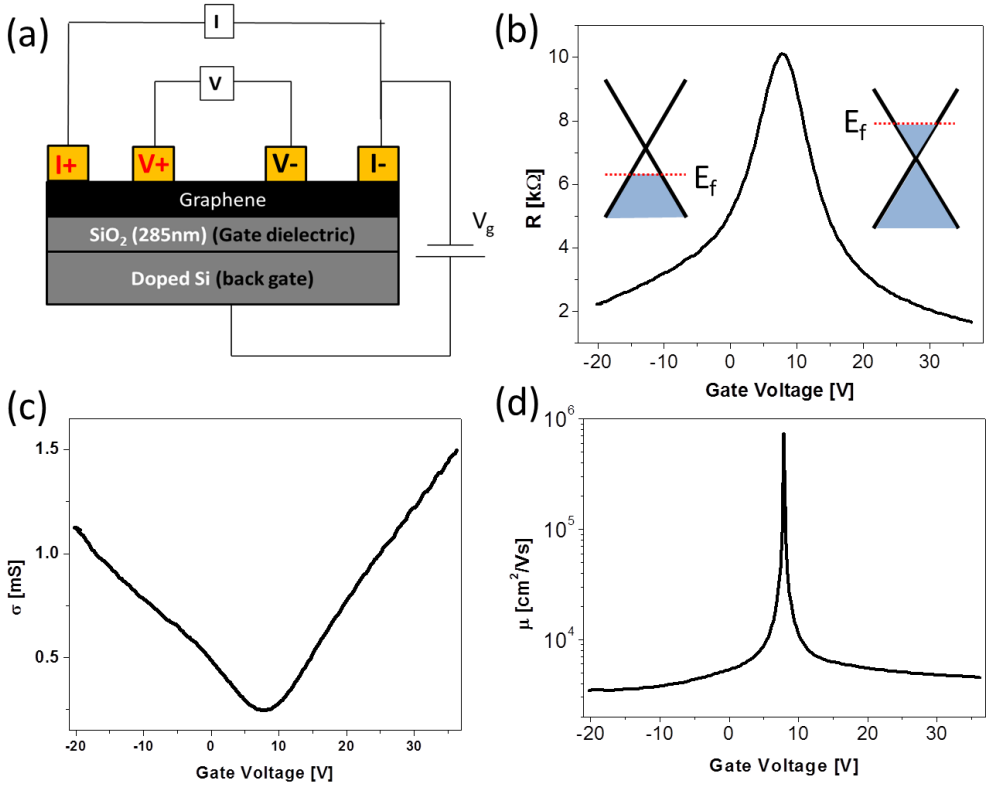

Figure 19 (a) Schematic diagram of 4-probe measurement with gate voltage application of the graphene device. (b) Resistance, (c) conductivity, and (d) mobility data of the graphene is displayed. The insets in (b) indicate Fermi levels corresponding to electrons and holes according to the gate voltage.

The carrier density, n, was modulated by applying a gate voltage and expressed in terms of the gate voltage and the capacitance of the dielectric layer as shown in equation (3.16).

$$ne = C_{ox}V_g \tag{3.16}$$

Here, e is the electron charge, C_{ox} is the capacitance of the oxide layer, and V_g is the gate voltage. In contrast to common semiconductors, both holes and electrons can be tuned to be a majority carrier by manipulation of the gate voltage, indicating that the Fermi energy, E_f, can be controlled by the applied gate voltage. When the positive gate voltage was applied, electrons were accumulated on graphene, locating the E_f above the origin as shown in the inset of the Figure 19 (b). Meanwhile, holes served as a majority carrier for the negative gate voltage, lowering the E_f below the origin.

Although the averaged charge concentration is zero at V_D, the conductivity reveals the universal nonzero minimum value, which stems from formation of hole and electron puddles. All the graphene devices fabricated in the cleanroom reveals p-type doping behaviors as shown Figure 19 (b), which is in accordance with a previous report that graphene supported by SiO_2/Si substrates reveals the p-doping behavior before annealing and converts to the n-type as a result of annealing [96].

Making use of the channel length (L) and the width (W), which are defined in Figure 4, a conductivity and a mobility can be derived from the measured resistance as shown in equations 3.17 and 3.18.

$$\frac{1}{\sigma} = \rho = R\frac{W}{L} \tag{3.17}$$

$$\mu = \frac{1}{ne\rho} = \frac{1}{\rho C_{ox}(V_D - V_g)} \tag{3.18}$$

Here, σ is the conductivity, ρ is the resistivity, n is the carrier concentration, e is the electron charge, C_{ox} is the capacitance of the oxide layer between the Si and the graphene, V_D is the Dirac point, V_g is the gate voltage applied, and μ is the carrier mobility. The conductivity and the mobility derived from the measured resistance are plotted in Figure 19 (c) and (d).

3.2.5 Annealing effect of graphene

Graphene devices fabricated by the mechanical exfoliation technique have chances to be contaminated by a sticky material from the scotch tape and chemical residue from PMMA during the device fabrication process. These kinds of contaminants change the intrinsic properties of graphene devices. In particular, transport properties of the graphene devices can be deteriorated by an increase of resistance. Moreover, the asymmetric feature of the transport properties between holes and electrons dominated conduction regions are related to the contamination of graphene as shown in Figure 20. In order to clean graphene devices in a vacuum, an electrical heater was installed to anneal the graphene devices in the EBL chamber. To prevent damage of the EBL system, heating the device was limited to 200°C for 10 minutes. We observed that transport properties of graphene devices were improved by the short term annealing at

200°C in a vacuum as shown in Figure 20. The low quality graphene devices reveal the asymmetric transport behavior between holes and electrons dominated conduction regions such as a high magnitude of resistivity, and a P-type doping behavior [18] as plotted by the black curve in Figure 20 (a). As the graphene device was cleaned by annealing at 200° for 5 minutes, the V_D moved toward the negative gate voltage, and the magnitude of resistivity was reduced. Although the asymmetric nature of resistivity slightly remained after annealing, it revealed the enhanced transport behaviors, indicating that annealing of the graphene device at 200°C is effective to clean it in our project.

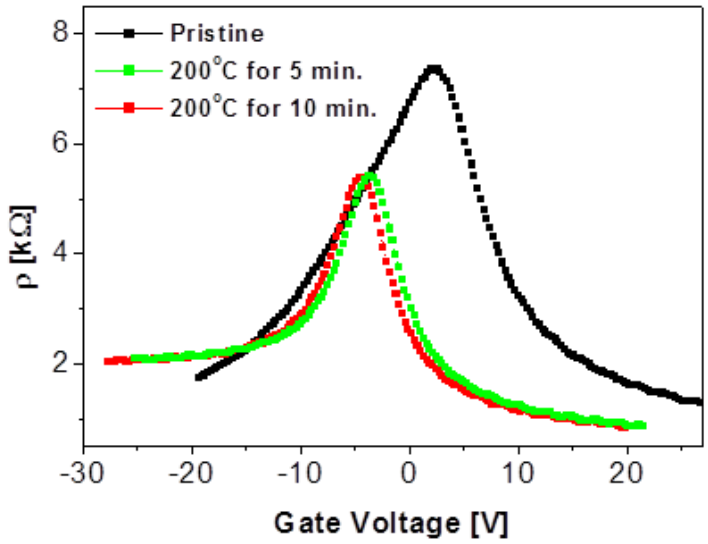

Figure 20 Annealing effects of graphene FET devices on transport properties. Annealing was conducted at 200°C in vacuum of $2*10^{-5}$ Torr.

In order to investigate annealing effect further, surface morphology was measured by AFM and compared before and after annealing graphene as shown in Figure 21.

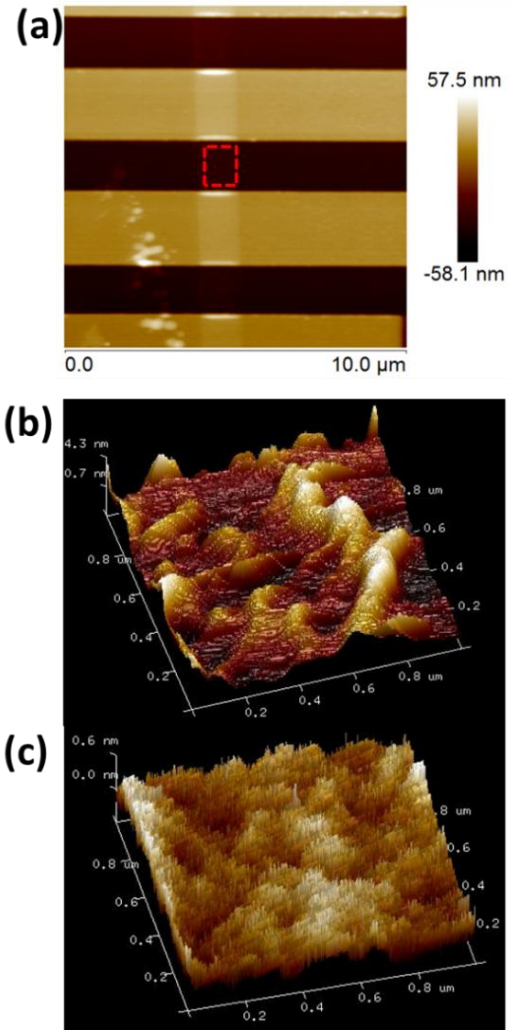

Figure 21 AFM images of graphene before and after annealing (a) 10um scale image. (b) 3D surface morphology of pristine and (c) annealed graphene. (b) and (c) are scanned from graphene indicated by red dotted square in (a)

Not all graphene devices reveal remarkable dirty materials but residue remains on the graphene surface even after cleaning with IPA and acetone. The height of the dirty materials reaches 4nm as shown in Figure 21 (b), which is thicker than the thickness of graphene measured by AFM. Although ideal thickness of graphene is 0.35nm, the height of the graphene reported from AFM experiments ranges from 1.6 to 2nm. After cleaning the graphene by annealing at 200°C for 10 minutes, most of the residue was removed and the surface of the graphene was cleaned and flattened with the maximum height of the residue is less than 0.6nm as shown in Figure 21 (c). Transport properties in Figure 20 show improvement as the surface of the graphene devices is cleaned by annealing, which is a consistent result with AFM images in Figure 21. The AFM data further supports the idea that short term annealing in our measurement system is enough to clean the device.

CHAPTER IV

THE EFFECT OF ELECTRON BEAM IRRADIATION ON A PMMA/GRAPHENE DOUBLE LAYER*

4.1 Motivation

Because graphene is a single layer of atomic carbon and affected by defects or surface adsorbates, the effects of bombardment by energetic particles such as ions [63, 64], photons [61], and electrons [76, 79, 81] should be studied. As a result of energetic ions or electrons irradiation on graphene, graphene can be damaged, causing degradation of electrical transport properties. There are many chances for the graphene to be exposed to electron beams during device fabrication and characterization, therefore it is important to elucidate the effect of the e-beam irradiation on graphene and that effect has not been studied yet. Because EBLs are widely used for device fabrication and PMMA is a common electron-resist used during e-beam lithography, the local alteration of the PMMA/graphene bilayer, a stack of PMMA on top of graphene, as a result of exposure to energetic electrons is of particular interest. Even though the influence of electron irradiation on bare graphene has been studied, the impact of electron irradiation on PMMA/graphene bilayers and related changes of the electrical transport properties of graphene FETs have not yet been established. In this chapter, we present modified

* Part of this chapter is reprinted with permission from "The effect of electron induced hydrogenation of graphene on its electrical transport properties" Sung Oh Woo and Winfried Teizer, Appl. Phys. Lett. **103**, 041603 (2013): Copyright © 2013 American Institute of Physics.

electrical transport properties of the GFET devices due to electron irradiation on PMMA/graphene bilayer systems.

4.2 Experimental procedure

A schematic diagram of experimental procedure is shown in Figure 22. We prepared the graphene FET devices by mechanical exfoliation as introduced in chapter III, and Figure 22 (a) shows the pristine graphene. PMMA was spun on the graphene device as shown in (b) and baked on a hot plate at 165°C for 3minutes. Then, the PMMA/graphene bilayer was irradiated by electron beams with 30keV and 10pA. The Nanometer Pattern Generation System (NPGS) in EBL controlled the electron beam precisely, as shown in Figure 22 (c). The entire PMMA/graphene flake was exposed to electron beams, and the irradiated area was confirmed after development of PMMA by optical microscope. Finally, the PMMA was cleaned off by immersing the flake in acetone, and then the transport properties were measured in a high vacuum. The schematic diagram of transport measurement after removal of PMMA is revealed in Figure 22 (d). In order to investigate the effect of the electron beam irradiation on PMMA/graphene on transport properties of graphene after removal of the PMMA, processes from (b) to (d) were repeated with electron irradiation doses such as 0.4, 2, and 7mC/cm^2.

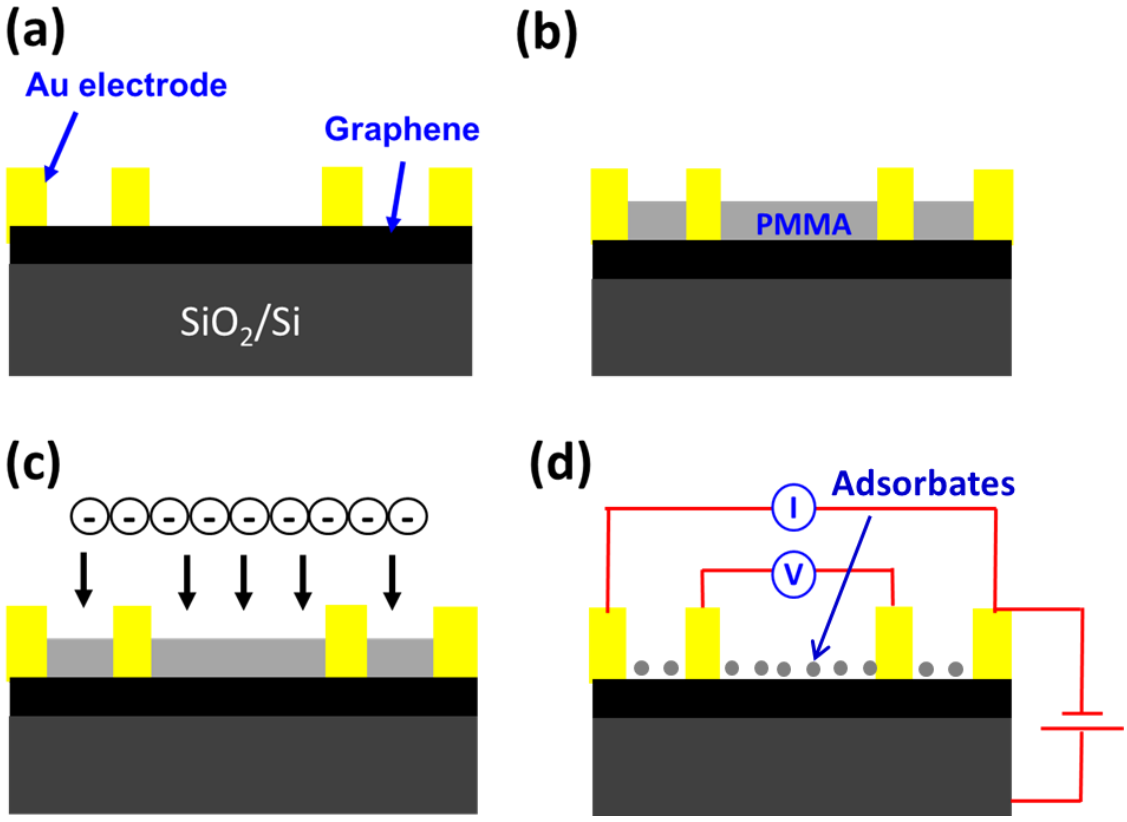

Figure 22 Schematic diagram of experimental procedure. (a) a pristine graphene FET device, (b) PMMA/graphene bilayer on a substrate, (c) electron irradiation on the PMMA/graphene, and (d) transport measurement in a vacuum after electron irradiation on PMMA/graphene and subsequent removal of PMMA.

4.3 Results and discussion

Characteristic properties of pristine graphene are shown in Figure 23. An optical microscope image of the graphene FET device is shown in Figure 23 (a). The length of the graphene flake reaches about 30μm, and the area irradiated after PMMA coating is marked by the green dotted square. The Raman spectrum in Figure 23 (b) reveals that

the graphene device does not have a Raman 'D' band, indicating that the pristine graphene does not have defect signatures from structural disorder or molecular adsorption. The Lorentzian fitting of the Raman '2D' peak in the inset identifies the flake as a single layer graphene because the 2D band shows a single peak nature with Full Width Half Maximum (FWHM) less than $30cm^{-1}$ [86, 91]. The mobility of the pristine graphene reaches up to $10^4 cm^2/Vs$ with a carrier concentration above $10^{12} cm^{-2}$ at room temperature, indicating that the graphene is a high quality single layer graphene. Resistivity data of the pristine graphene device measured in various conditions are shown in Figure 23 (d).

In ambient air, the graphene device revealed that the V_D was located at higher gate voltage than 20V, indicating the P-type doping of the graphene, which was in accordance with the graphene devices fabricated on SiO_2/Si substrates [89, 97, 98]. In addition, the values of V_D were different when the gate voltage swept up and down. The hysteresis of the gate voltage in ambient condition stems from environment molecules adsorbed on the graphene device. As the graphene device had stayed in a high vacuum for six hours, weakly bound adsorbates were removed, and the hysteresis disappeared. However, the mobility of the graphene was not remarkably improved even after removal of the air adsorbates on graphene as shown in Figure 23 (c).

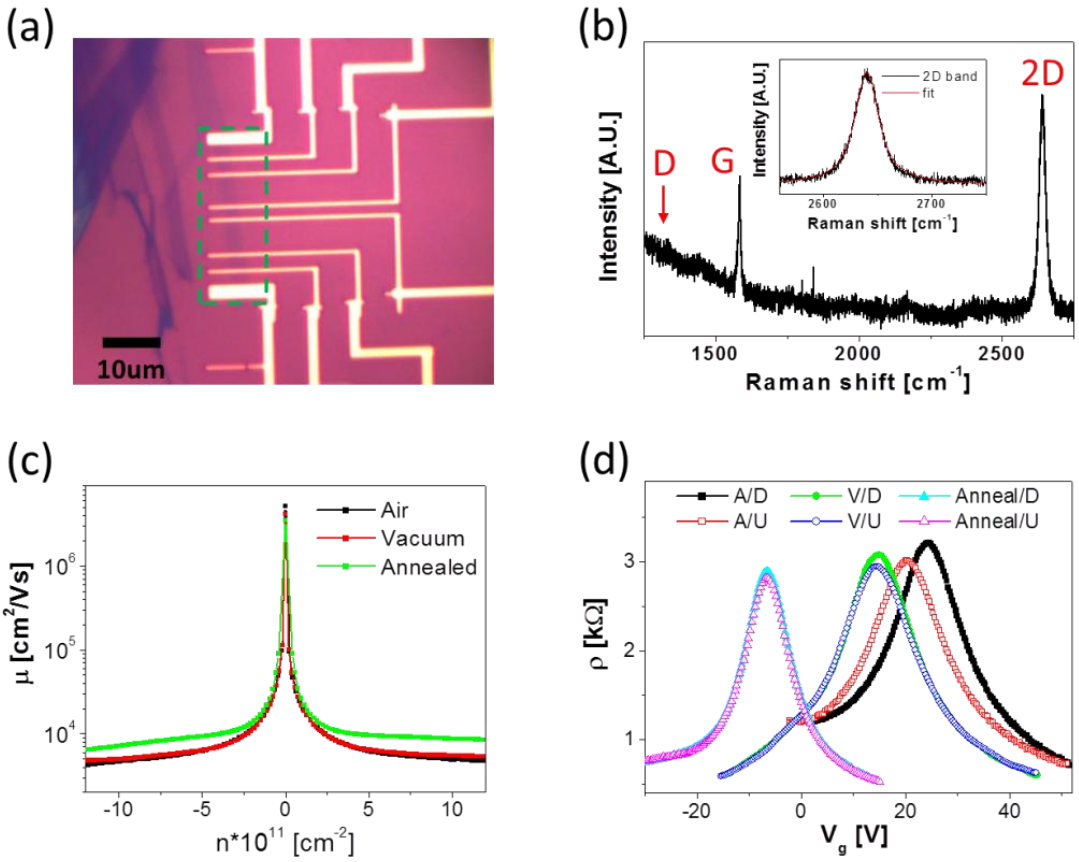

Figure 23 Properties of pristine graphene. (a) Optical microscope image of the pristine graphene device. Green dotted square is irradiated area by electron beams. (b) Raman spectrum of the pristine graphene. Magnified 2D band and its Lorentzian fit with FWHM of ~26.13 cm^{-1} are inserted as inset. (c) Mobility and (d) resistivity of the pristine graphene in ambient condition, vacuum, and annealed. Abbreviations 'A', 'U', and 'D' indicate 'Ambient', 'Up', and 'Down', respectively.

Once the graphene was annealed around 200°C for 5 minutes in a vacuum, the initial P-type doping behavior was inverted to the N-type, which was the result of removal of environment molecules adsorbed on graphene and in agreement with

previous work [97]. Even after removal of the environmental molecules at high temperature, the V_D was not at the gate voltage of zero, an indication of the existence of another contribution to the biased doping. As the device was exposed to ambient air, the transport curve recovered its initial properties. Therefore, in addition to other possible factors, the initial P-type doping behavior was dominated by environmental molecules adsorbed on top of the graphene. Moreover, the hysteresis appearing in ambient condition originated also from environmental molecules adsorbed on top of the graphene, because it disappeared when they were removed by the vacuum or annealing effects. In carbon nanotubes, the hysteresis is explained by polar molecules such as H_2O surrounding the carbon nanotube [99]. In graphene, the hysteresis is attributed to charge traps located between graphene and the gate oxide [89, 100] or charge transfer between graphene and adsorbates [100-102]. In this respect, we conclude that environmental molecules adsorbed on the graphene surface contribute to both initial P-type doping behavior and hysteresis appearance.

Electrical transport properties of the PMMA/graphene bilayer without electron irradiation are investigated in order to study the effect of PMMA on graphene. The resistivity of the PMMA/graphene bilayer before soft baking in Figure 24 (a) reveals a discrepancy of the CNP while sweeping up and down the gate voltage.

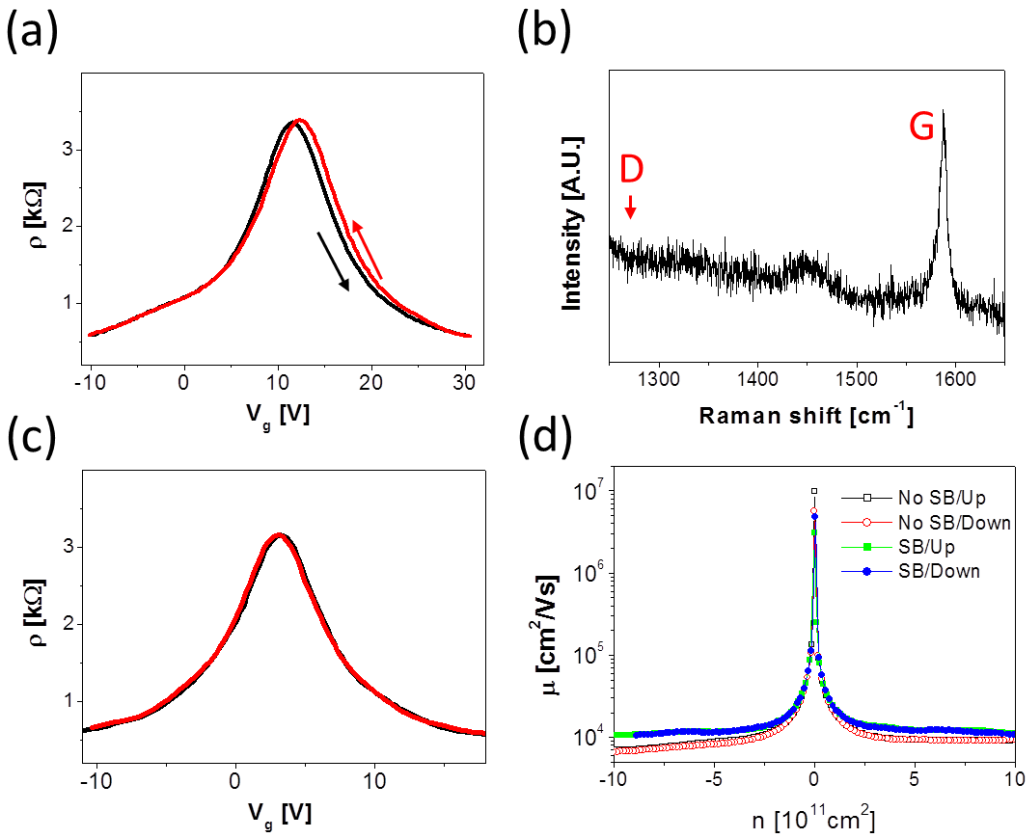

Figure 24 Electrical transport properties of PMMA/graphene bilayer without electron irradiation. (a) Resistivity shows hysteresis only in the device prior to soft baking. (b) Raman spectrum of the PMMA/graphene bilayer. (c) Resistivity of the PMMA/graphene bilayer after soft baking at 165°C for 3 minutes. (d) Mobility of the PMMA/graphene device before and after soft baking. The abbreviation "SB" means soft baked, and "Up" and "Down" indicate the direction of the gate voltage sweep, increase and decrease, respectively.

However, transport properties reveal improvement due to PMMA layer on the graphene when the PMMA bilayer is compared with the bare graphene device in Figure 23. In addition, the Raman spectrum of the PMMA/graphene bilayer does not reveal the

'D' band, a signature that PMMA layer on top of the graphene does not impede carrier transport as a result of interaction between graphene and PMMA solution. When the graphene device with the PMMA is baked at 165°C for 3 minutes, not only the CNP of the device is shifted toward negative value as shown in Figure 24 (c), which is the same behavior as the graphene device is cleaned by annealing, but also the magnitude of the mobility is enhanced. Because the hysteresis disappeared and the CNP shifted to a lower gate voltage value during soft baking, we suggest that the enhanced mobility is the result of evaporation of the environmental molecules from the graphene surface. Furthermore, we observed that PMMA serves as a protection layer of graphene from environmental molecules during the transport measurement, which is a remarkable characteristic of PMMA because it allows the graphene devices to operate in ambient conditions without losing its novel electronic properties.

After electron irradiation on the PMMA/graphene double layer and subsequent removal of PMMA, we observed that the Raman 'D' peak appears, and the relative intensity of D versus G, I_D/I_G, depends on the prior electron dose as shown in Figure 25 (a) and (b). In order to investigate the effect of the electron irradiation on PMMA/graphene on the transport properties, we extracted mobility data depending to the electron dosages. Equation (3-7) was used to derive the carrier mobility, and the induced charge concentration is calculated by equation (3-6). The value of the capacitance of the gate oxide is about 11.6nF/cm^2 [103]. We observed that irradiation with electron dosages comparable to the amount used in typical EBL (400uC/cm^2) does

not affect the transport properties of the graphene devices significantly as shown in Figure 25 (c). However, as the electron dosage increases, the mobility declines through the entire range of carrier concentration. Upon annealing the device, the mobility was recovered significantly, which is in agreement with corresponding Raman data that I_D/I_G decreases during annealing in Figure 25 (b). The transport behavior was similar to gas adsorption experiments in that transport properties changed as a result of gas adsorption and recovered as the adsorbates was removed [22]. In order to investigate the charge doping behavior, electron irradiation control experiments were conducted on bare graphene FET devices. As the electron beam irradiated in a single layer of graphene, the V_D shifted towards negative values, and the amount of the shift depended on electron dosage as shown in Figure 25 (d), which is the same behavior of the graphene devices from reported experimental results [79, 81] and is a signature of charge doping depending on electron dosage. Unlike irradiation on bare graphene, the shift of the V_D due to electron irradiation on the PMMA/graphene bilayer did not depend on the electron dosage, and the CNP remained around the origin even after successive irradiations. In other words, even though the amount of molecular adsorption increased based on Raman data as shown Figure 25 (a) and (b), the amount of charge doping did not change, which is an indication of neutral adsorbates.

The Raman 'D' band appears due to the asymmetry of the $A1_g$ mode in graphene [90]. This asymmetry is caused by structural disorder or atomic/molecular adsorption on graphene. Displacement of carbon atoms due to electron irradiation is not a plausible

scenario because electron beams with energy of 30keV are irradiated on the PMMA/graphene bilayer. This energy is far less than the established threshold energy (>86keV) to eject carbon atoms from their lattice points [66, 68]. Furthermore, the majority of electrons might lose their energy by scattering in the PMMA layer before arriving on the graphene.

A more plausible scenario of the Raman 'D' band appearance is due to adsorbates on graphene as a result of electron irradiation on PMMA/graphene. Various radicals such as H_2^+, CO^+, and CO_2^+ are generated by electron irradiation on PMMA [104]. In particular, graphene is hydrogenated due to electron irradiation on a Hydrogen Silsesquioxane (HSQ)/graphene bilayer [105]. In the electron irradiation on HSQ/graphene experiment, energetic electrons broke Si-H bonds in HSQ, and the hydrogen generated during the irradiation was then bound to graphene. Another experiment proposed that graphene could be hydrogenated due to fragmentation of H_2O adsorbates on graphene by exposing it to an electron beam [106]. Therefore, we argue that the Raman 'D' band, which appears after electron irradiation on the PMMA/graphene bilayer and subsequent removal of PMMA, is ascribed to the adsorption of fragmented hydrogen molecules or radicals from PMMA during the back bone secession process on top of graphene.

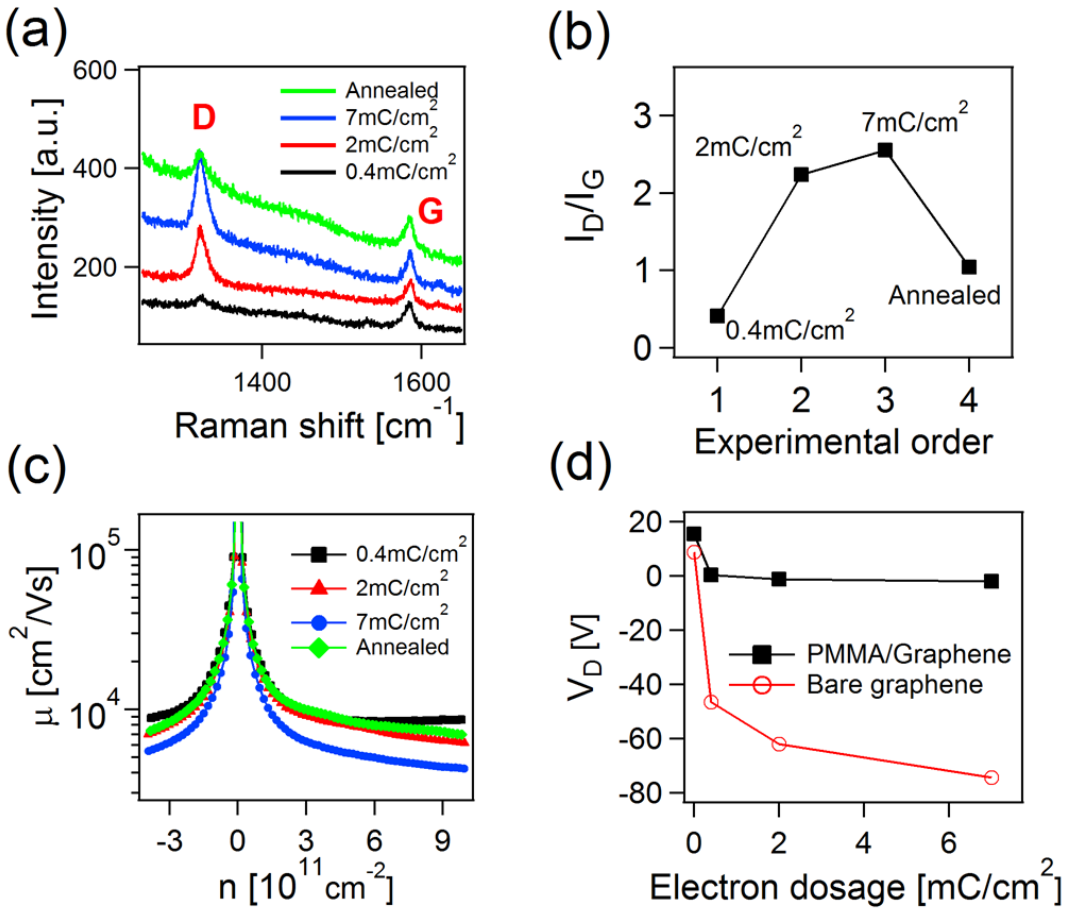

Figure 25 Properties of the graphene FET device after electron irradiation on PMMA/graphene and subsequent removal of PMMA. (a) Raman spectroscopy data, (b) I_D/I_G, (c) mobility, and (d) V_D of the graphene device depending on electron doses irradiated.

In this chapter, we have described the result of the electron irradiation on PMMA/graphene bilayer. In particular, electrical transport properties for pristine graphene, PMMA/graphene bilayers prior to electron irradiation and graphene devices after irradiation on PMMA/graphene with subsequent removal of PMMA. The PMMA/graphene bilayer prior to electron irradiation reveals no Raman 'D' band and

enhanced transport properties, indicating that the PMMA does not interfere with the graphene crystal lattice and serves as a protection layer for graphene from the environment. Upon electron irradiation on the PMMA surface, graphene was hydrogenated during the PMMA depolymerization process. As a result of electron induced hydrogenation of graphene device, their electrical transport properties deteriorated.

CHAPTER V

ELECTRON BEAM IRRADIATION ON GRAPHENE

5.1 Motivation

Graphene is a material that is vulnerable to damage from bombardments of energetic particles. Deterioration of the transport properties of graphene FET devices has been reported due to irradiation from various particles. These include photons [61], ions [63], and electrons [66, 81, 88]. Direct observations of atomic defects induced by ions in graphene have been shown by STM experiments [64]. Changes in the transport properties had also been reported as a consequence of damage induced by ion beams irradiation [63]. Graphene FET devices experience dynamic changes in their transport properties due to irradiation of electron beams with energy less than 30keV (low energy region) and moderate dosages[2] [79, 81]. Experimentally, atomic deficiency in graphene due to electron irradiation has been observed only when the electron energy is higher than 80keV [66, 68]. In those experiments [66, 68], atomic defects in carbon lattices were observed only when an extremely high dose of electrons is used (> $10C/cm^2$). Theoretically, the threshold energy to eject carbon atoms from graphene is 86keV [67], indicating that low energy electron beams rarely create atomic defects. Therefore, changes of transport properties in graphene devices as a result of electron beam

[2] Typical electron dosage during EBL ranges from 0.2 to $0.4mC/cm^2$. In this project, electron dosages less than $10mC/cm^2$ are considered as moderate when compared to electron dosage more than $10^3mC/cm^2$ during TEM for direct observation of lattice defects

irradiation with moderate electron dosage are not ascribed to the atomic defects. Although atomic defects rarely occur in graphene due to irradiation of electrons with energy less than 30keV, the defects signal, a Raman ‘D’ band, appears after irradiation of various ranges of electron beam energy from 100eV to 30keV [79, 83]. Furthermore, graphene devices reveal deterioration of transport properties when irradiated by those low energy electron beams [79, 81]. From modification of transport properties and Raman spectroscopy data, it has been believed that electron beams damage the graphene, altering the crystal structure [76]. However, no clear evidence has been reported as to whether graphene experiences lattice defects or a modification of the crystal structure due to low electron beams irradiation.

Electron beam irradiation on graphene is hardly avoidable because SEM/EBL or TEM are important tools during graphene device fabrication and characterization, indicating that graphene might be exposed to unintended electron beams during the fabrication or characterization processes. Furthermore, electron beams are used to functionalize graphene for use as sensors for biomaterials. For example, graphene devices with nanopores formed by electron beams have been attempted to use for DNA sequencing sensors, which detect changes in transport properties [107, 108]. Therefore, it is important to understand effects of electron beams irradiation on graphene.

5.2 Results and Discussions

In order to study the transport properties of graphene FET devices as a result of electron irradiation, we irradiated graphene with 30keV energy electron beams. As the graphene was irradiated by electron beams with electron dosage of 0.4mC/cm^2, the device revealed changes in the transport properties such as appearance of hysteresis, charge doping, and dynamic changes of entire transport curves. These happened when the irradiated graphene devices kept in a vacuum or were exposed to ambient air or specific gases. Two representative transport curves after electron irradiation on graphene are presented in Figure 26. Generally, our pristine graphene device shows a P-type doping behavior (V_D > 0V) and do not reveal hysteresis when keep in a vacuum, as already shown in Figure 23 (d). Upon irradiation, V_D shifted toward negative gate voltage value (~-50V), indicating that the graphene device was immediately doped with negative charges and converted from the P- to the N-type doped device, as shown in Figure 26. The charge concentration doped due to electron irradiation is calculated by equation 5.1,

$$n = \frac{C_g}{e\Delta V_D}, \tag{5.1}$$

where ΔV_D is change of the Dirac voltage due to electron irradiation, C_g ~11.6nF/cm^2 is the capacitance of SiO_2, n is charge concentration induced by electron irradiation, and e is the elementary charge. After 0.4mC/cm^2 of electron irradiation, the V_D was decreased by ~50V, indicating that graphene was doped with electrons with a concentration of

$4.14*10^{12}/cm^2$. The areal dose of electrons irradiated on graphene ($0.4mC/cm^2$ ~ $2.5*10^{15}/cm^2$) was higher than actual charges doped in graphene ($4.14*10^{12}/cm^2$), indicating that a negligible amount of electrons contributed to electron doping in graphene. In addition to charge doping, the irradiated graphene also revealed hysteresis in the transport properties when sweeping the gate voltage up and down. Furthermore, the transport properties, including V_D and hysteresis of graphene after electron irradiation, changed dynamically as the irradiated graphene kept in a vacuum.

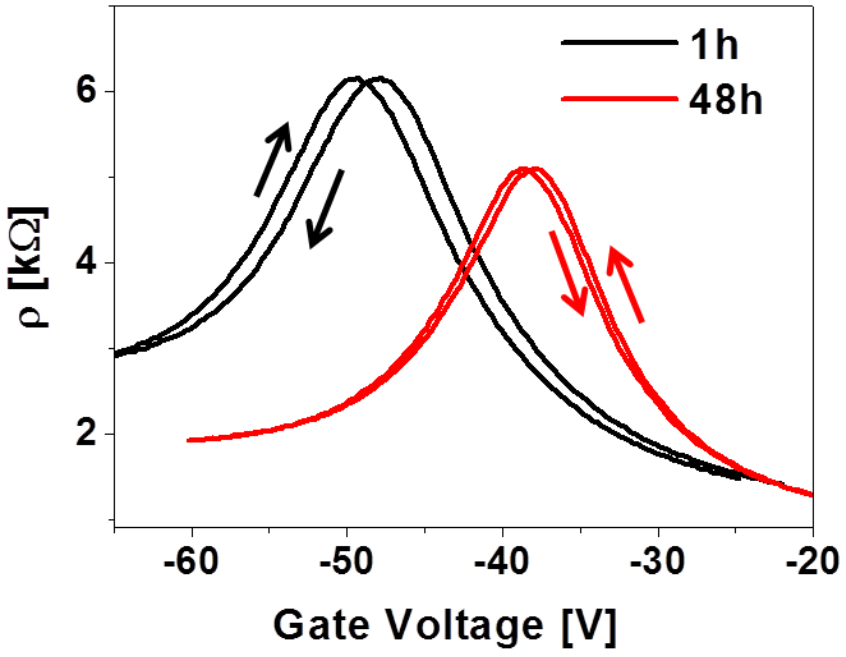

Figure 26 Representative transport properties of graphene devices after electron irradiation. The energy of electron beam is 30keV, and electron dose is $0.4mC/cm^2$. Arrows indicate direction of gate voltage sweep. Black and red curves are measured after 1h and 48h after irradiation while the graphene stay in vacuum.

To study dynamic changes in transport properties of graphene as a result of electron irradiation, we monitored the irradiated graphene in a vacuum for 48 hours. While the graphene device stayed in a vacuum after electron irradiation, the V_D continued to increase, and conductivity was decreased as shown in Figure 27 (a) and (b).

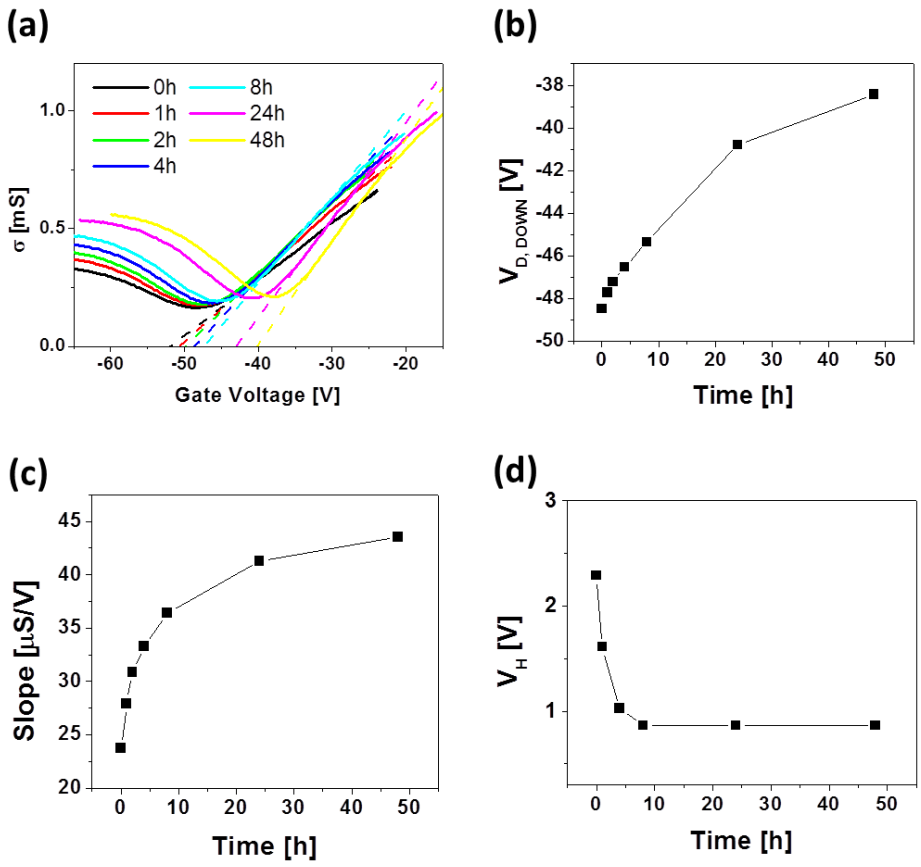

Figure 27 Transport properties of the graphene device in vacuum for 48 hours after electron irradiation. (a) Conductivity with linear fits, (b) $V_{D, Down}$, (c) slope of linear fit from (a), and (d) magnitude of hysteresis which is defined by difference of Dirac points while gate voltage is swept up and down ($V_H = V_{D, Down}-V_{D, UP}$).

When the V_D reached its negative maximum gate voltage value marked as '0h' in Figure 27 (a), it began to recover back toward positive a gate voltage value while in a vacuum. This indicates that the charge doping effect induced by electron beam irradiation was reduced by the vacuum effect. In addition to a reduction of the magnitude of conductivity, a slope of conductivity in the linear region of σ-V_g relation is another measure of charge doping in graphene. Dotted lines in Figure 27 (a) are linear fittings extracted from the linear region of conductivity data, and magnitudes of the slopes are marked in Figure 27 (c). As the duration of time graphene sits in a vacuum after electron irradiation increases, the slope also increases. This can be interpreted as a reduction of charged electrons in graphene. The Relationship between the slopes and the concentration of charged impurities is described by the equation 2.30, $\boldsymbol{\sigma} = \frac{Ce^2}{h}\left|\frac{n}{n_i}\right| + \boldsymbol{\sigma}_{res}$, which implies that a slope of conductivity in the σ-V_g relation far from the V_D is inversely proportional to the concentration of electrons doped in graphene. Therefore, alteration of slopes of the linear fittings in the conductivity data is caused by changes in a charge concentration.

Another interesting feature of the conductivity as a result of irradiation is that flattened and widened plateau becomes narrow as time passes in a vacuum. By comparing '0h' and '48h' in Figure 27 (a), the transport curve marked '1h' is wider than '48h' near the V_D, which is also deduced from variation of slopes far from the V_D. At the V_D, which is a gate voltage where an average charge concentration is zero, the conductivity does not drop to zero because hole-electron puddles contribute to

conduction [46, 52]. The fact that the width of the plateau near the V_D decreases in a vacuum is ascribed to a reduction of electron-hole puddles as doped charges decreases.

Hysteresis is another interesting feature that appeared as a consequence of electron beam irradiation on graphene. The magnitude of the hysteresis, $V_H = V_{D,\,Down} - V_{D,\,Up}$, decreased from 2.29V to 0.86V while the irradiated graphene stayed in a vacuum but did not completely disappear. Instead, the magnitude of hysteresis remained constant after 8 hours, as shown in Figure 27 (d).

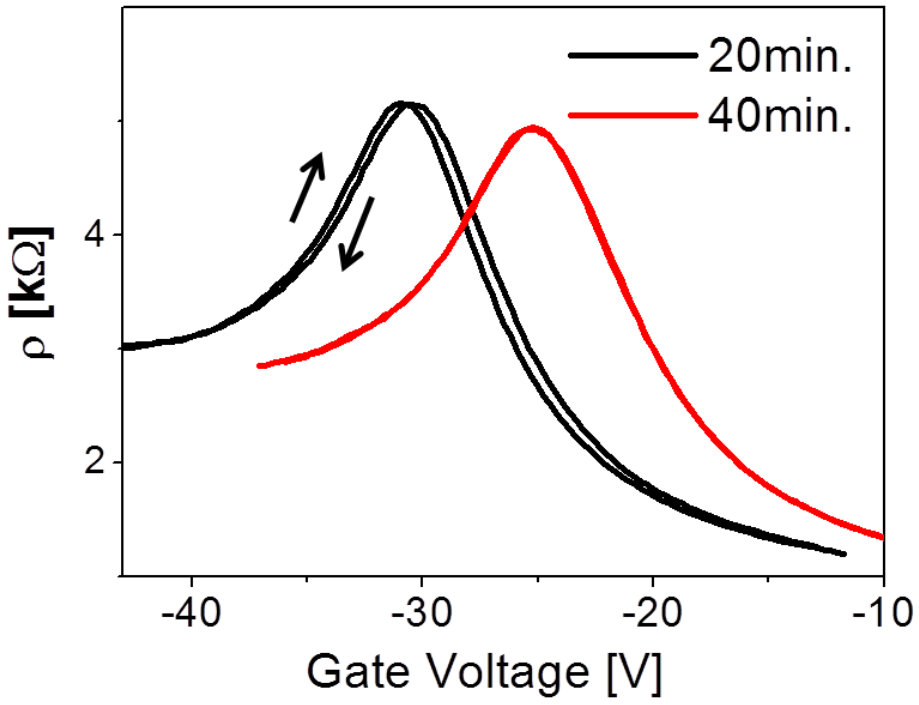

Figure 28 Transport properties of the irradiated graphene after exposure to ambient air molecules. Arrows indicate the direction of gate voltage sweep.

In order to investigate the transport properties further, we exposed the irradiated graphene to ambient air after it had stayed in a vacuum for 48 hours. After exposing the irradiated graphene device to ambient air for 20 minutes, V_H was reduced from 0.87V to 0.41V as shown in Figure 28. Additional exposure to air for 20 minutes completely eliminates the hysteresis. Ambient air molecules are known as P-type dopants. In particular, a mixture of H_2O and O_2 molecules abundant in ambient air accepts electrons from graphene by a Redox coupling process [96, 109, 110], which is in agreement with the observation that V_D moves toward a positive gate voltage value as shown in Figure 28.

Detailed description of the transport properties in ambient conditions is after electron beam irradiation on graphene shown in Figure 29. All transport measurements were conducted in a vacuum after exposure of graphene to ambient condition. As a consequence of interaction of the irradiated graphene with ambient molecules, the transport properties recovered to their initial state as shown in Figure 29 (a), which is the same behavior as the irradiated graphene in a vacuum. It is a reasonable speculation that changes of the transport properties when the irradiated graphene is exposed to ambient air is due to adsorption of air molecules. As a result of exposure of the irradiated graphene to air, the V_D and the conductivity were increased, which were dependent on exposure time as shown in Figure 29 (a) and (b). Although the irradiated graphene showed similar transport behaviors in a vacuum and in ambient condition, the speed of changes in the transport properties was accelerated, which is ascribed to a density of

molecules near graphene. For example, the V_D increased only 10V for 48 hours in a vacuum but increased 35V after exposure to air for 12 hours. Our results that changes of the transport properties due to electron irradiation are in accordance with previous work that graphene was doped with electrons due to electron irradiation and recovered to its initial state as the graphene device is exposed to ambient air [79]. This result supports our speculation that changes in the transport properties of the irradiated graphene are caused by adsorption of environmental molecules on graphene. In pristine graphene, molecular adsorption in ambient air is governed by the Redox coupling process. Therefore, alteration of the transport properties of the irradiated graphene originates from the same mechanism of pristine graphene, which is called the Redox process.

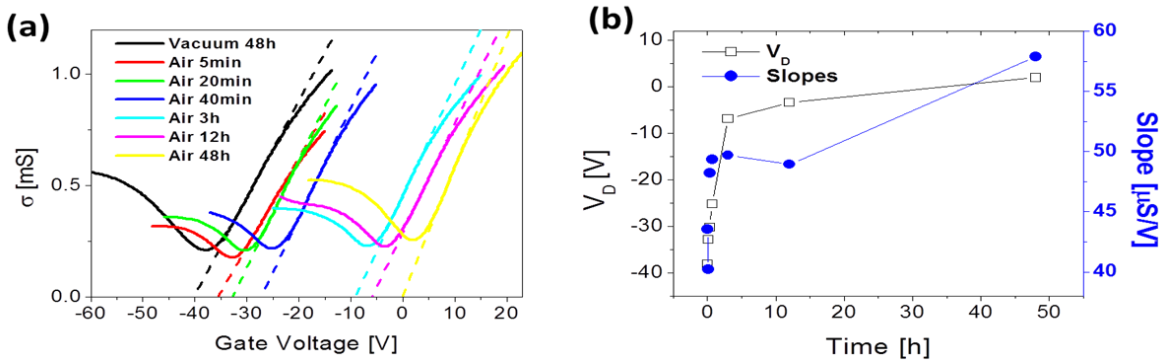

Figure 29 Transport properties of the irradiated graphene after exposure to ambient condition. (a) Conductivity with linear fits. (b) The Dirac points and values of slopes shown in (a).

An additional electron beam with an electron dose of 2mC/cm^2 was irradiated on the graphene device to investigate the dynamic behaviors of the transport properties further. Except for initial variation of both the V_D and the magnitude of resistivity, the transport properties revealed similar behaviors as in the case of irradiation 0.4mC/cm^2 electron dose, as shown in Figure 30. As a result of electron irradiation with elevated electron dosage, the entire transport curve was shifted to a negative gate voltage and recovered as it was kept in a vacuum and exposed to ambient air. However, the variation of the V_D induced by additional irradiation did not increase linearly proportional to the electron dosage. Despite the elevated electron dose (2mC/cm^2), which is five times higher than the initial irradiation with electron dosage (0.4mC/cm^2), the V_D shifted to -70V as shown in Figure 30 (a) and (b). We find that charge doping in graphene due to electron irradiation is not proportional to the irradiated electron dosages, allowing us to consider that irradiated electrons are not doped directly in graphene. We also find from electron irradiation experiments that the dynamic behaviors of the transport properties of graphene devices are a general feature. In addition, reduction of induced charge by electron irradiation is also a general behavior when ambient molecules interact with graphene, which is indicated by slopes of conductivity as shown in Figure 30 (c) and (d). From successive irradiation experiments, we find that the magnitude of resistivity, the magnitude of V_D, and the slopes extracted from the conductivity of the irradiated graphene are changed by the same origin, adsorbates on graphene. Therefore, we speculate that adsorption dynamics of molecules on graphene is the key to understanding

the electrical transport properties of graphene FET devices as a result of electron irradiation. Based on the fact that dynamic behaviors of the transport properties in a vacuum are similar to that in ambient condition, we can also speculate the transport properties change by that same mechanism. In other words, as molecules adsorb on graphene in ambient condition, dynamic behaviors of the transport properties of the irradiated graphene in a vacuum is the result of molecular adsorption on graphene.

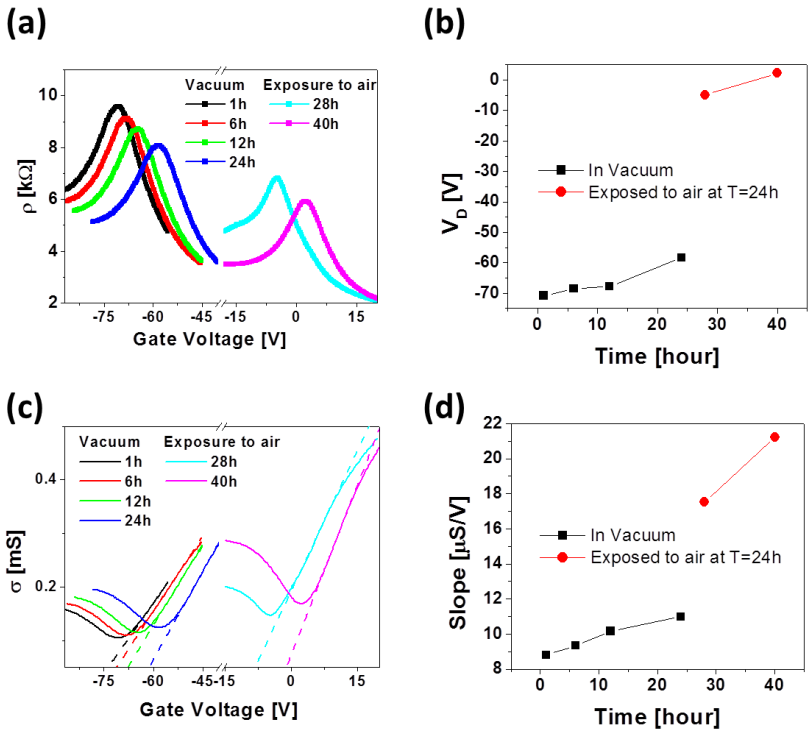

Figure 30 Transport properties of the graphene FET device as a result of additional electron irradiation with electron dose of 2mC/cm^2. Changes in transport properties in a vacuum for 24 hours and after exposed to ambient condition are shown. (a) Resistivity, (b) Dirac point (V_D), (c) conductivity with linear fits, and (d) magnitudes of slopes shown in (c).

To study defects generated by electron beam irradiation on graphene further, we investigated the surface topography using an AFM. Although we cannot observe atomic defects generated by electron beam irradiation with an AFM, we expect that molecules should be observed on graphene if the Redox process is the origin of changes in the transport properties.

AFM images, including height and phase shift, are shown in Figure 31. We conducted tapping mode AFM experiments in ambient conditions after Raman spectroscopy experiments and observed the changes in the surface morphology on graphene, which was induced by electron beam irradiation as shown in Figure 31.

First of all, AFM images of a pristine graphene device in 10um scale are shown in Figure 31 (a). Other AFM images were obtained from 1um square area indicated by the blue doted area in Figure 31 (a). The pristine graphene as shown in Figure 31 (b) and (c) reveals impurities on the surface. Although the pristine graphene unavoidably shows adsorbates on its surface, they do not cause the Raman 'D' band as shown in Figure 32. Those adsorbates might appear on graphene during the device fabrication process and contribute to make transport curves asymmetric between holes and electrons conduction regions, which is generally shown in our graphene devices [111].

After an electron dose of 0.4 mC/cm^2 was irradiated on graphene, the surface morphology began to change as shown in Figure 31 (d) and (e). In particular, adsorbates at identical locations (indicated by an arrow and near the tail of the arrow) became slightly bigger, and the coverage of adsorbates on graphene increased. Although the

evolution of the surface morphology is not clearly shown in the height image, the phase shift image reveals alteration of the surface morphology clearly. These behaviors were significantly enhanced when an increased electron dose was irradiated as shown in Figure 31 (f) and (g).

After additional electron irradiation of $2mC/cm^2$, it is confirmed that adsorbates consolidated and became bigger as shown in Figure 31 (g). To analyze detailed changes in the surface morphology due to the additional electron irradiation, we selected a cluster of adsorbates, which is marked by arrows in the AFM images and studied the variation of height profiles as shown in Figure 31 (h), (i), and (j). In pristine graphene, we find two separate accumulations of adsorbates marked in Figure 31 (b) and corresponding height profile is shown in Figure 31 (h). This height profile shows that two distinct adsorbates are separated. As a $0.4mC/cm^2$ areal dose of electrons was irradiated, the height of the adsorbates slightly decreased and the graphene area between the two adsorbates is filled in by adsorbates. This was confirmed by an increase of the height in the intermittent area as shown in Figure 31 (i). These behaviors were enhanced by additional irradiation as shown in Figure 31 (j). The height of adsorbates was reduced to half, and the intermittent area was completely filled in by adsorbates, which is visualized in Figure 31 (g). It is clear that adsorbates accumulations induced by exposing the irradiated graphene to air are chemically different from graphene and develop into granular adsorbates of increasing size. We interpret the granular shaped adsorbates

accumulations as the result of consolidation of adsorbates by exchange of electrons between graphene and environmental molecules, caused by the preceding irradiation.

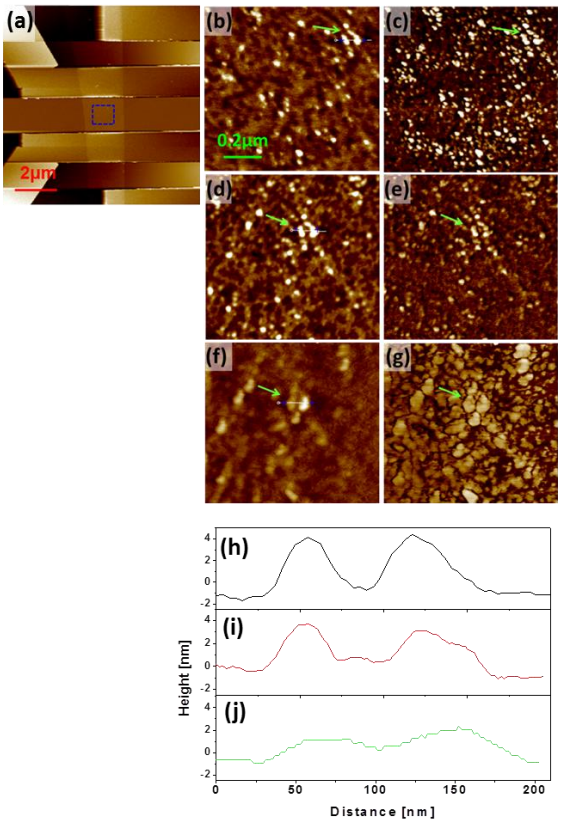

Figure 31 Surface topographs of pristine graphene and irradiated graphene by electron beams with dosages of 0.4 and 2mC/cm^2. (a) AFM images of pristine graphene FET device. The scale bar is 2um. Blue dotted area is a 1um by 1um square. Other AFM images (b)-(g) are obtained from the square area. (b), (d), and (f) are height images of pristine, 0.4, and 2mC/cm^2 irradiated graphene, respectively. (c), (e), and (g) are phase shift images corresponding to (b), (d), (f). Arrows indicate physically the same adsorbates at the same position on graphene. Height profiles (h), (i), and (j) are obtained cluster of adsorbates marked by arrows in (b), (d), and (f), respectively.

Taking into account the experimental result that the Raman ‘D’ band is caused by molecular adsorption [105], it is reasonable to suspect that those adsorbates on graphene surface interrupt vibration of carbon atoms in lattice and activated the Raman ‘D’ band. Therefore, the surface morphology can be explained by a Redox coupling process in that the amount of electrons accumulated by electron irradiation determines the adsorption of environmental molecules on graphene. This idea is further supported by Raman spectroscopy data. The Raman ‘D’ band appeared after electron beam irradiation as shown in Figure 32, which is customarily interpreted as adsorbates on graphene tightly binding with graphene so that the intrinsic vibrations of carbon atoms are impeded [90]. This effect was enhanced significantly by an increased irradiation dose of electrons ($2mC/cm^2$) based on the fact that the Raman ‘D’ band increases with increasing electron dosages, which is in agreement with interpretation of AFM images.

After transport measurements, we obtained Raman spectrum conducted in ambient conditions. As a result of electron irradiation on graphene, we observed the Raman ‘D’ band in Figure 32, which is a signature of defects in graphene and an agreement with previous works [76, 79, 81]. We also observed that the intensity of the ‘D’ band increased with increasing electron dosages. Teweldebrhan et al. argued that graphene experiences an amorphization trajectory as a result of electron irradiation, indicating that bombardment of electrons on graphene induces transformation of the crystallographic structure. The idea of the amorphization trajectory is based on the

theory that lateral size of grains can be determined by relative intensity of 'D' versus 'G' band in Raman spectrum as shown in equation 5.2,

$$\frac{I_D}{I_G} = \frac{C(\lambda)}{L_a}, \tag{5.2}$$

where $C(\lambda)$ is a constant related to wave length of excitation laser, L_a is effective crystal size of graphene, I_D is intensity of D band, and I_G is intensity of G band in Raman spectrum [90]. Making use of equation 5.2, Ferrari and Robertson proposed the amorphization trajectory, which classifies crystallographic status of graphene into three stages: graphite, nanocrystalline graphite, and amorphous carbon [91, 112].

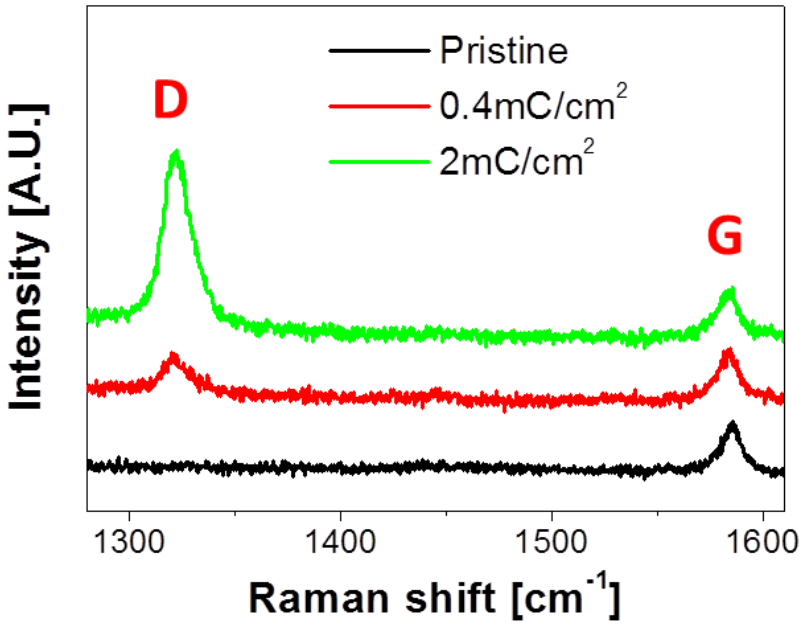

Figure 32 Raman spectroscopy data of the graphene devices irradiated by electron beams with electron dosages ranging from 0 to 2mC/cm^2.

However, Raman spectra not only respond to structural defects, but also respond to any kind of defects, such as molecular adsorption, which break symmetric vibration of the A_{1g} mode in graphene. In other words, Raman spectra alone cannot determine defect types activated in graphene due to electron irradiation. In our experiments, we also observed that the intensity of 'D' band increased as an electron dosage increased, an indication that the amount of defects induced in graphene was increased.

In order to investigate the mechanism of molecular adsorption on graphene as a result of electron beam irradiation, we studied the Redox process in graphene. According to the Redox coupling theory, electrons transfer between graphene and molecules until the Fermi energy level of graphene aligns to that of the Redox system as shown in Figure 33 [96, 109].

As water and oxygen adsorb to graphene, electrons transfer from graphene to the environmental molecules. Adsorption and consolidation of the molecules on the graphene surface continue until the Fermi energy level of graphene is aligned with the Redox states located at -4.83eV and -5.66eV with respect to the vacuum energy level. Chemical reactions for the Redox process are shown by 5.3 and 5.4 [96, 109].

$$O_2 + 2H_2O + 4e^- \leftrightarrow 4OH^- \tag{5.3}$$

$$O_2 + 4H^+ + 4e^- \leftrightarrow 2H_2O. \tag{5.4}$$

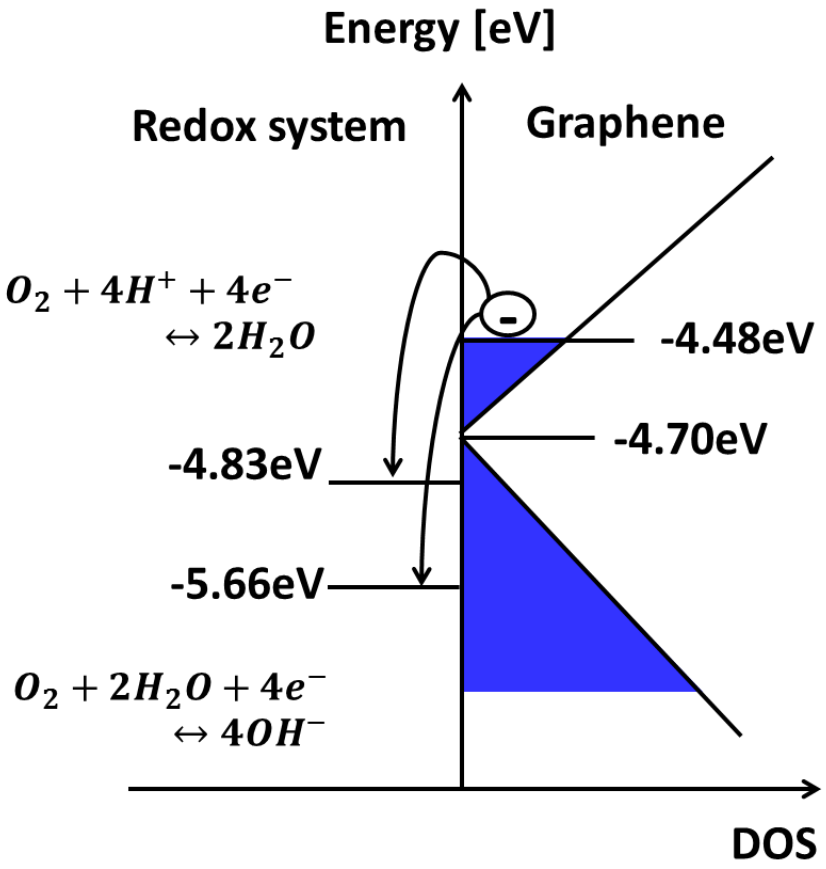

Figure 33 Schematic diagram of energy level of electron in graphene and Redox system.

The Dirac point of ideally clean graphene is located at -4.7±0.05eV, which is higher than the Fermi energy level of the Redox states [113]. When the Fermi energy level of graphene is decreased and aligned with the Redox states, the graphene/Redox system reaches an equilibrium state. The fact that the Dirac point sticks at the

equilibrium point regardless of electron dose indicates that pristine graphene should reveals a P-type doping behavior, as our pristine graphene devices shows.

We observed that graphene was doped electrons due to electron irradiation by alteration of the transport properties. Therefore, exposure of the graphene device to electron beams elevates the Fermi energy level of graphene. The Fermi energy of graphene after electron irradiation with electron dosage of 0.4mC/cm^2 can be calculated by equation 5.5.

$$n = \int_0^\infty D(E)f(E)dE \tag{5.5}$$

Here, $D(E) = \frac{E}{\pi(v_f\hbar)^2}$ is density of state of graphene, and the $f(E) = \frac{1}{1+\exp((E-E_F)/k_BT)}$ is the Fermi-Dirac distribution function. The equation 5.5 is derived to equation 5.6.

$$n = \frac{2}{\pi(v_F\hbar)^2}(k_BT)^2F_1(\varepsilon_F) \tag{5.6}$$

Here, $F_1(\varepsilon_F)$ is the Fermi-Dirac integral of order 1, which is defined by $F_1(\varepsilon_F) = \int_0^\infty \frac{\varepsilon}{1+\exp(\varepsilon-\varepsilon_F)}d\varepsilon$, k_B is the Boltzmann constant, T is the temperature, and $\varepsilon_F = \frac{E_F}{k_BT}$. Because the $F_1(\varepsilon_F)$ cannot be solved analytically, we try to find asymptotic expression of the $F_1(\varepsilon_F)$, which is categorized according to magnitude of ε_F. In order to estimate ε_F, we first calculate the Fermi energy at Tis zero Kelvin. At T=0K, the Fermi integral of order 1, $F_1(\varepsilon_F)$ is simplified to ${\varepsilon_F}^2/2$, which simplifies the equation (5-6) to equation 5.7.

$$n = \frac{1}{\pi\left(v_f \hbar\right)^2}(k_B T \varepsilon_F)^2 \tag{5.7}$$

Here, a carrier concentration can be obtained from the variation of the V_D of graphene devices due to electron irradiation. When the V_D shifts 50V as a result of electron beams irradiation, the induced charge concentration is $-3.62*10^{12}cm^{-2}$, which is calculated by $n(V_g = -50V) = -50V*C_g/e$, where C_g~11.6 nF/cm^2 is the capacitance of gate oxide and e is the elementary charge. We found that the Fermi energy was increased by 0.22eV at T=0K by combining the charge concentration induced by electron irradiation ($-3.62*10^{12}cm^{-2}$) and the equation 5.7. To calculate equation 5.7 at T=0K, the Fermi velocity of the graphene, v_f~10^6 m/s, is used [35]. We make use of the asymptotic expression of $F_1(\varepsilon_F) \sim {\varepsilon_F}^2/2$ to evaluate the equation 5.6, resulting into the equation 5.7 [114].

In order to investigate further the mechanism of the Redox process in graphene after electron irradiation, we exposed the irradiated graphene to individual O_2 and H_2O gases. In Redox gas exposure experiments with pristine graphene, individual H_2O and O_2 gases reveals different doping behaviors and are known as an electron donor and an electron acceptor, respectively [96]. In our experiments, when the irradiated graphene was exposed to H_2O, the transport curve shifted toward a negative gate voltage value, indicating that water molecules serve as electrons donor as shown in Figure 34 (a), which is in agreement with the chemical reactions 5.3 and 5.4. Upon exposure of the irradiated graphene to H_2O, large initial hysteresis (5.66V) appears and reduces to 2.37V

after successive measurements. In contrast to ambient air, adsorption of H_2O molecules on graphene keeps at the hysteresis more than 2V after successive measurements.

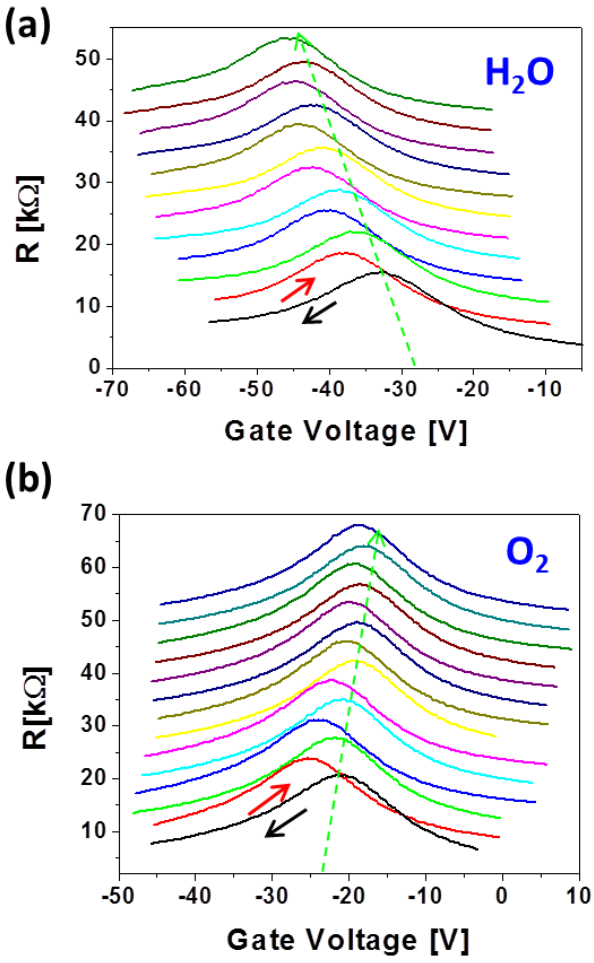

Figure 34 Transport properties of graphene FET devices irradiated by an electron beam with electron dose of 0.4mC/cm^2 and subsequently exposed to (a) H_2O and (b) O_2. Black and red arrows indicate directions of gate voltage sweep directions. Offset only along y axis sets. Successive measurements are shown from bottom to top. Green dotted arrows are guideline for V_D shift.

It is considered that the electronically polar nature of water molecules cause hysteresis in the graphene devices, which is in agreement with previously published works with graphene and CNT [96, 99]. In contrast to water, oxygen molecules act as electron acceptors, indicated by a shift of the transport curve toward a positive gate voltage. Although the irradiated graphene also reveals a large hysteresis initially, the hysteresis is reduced to 0.86V, which is a typical value the irradiated graphene reveals in a vacuum after electron irradiation. This indicates that oxygen does not interfere with hysteresis when the graphene in oxygen environment reaches a steady state. In addition, the amount of charge doping in graphene indicated by the variation of V_D is different from those two gases. While the V_D increased 2V in oxygen, it decreased 10V in H_2O environment during 6 successive measurements, which is in accordance with the Redox gas exposure experiment of pristine graphene [96]. Furthermore, those gas adsorption experiments can be explained by chemical reactions 5.3 and 5.4. Therefore, water and oxygen gas exposure experiments support the idea that adsorption of ambient molecules on the irradiated graphene by electron beams is governed by a Redox process.

So far, we observed that graphene FET devices reveal a signature of defects indicated by Raman ‘D’ as a result of electron beam irradiation. In addition, we directly observed that the irradiated graphene adsorbed environmental molecules in ambient air as a consequence of a Redox process. It is reasonable to consider that charge carriers experience scattering by adsorbates on graphene produced by electron irradiation and subsequent molecular adsorption. In order to investigate effects of the surface

morphology induced by molecular adsorption on electrical properties, transport measurements of the graphene device were conducted after AFM experiments. From conductivity data shown in Figure 35, it is verified that molecular adsorption induced by electron irradiation deteriorates the transport properties of the graphene device. In addition, conductivity depends on electron dosages irradiated on graphene because defect states in graphene are dependent on electron dosage irradiated, which is consistently interpreted with AFM images as shown in Figure 31 and the Raman spectroscopy data in Figure 32. However, the transport behaviors shown in Figure 35 are different from that measured in a vacuum. Above all, the Dirac points were recovered to original value regardless of electron dosages irradiated, which means that artificially doped charges were removed. In other words, the transport properties are not governed by charged impurities described by the equation (2-30). Instead, neutral defects induce carrier scattering in graphene. Theory of carrier scattering by neutral defects was modeled by introducing a deep potential well, which is described by equation 5.8.

$$\sigma_d = \frac{2e^2}{\pi h}\frac{n}{n_d}\, ln^2(k_F R) \tag{5.8}$$

Here n_d is density of neutral defects is, k_F is the Fermi wave vector, R is the radius of potential well generated by the defect. The equation 5.8 is experimentally supported by ion irradiation experiments [63]. In contrast to neutral defects generated by ion irradiation, the adsorbates generated on graphene samples due to electron irradiation cover the entire surface. This makes it difficult to define the radius of a potential well in

equation 5.8. Nevertheless, the theory of carrier scattering by defects reveals that there is a linear relationship between conductivity and a carrier concentration. Furthermore, the conductivity is inversely proportional to defect density, which indicates that the slope of the conductivity far from the Dirac point is a measure of adsorbates concentration. The argument that the transport properties are degraded as a result of electron irradiation was supported by unusual results of quantum Hall effect experiments [79]. Therefore, deterioration of the transport properties of graphene FET devices due to electron irradiation and subsequent exposure to ambient conditions is originates charge carrier scattering due to neutral adsorbates.

Another remarkable property of the conductivity data in Figure 35 is a broadening of the valley near the $V_{D.}$ In the case of a graphene FET, irradiated by electrons and exposed to air, the V_D is nearly identical to that of pristine graphene regardless of electron dosage, however the valley near the V_D is broadened as the charged impurity concentration increased due to electron irradiation, which is in accordance with previous charge doping studies [46, 52, 115]. Although doped charges due to electron irradiation are neutralized on average in ambient conditions by adsorption of environmental molecules, the local fluctuations of charge density, which contribute conductivity at the V_D, increases with increasing electron dosage even after the V_D is fully recovered. We therefore agree that the increased charge density fluctuation induced by e-beam irradiation increases hole-electron puddles, thereby increasing the plateau around the V_D.

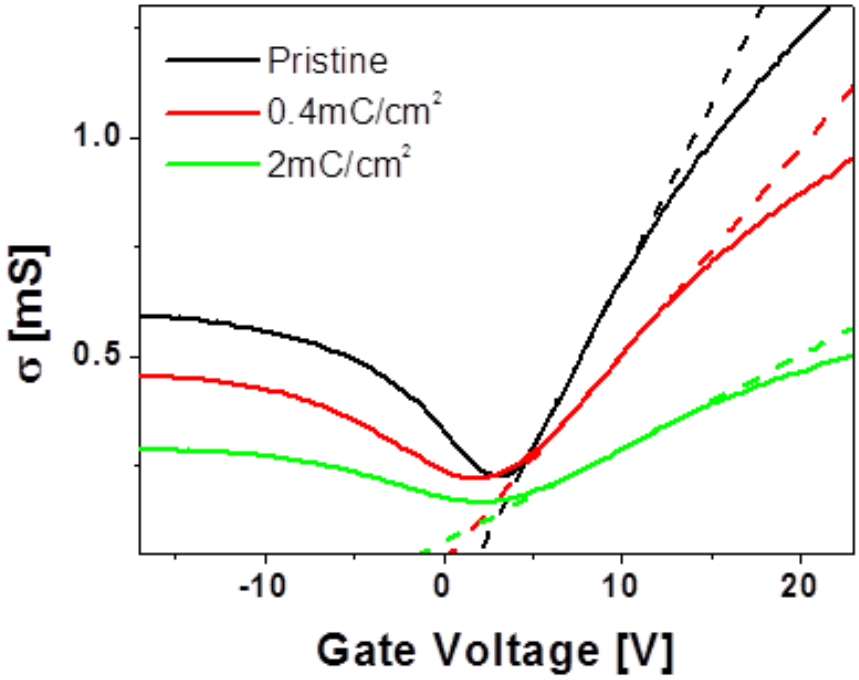

Figure 35 Conductivity of the irradiated graphene FET device and subsequently exposed to ambient air until the Dirac point recovers to that of pristine graphene. Dashed lines indicate linear fittings in the linear region of the conductivity data.

5.3 Hysteresis and charge doping by electron beams irradiation

As a consequence of electron beams irradiation, the graphene device reveals hysteresis, which is defined by the discrepancy of the Dirac voltages during sweeping up and down the gate voltage. We define the hysteresis (V_H) by equation 5.9.

$$V_H = V_{D,Up} - V_{D,Down} \tag{5.9}$$

Here $V_{D,\,Up}$ and $V_{D,\,Down}$ are the Dirac voltage obtained during sweeping down and up the gate voltage, respectively. The hysteresis phenomenon has been reported and studied in carbon materials including graphene and CNT in various conditions. Defects [116] and chemical residues during the fabrication process [117] are considered as candidates to induce hysteresis in the transport properties. Trapped charges in the SiO_2 layer [89] or interface between graphene and the SiO_2 layer [118] are also considered as a cause of hysteresis by transferring of the trapped charges by an applied electric field. An ambient condition is a commonplace where hysteresis appears in both graphene or CNT FET devices, which presumably originates from dipolar molecules on the surface of graphene or CNT [85, 89, 96, 98, 99, 101, 119, 120].

In addition to dynamic behaviors of graphene due to electron irradiation, we also observed hysteresis, which appeared in the graphene device as discussed in the previous section. General behaviors of hysteresis have already been introduced in an earlier part of this chapter. Because our pristine graphene does not show hysteresis as shown in Figure 23, hysteresis is a phenomenon that appears as a consequence of interaction between graphene and energetic electrons. Upon irradiation, graphene reveals hysteresis, V_H ~2V which is small compared with the total charge induced by electron irradiation (ΔV_D~50V) in graphene as shown in Figure 27. This implies that only a small portion of charge induced by electron irradiation contributes to hysteresis, indicating that there might be different origins of the hysteresis and charge doping in graphene.

The steady state value of V_H (0.87V) in a vacuum did not disappear until the graphene device was exposed to ambient air as shown in Figure 28. Once hysteresis disappears as a result of adsorption of air molecules on graphene, it does not appear again, indicating that all the charges contributed to hysteresis are neutralized by air molecules. Although hysteresis completely disappears after exposure of graphene to air for 40 minutes, the V_D did not completely recover to its initial value as shown in Figure 28. This implies that the charges related to hysteresis are of a different type from dopants that induce variation of the V_D. Based on the fact that the Raman 'D' peak appears and increases according to electron dosages irradiated on graphene as displayed in Figure 32, we consider that environmental molecules adsorb on graphene.

In contrast to our speculation that charge doping in graphene due to electron irradiation originates from molecular adsorption, He et al. [79] and Childres et al. [81] argued that charge doping in graphene due to electron irradiation is related to an oxide layer underneath graphene. In order to elucidate whether the oxide layer plays an critical role in charge doping process in graphene, we fabricated suspended graphene for electron irradiation experiments. SEM images of top view and angled view are shown in Figure 36 (a) and (b), respectively. From the SEM image in Figure 36 (b), we verified that the graphene was suspended between two electrodes after etching out the oxide layer. Once suspension of graphene was verified, we heated the suspended graphene at 200°C for 5 minutes in a vacuum. This is to remove anything adsorbed on graphene during the drying a process in CO_2 environment, during fabrication of suspended

graphene, or contamination in ambient conditions. After cleaning the suspended graphene by heating in the transport measurement chamber, we obtained the transport data from suspended graphene prior to electron irradiation. As shown in Figure 36 (c), the V_D locates around -4V, revealing that the suspended graphene prior to electron irradiation is slightly doped with negative charges.

In general, cleaning the graphene devices by heating in a vacuum shifts the V_D toward a negative gate voltage value, and the amount of shift of the Dirac point depends on annealing time [97]. After obtaining the transport data from pristine graphene, we irradiated an electron beam on the suspended graphene and measured resistance which showed that the suspended graphene was doped with negative charges as supported graphene by oxide layer. Therefore, the majority of charges doped as a result of electron irradiation indicated by a shift of the V_D are the result of adsorption of molecules on graphene.

Once the fact that charge doping as a result of electron irradiation originates from adsorption of molecules, we investigated the origin of the hysteresis. Because the V_D moved to a negative gate voltage value, electrons were doped in graphene. In contrast, the charges that contribute to hysteresis switch their charge type from positive to negative or vice versa according to the carrier type in graphene, implying that the charges respond to vertical electric field generated by charge carriers in graphene.

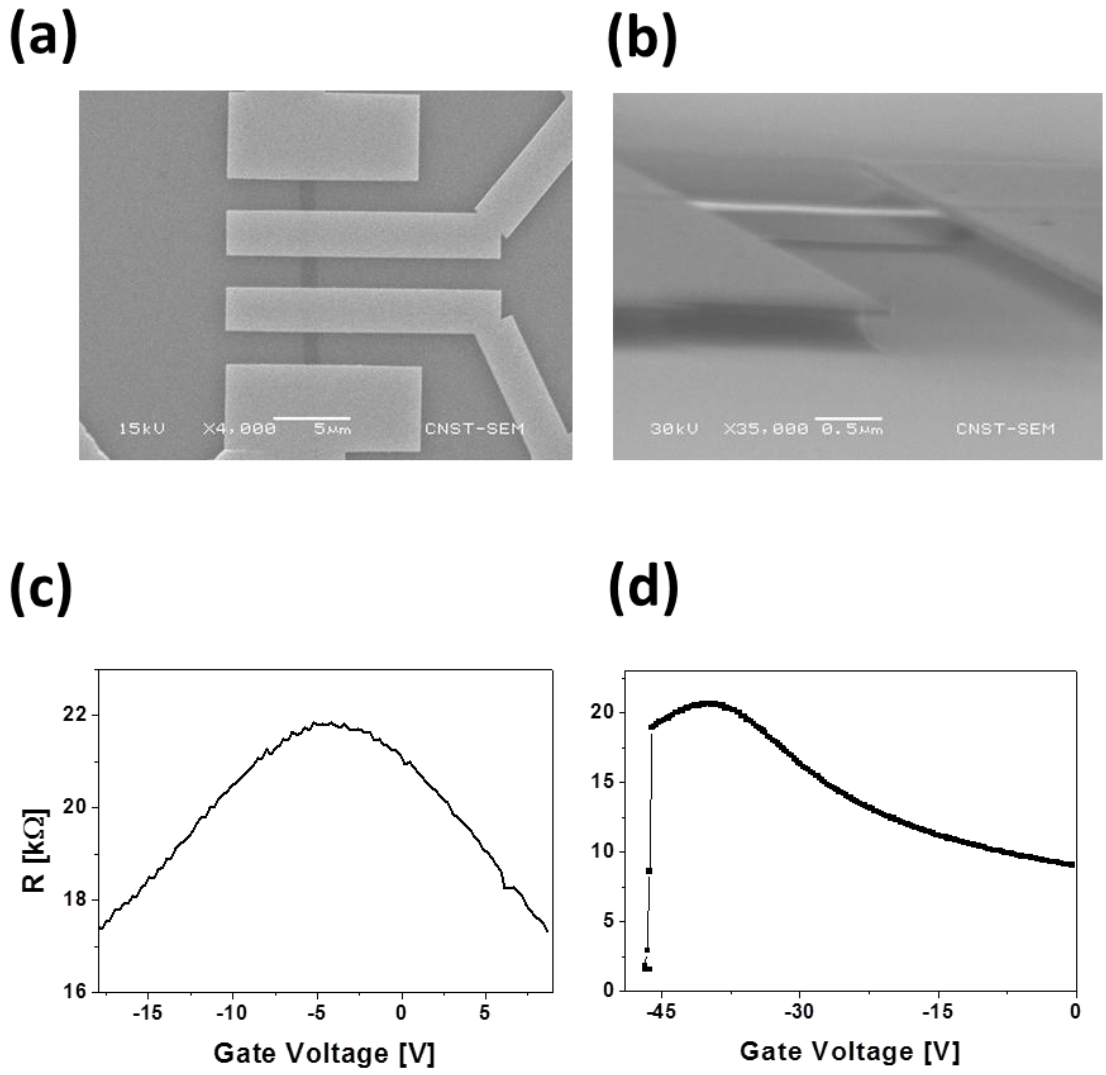

Figure 36 Suspended graphene. (a) top view and (b) angled view of SEM images of suspended graphene. Resistance data (c) before and (d) after irradiation of electrons with 0.4mC/cm^2 dose.

One possible scenario of the hysteresis appearance is that charge gets trapped in an oxide layer or interface between graphene and an oxide layer. Unfortunately, the role

of an oxide layer underneath graphene cannot be proved by obtaining the transport properties with suspended graphene because it collapses down during charge carrier modulation due to electrostatic force induced by the charge carrier. Although we cannot show experimentally that the oxide layer does not contribute directly to hysteresis by charge traps, it is difficult to accept the scenario because charge trap density in an oxide layer or in the interface will not be affected by adsorption of air molecules on graphene. Instead, it is speculated that adsorbates on top of graphene with polarity which are generated during electron irradiation induce hysteresis because hysteresis is removed by adsorption of ambient molecules as shown in Figure 28.

In order to investigate hysteresis further, in-situ annealing experiments were conducted. As shown in Figure 37, hysteresis appeared due to electron irradiation and reduced from 1.47V to 0.24V as a result of 1 minute-annealing around 200°C as shown in Figure 37. Hysteresis disappeared completely within 5 minutes by annealing around 200°. Because the depth of electron trap energy levels in a thermally grown oxide surface is 2.13 ± 0.05 eV [121], a few tens of meV (thermal energy of around 200°C) rarely makes the trapped electrons escape from trapped states. In other words, hysteresis cannot be removed by an annealing effect at 200°C if the trapped charges in an oxide layer are the cause of hysteresis. Therefore, we rule out one possible cause of hysteresis, charges trapped in an oxide layer [122].

One remarkable aspect of the annealing effect is that the hysteresis, V_H, decreased quite abruptly from 1.29V to 0.12V after 1 minute of annealing while the V_D

remained unaltered. This indicates that the adsorbates that induce negative charge doping are different from the adsorbates that induce hysteresis as shown in Figure 37 (a). We argue that the origin of hysteresis is adsorbates, which are so weakly bound on graphene that they are removed by annealing for a short period of time. Furthermore, the hysteresis completely disappeared after annealing for 5-minutes. From these results, we conclude that the hysteresis originates from adsorbates, which are so weakly bound on graphene that they are desorbed during a short period of annealing compared with adsorbates that induce charge doping which are more resilient. Presumably, environmental molecules such as O_2 and H_2O are the main causes of hysteresis because they are abundant in air and likely to remain on graphene even after evacuation of the EBL chamber. They can also undergo electronic excitation, ionization, and electron attachment by electrons with energies ranging from ~eV to keV [123, 124], which is comparable to energies of backscattered or secondary electrons. Especially, molecules with missing or surplus electrons might physically remain on graphene with switchable electronic polarity. Although it is difficult to confirm which particular species induces hysteresis, we suggest that environmental molecules which have polarity are the origin of the hysteresis due to electron irradiation.

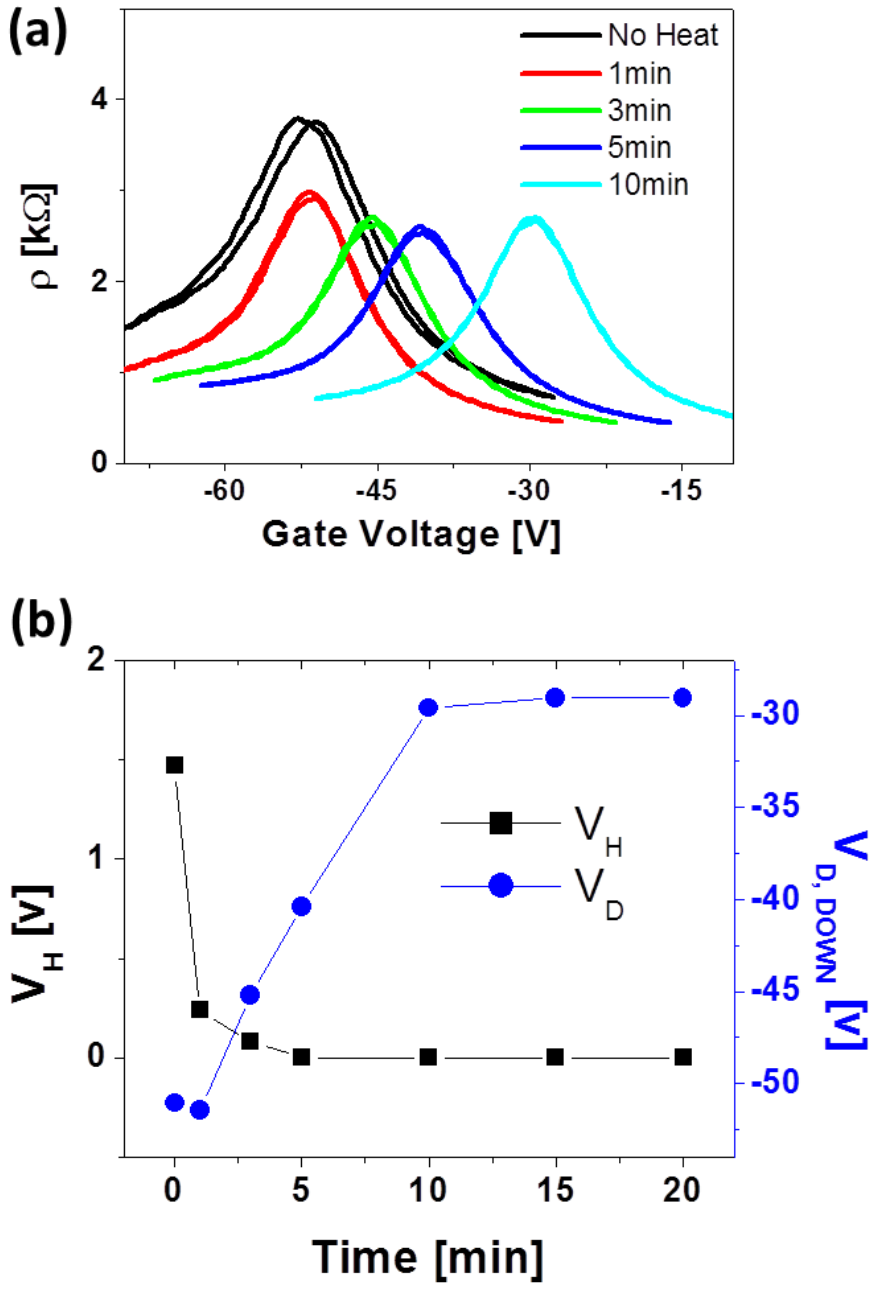

Figure 37 Transport properties of the irradiated graphene with electron dosage of 0.4mC/cm^2 during annealing around 200°C in vacuum. (a) Resistivity and (b) Magnitude of hysteresis and the Dirac point during sweeping down gate voltage.

CHAPTER VI

SUMMARY AND FURTHER USEFUL RESEARCH

The main purpose of this research project was to study transport properties of graphene field effect transistor devices as a result of electron beam irradiation. The graphene FET devices showed dynamic transport properties after electron irradiation in vacuum. Upon irradiation of graphene with an electron beam, V_D shifted to negative gate voltage which is an indication of electron doping on graphene. With increasing time in vacuum, V_D increased gradually for 48 hours. Once the irradiated graphene was exposed to ambient conditions, V_D increased and recovered to its initial value in a few hours. At the same time, the resistivity increased but did not recover to the value of pristine graphene. Both the recovering process of the Dirac point and the increasing resistivity are governed by Redox coupling processes. Molecular adsorption on graphene is induced by transferring electrons from graphene to environmental molecules such as H_2O and O_2, which induces carrier scattering in graphene. Another remarkable characteristic property of graphene devices resulting from electron irradiation is hysteresis in the transport properties. While the electron irradiated graphene stays in vacuum, it reveals hysteresis. As a result of exposure of graphene to ambient air, the magnitude of the hysteresis decreases and finally disappears. Furthermore, annealing at 200°C for a short period of time removes the hysteresis. We consider that the hysteresis which appeared in graphene as a result of electron irradiation is the result of interactions

between graphene and adsorbates molecules near graphene. The electronic state of molecules such as H_2O and O_2 possibly changes as a result of backscattered or secondary electrons. In particular, these molecules can be ionized or capture electrons with energy ranging from 1eV to 100eV. However, it is difficult to determine which species induce hysteresis in graphene because the energy of secondary electrons is comparable to changes in the electronic states of those molecules.

A study to investigate the effect of electron irradiation on PMMA/graphene bilayers was also presented in a previous chapter. While the back bone structure of PMMA is broken by electron irradiation, gas atoms such as hydrogen are also generated. The appearance of the Raman 'D' band indicates that atoms or molecules are tightly bound. In addition, the transport properties are degraded by electron irradiation depending on the electron dosage irradiated on graphene. The deterioration of the transport properties is the results of molecular adsorption on graphene which is in agreement with the observed Raman spectrum. We suggest that the atoms or molecules adsorbed on graphene are gaseous atoms generated during the depolymerization process of PMMA.

Although adsorbed molecules on graphene as a result of electron irradiation are observed by AFM, the atomic scale landscape is not known yet. In addition, AFM measurements were conducted in ambient condition, so no information on the morphology of graphene after electron irradiation in vacuum is available. In order to investigate the origin of the hysteresis and the species which induce hysteresis, in-situ

transport measurements and Scanning Tunneling Microscope (STM) experiments are required. After irradiation of graphene by an electron beam, the transport properties and surface morphology at the atomic scale must be conducted while precisely controlled molecules are added to the vacuum chamber. Because environmental molecules such as water and oxygen donate or capture electrons as a result of scattering with low energy electrons, we expect that electronically polarized molecules which cause the hysteresis may be observable by STM.

NOMENCLATURE

FET	Field Effect Transistor
EBL	Electron Beam Lithography
SEM	Scanning Electron Microscopy
STM	Scanning Tunneling Microscopy
AFM	Atomic Force Microscopy
IPA	Isopropyl alcohol
PMMA	Poly Methyl Methacrylate
XPS	X-ray Photoemission Spectroscopy
CNT	Carbon NanoTube
AFM	Atomic Force Microscopy
Redox	Reduction-Oxidation

REFERENCES

1. Fradkin, E., “Critical-Behavior of Disordered Degenerate Semiconductors. II. Spectrum and Transport-Properties in Mean-Field Theory”, Phys. Rev. B, **33**, 3263 (1986)

2. Wallace, P. R., “The Band Theory of Graphite”, Phys. Rev., **71**, 476 (1947).

3. Mermin, N. D., “Crystalline Order in 2 Dimensions”, Phys. Rev., **176**, 250 (1968).

4. Novoselov, K. S., Jiang, D., Schedin, F., Booth, T. J., Khotkevich, V. V., Morozov, S. V., Geim, A. K., “Two-dimensional Atomic Crystals”, PNAS, **102**, 10451 (2005).

5. Landau, L. D., Lifshitz, E. M., “Statistical Physics”, Butterworth-Heinemann Pergamon, Oxford (1980), ISBN: 0750633727.

6. Novoselov, K. S., Geim, A. K., Morozov, S. V., Jiang, D., Zhang, Y., Dubonos, S. V., Grigorieva, I. V., Firsov, A. A., “Electric Field Effect in Atomically Thin Carbon Films”, Science, **306**, 666 (2004).

7. Bolotin, K. I., Sikes, K. J., Jiang, Z., Klima, M., Fudenberg, G., Hone, J., Kim, P., Stormer, H. L., “Ultrahigh Electron Mobility in Suspended Graphene”, Solid State Commun., **146**, 351 (2008).

8. Ki, D. K., Morpurgo, A. F., “High-quality Multiterminal Suspended Graphene Devices”, Nano Lett., **13**, 5165 (2013)

9. Lee, C., Wei, X., Kysar, J. W., Hone, J., “Measurement of the Elastic Properties and Intrinsic Strength of Monolayer Graphene”, Science, **321**, 385 (2008).

10. Lee, G. H., Cooper, R. C., An, S. J., Lee, S., van der Zande, A., Petrone, N., Hammerberg, A. G., Lee, C., Crawford, B., Oliver, W., Kysar, J. W., Hone, J., “High-strength Chemical-vapor-deposited Graphene and Grain Boundaries”, Science, **340**, 1073 (2013).

11. Chen, C., Rosenblatt, S., Bolotin, K. I., Kalb, W., Kim, P., Kymissis, I., Stormer, H. L., Heinz, T. F., Hone. J., “Performance of Monolayer Graphene Nanomechanical Resonators with Electrical Readout”, Nature Naontech, **4**, 861 (2009).

12. Fuhrer, M. S., Lau, C. N., MacDonald, A. H., “Graphene: Materially Better Carbon”, MRS Bulletin, **35**, 289, (2010).

13. Balandin, A. A., Ghosh, S., Bao, W. Z., Calizo, I., Teweldebrhan, D., Miao, F., Lau, C. N., “Superior Thermal Conductivity of Single-layer Graphene”, Nano Lett., **8**, 902 (2008).

14. Pop, E., Mann, D., Wang, Q., Goodson, K. E., Dai, H. J., “Thermal Conductance of an Individual Single-wall Carbon Nanotube above Room Temperature”, Nano Lett., **6**, 96 (2006).

15. Kuzmenko, A. B., van Heumen, E., Carbone, F., van der Marel, D., “Universal Optical Conductance of Graphite”, Phys. Rev. Lett., **100**, 117401 (2008).

16. Blake, P., Hill, E. W., Neto, A. H. C., Novoselov, K. S., Jiang, D., Yang, R., Booth, T. J., Geim, A. K., “Making Graphene Visible”, Appl. Phys. Lett., **91**, 063124 (2007).

17. Elias, D. C., Nair, R. R., Mohiuddin, T. M. G., Morozov, S. V., Blake, P., Halsall, M. P., Ferrari, A. C., Boukhvalov, D. W., Katsnelson, M. I., Geim, A. K., Novoselov, K. S., “Control of Graphene's Properties by Reversible Hydrogenation: Evidence for Graphane”, Science, **323**, 610 (2009).

18. Kim, B. H., Hong, S. J., Baek, S. J., Jeong, H. Y., Park, N., Lee, M., Lee, S. W., Park, M., Chu, S. W., Shin, H. S., Lim, J., Lee, J. C., Jun, Y., Park, Y. W., “N-type Graphene Induced by Dissociative H-2 Adsorption at Room Temperature”, Sci. Rep., **2**, 690 (2012).

19. Sun, Z. Z., Pint, C. L., Marcano, D. C., Zhang, C. G., Yao, J., Ruan, G. D., Yan, Z., Zhu, Y., Hauge, R. H., Tour, J. M., “Towards Hybrid Superlattices in Graphene”, Nat. Commun., **2**, 559 (2011).

20. Luo, Z. Q., Yu, T., Kim, K. J., Ni, Z. H., You, Y. M., Lim, S., Shen, Z. X., Wang, S. Z., Lin, J. Y., “Thickness-Dependent Reversible Hydrogenation of Graphene Layers”, ACS Nano, **3**, 1781 (2009).

21. Luo, Z. Q., Shang, J. Z., Lim, S. H., Li, D. H., Xiong, Q. H., Shen, Z. X., Lin, J. Y., Yu, T., “Modulating the Electronic Structures of Graphene by Controllable Hydrogenation”, Appl. Phys. Lett., **97**, 233111 (2010).

22. Schedin, F., Geim, A. K., Morozov, S. V., Hill, E. W., Blake, P., Katsnelson, M. I., Novoselov, K. S., “Detection of Individual Gas Molecules Adsorbed on Graphene”, Nature Mater., **6**, 652 (2007).

23. Geim, A.K. and K.S. Novoselov, “The Rise of Graphene”, Nature Mater., **6**, 183 (2007).

24. Subrahmanyam, K. S., Kumar, P., Maitra, U., Govindaraj, A., Hembram, K. P. S. S., Waghmare, U. V., Rao, C. N. R., “Chemical Storage of Hydrogen in Few-layer Graphene”, PNAS, **108**, 2674 (2011).

25. Shao, Y. Y., Wang, J., Wu, H., Liu, J., Aksay, I. A., Lin, Y. H., “Graphene Based Electrochemical Sensors and Biosensors: A Review”, Electroanalysis, **22**, 1027 (2010).

26. Datta, S., ECE 495N Lecture 21: Graphene Bandstructure (2008), https://nanohub.org/resources/5710, Last date accessed: 10th July, 2014.

27. Ashcroft, N.W. and Mermin, N.D., “Solid State Physics”, International edition, Holt, Rinehart and Winston, New York Brooks Cole (1976), ISBN: 0030839939.

28. Merzbacher, E., “Quantum Mechanics”, 3rd edition, New York, Wiley (1988), ISBN: 1887021.

29. Liboff, L. R., “Introduction to Quantum Mechanics”, 3rd edition, Addison-Wesley (1980), ISBN: 0201122219.

30. Katsnelson, M. I., Novoselov, K. S., Geim, A. K., “Chiral Tunneling and the Klein Paradox in Graphene”, Nature Phys., **2**, 620 (2006).

31. Su, R. K., Siu, G. G., Chou, X., “Barrier Penetration and Klein Paradox”, J. Phys. A, **26**, 1001 (1993).

32. Cheianov, V. V. and Fal'ko, V. I., “Selective Transmission of Dirac Electrons and Ballistic Magnetoresistance of n-p Junctions in Graphene”, Phys. Rev. B, **74**, 041403 (2006).

33. Low, T. and Appenzeller, J., “Electronic Transport Properties of a Tilted Graphene p-n Junction”, Phys. Rev. B, **80**, 155406 (2009).

34. Das Sarma, S., Adam, S., Hwang, E. H., Rossi, E., “Electronic Transport in Two-Dimensional Graphene”, Rev. Mod. Phys., **83**, 407 (2011).

35. Novoselov, K. S., Geim, A. K., Morozov, S. V., Jiang, D., Katsnelson, M. I., Grigorieva, I. V., Dubonos, S. V., Firsov, A. A., “Two-dimensional Gas of Massless Dirac Fermions in Graphene”, Nature, **483**, 197 (2005).

36. Berry, M. V. and Mondragon, R. J., "Neutrino Billiards - Time-Reversal Symmetry-Breaking without Magnetic-Fields", Proceedings of the Royal Society of London Series a-Mathematical Physical and Engineering Sciences, **412**, 53 (1987).

37. Tworzydlo, J., Trauzettel, B., Titov, M., Rycerz, A., Beenakker, C. W. J., "Sub-Poissonian Shot Noise in Graphene", Phys. Rev. Lett., **96**, 246802 (2006).

38. Bostwick, A., McChesney, J., Ohta, T., Rotenberg, E., Seyller, T., Horn, K., "Experimental Studies of the Electronic Structure of Graphene", Progress in Surf. Sci., **84**, 380 (2009).

39. Morozov, S. V., Novoselov, K. S., Katsnelson, M. I., Schedin, F., Elias, D. C., Jaszczak, J. A., Geim, A. K., "Giant Intrinsic Carrier Mobilities in Graphene and Its Bilayer", Phys. Rev. Lett., **100**, 016602 (2008).

40. Bolotin, K. I., Sikes, K. J., Hone, J., Stormer, H. L., Kim, P., "Temperature-Dependent Transport in Suspended Graphene", Phys. Rev. Lett., **101**, 096802 (2008).

41. Jang, C., Adam, S., Chen, J. H., Williams, D., Das Sarma, S., Fuhrer, M. S., "Tuning the Effective Fine Structure Constant in Graphene: Opposing Effects of Dielectric Screening on Short- and Long-range Potential Scattering", Phys. Rev. Lett., **101**, 146805 (2008).

42. Huard, B., Stander, N., Sulpizio, J. A., Goldhaber-Gordon, D., "Evidence of the Role of Contacts on the Observed Electron-hole Asymmetry in Graphene", Phys. Rev. B, **78**, 121402 (2008).

43. Hong, X., Zou, K., Zhu, J., "Quantum Scattering Time and Its Implications on Scattering Sources in Graphene", Phys. Rev. B, **80**, 241415 (2009).

44. Shon, N. H. and Ando, T., "Quantum Transport in Two-dimensional Graphite System", J. Physical Society of Japan, **67**, 2421 (1998).

45. Trushin, M. and Schliemann, J., "Conductivity of Graphene: How to Distinguish between Samples with Short- and Long-range Scatterers", EPL, **83**, 17001 (2008).

46. Chen, J. H., Jang, C., Adam, S., Fuhrer, M. S., Williams, E. D., Ishigami, M., "Charged-impurity Scattering in Graphene", Nature Phys., **4**, 377 (2008).

47. Katsnelson, M. I., Guinea, F., Geim, A. K., "Scattering of Electrons in Graphene by Clusters of Impurities", Phys. Rev. B, **79**, 195426 (2009).

48. Nomura, K. and MacDonald, A. H., “Quantum Transport of Massless Dirac Fermions”, Phys. Rev. Lett., **98**, 076602 (2007).

49. Ando, T., “Screening Effect and Impurity Scattering in Monolayer Graphene”, J. Physical Society of Japan, **75**, 074716 (2006).

50. Cheianov, V. V. and Fal'ko, V. I., “Friedel Oscillations, Impurity Scattering, and Temperature Dependence of Resistivity in Graphene”, Phys. Rev. Lett., **97**, 226801 (2006).

51. Hwang, E. H., Adam, S., Das Sarma, S., “Carrier Transport in Two-dimensional Graphene Layers”, Phys. Rev. Lett., **98**, 186806 (2007).

52. Adam, S., Hwang, E. H., Galitski, V. M., Das Sarma, S., “A self-consistent Theory for Graphene Transport”, PNAS, **104**, 18392 (2007).

53. Castro Neto, A. H., Guinea, F., Peres, N. M. R., Novoselov, K. S., Geim, A. K., “The Electronic Properties of Graphene”, Rev. Mod. Phys., **81**, 109 (2009).

54. Yan, X. Z., Romiah, Y., Ting, C. S., “Electric Transport Theory of Dirac Fermions in Graphene”, Phys. Rev. B, **77**, 125409 (2008).

55. Trushin, M. and Schliemann, J., “Minimum Electrical and Thermal Conductivity of Graphene: A Quasiclassical Approach”, Phys. Rev. Lett., **99**, 216602 (2007).

56. Stauber, T., Peres, N. M. R., Guinea, F., “Electronic Transport in Graphene: A Semiclassical Approach Including Midgap States”, Phys. Rev. B, **76**, 205423 (2007).

57. Adam, S., Brouwer, P. W., Das Sarma, S., “Crossover from Quantum to Boltzmann Transport in Graphene”, Phys. Rev. B, **79**, 201404 (2009).

58. Sun, P. Z., Zhu, M., Wang, K. L., Zhong, M. L., Wei, J. Q., Wu, D. H., Cheng, Y., Zhu, H. W., “Photo Induced Molecular Desorption From Graphene Films”, Appl. Phys. Lett. **101**, 053107 (2012).

59. Lin, Y. J. and Zeng, J. J., “Tuning the Work Function of Graphene by Ultraviolet Irradiation”, Appl. Phys. Lett., **102**, 183120 (2013).

60. Luo, Z. T., Pinto, N. J., Davila, Y., Johnson, A. T. C., “Controlled Doping of Graphene Using Ultraviolet Irradiation”, Appl. Phys. Lett., **100**, 253108 (2012).

61. Hicks, J., Arora, R., Kenyon, E., Chakraborty, P. S., Tinkey, H., Hankinson, J., Berger, C., de Heer, W. A., Conrad, E. H., Cressler, J. D., "X-ray Radiation Effects in Multilayer Epitaxial Graphene", Appl. Phys. Lett., **99**, 232102 (2011).

62. Kim, K. J., Choi, J. H., Lee, H., Lee, H. K., Kang, T. H., Han, Y. H., Lee, B. C., Kim, S., Kim, B. , "Effects of 1 MeV Electron Beam Irradiation on Multilayer Graphene Grown on 6H-SiC(0001)", J. Phys. Chem. C,, **112**, 13062 (2008).

63. Chen, J. H., Cullen, W. G., Jang, C., Fuhrer, M. S., Williams, E. D., "Defect Scattering in Graphene", Phys. Rev. Lett., **102**, 236805 (2009).

64. Ugeda, M. M., Brihuega, I., Guinea, F., Gomez-Rodriguez, J. M., "Missing Atom as a Source of Carbon Magnetism", Phys. Rev. Lett., **104**, 096804 (2010).

65. Hahn, J. R., Kang, H., Song, S., Jeon, I. C., "Observation of Charge Enhancement Induced by Graphite Atomic Vacancy: A Comparative STM and AFM Study", Phys. Rev. B, **53**, R1725 (1996).

66. Hashimoto, A., Suenaga, K., Gloter, A., Urita, K., Iijima, S., "Direct Evidence for Atomic Defects in Graphene Layers", Nature, **430**, 870 (2004).

67. Banhart, F., "Irradiation Effects in Carbon Nanostructures", Reports on Progress in Physics, **62**, 1181 (1999).

68. Robertson, A. W., Allen, C. S., Wu, Y. A., He, K., Olivier, J., Neethling, J., Kirkland, A. I., Warner, J. H., "Spatial Control of Defect Creation in Graphene at the Nanoscale", Nature Commun., **3**, 1144, (2012).

69. Zhu, W. P., Wang, H. T., Yang, W.," Evolution of Graphene Nanoribbons under Low-voltage Electron Irradiation", Nanoscale, **4**, 4555 (2012).

70. Xu, M. S., Fujita, D., Hanagata, N., "Monitoring Electron-Beam Irradiation Effects on Graphene by Temporal Auger Electron Spectroscopy", Nanotechnology, **21**, 265705 (2010).

71. Song, B., Schneider, G. F., Xu, Q., Pandraud, G., Dekker, C., Zandbergen, H., "Atomic-Scale Electron-Beam Sculpting of Near-Defect-Free Graphene Nanostructures", Nano Lett., **11**, 2247 (2011).

72. Xu, M. S., Fujita, D., Gao, J. H., Hanagata, N., "Auger Electron Spectroscopy: A Rational Method for Determining Thickness of Graphene Films", ACS Nano, **5**, 2937 (2010).

73. Tao, L., Qiu, C. Y., Yu, F., Yang, H. C., Chen, M. J., Wang, G., Sun, L. F., "Modification on Single-Layer Graphene Induced by Low-Energy Electron-Beam Irradiation", J. Phys. Chem. C, **117**, 10079 (2013).

74. Borrnert, F., Fu, L., Gorantla, S., Knupfer, M., Buchner, B., Rummeli, M. H., "Programmable Sub-nanometer Sculpting of Graphene with Electron Beams", ACS Nano, **6**, 10327 (2012).

75. Kotakoski, J., Santos-Cottin, D., Krasheninnikov, A. V., "Stability of Graphene Edges under Electron Beam: Equilibrium Energetics versus Dynamic Effects", ACS Nano, **6**, 671 (2012).

76. Teweldebrhan, D. and Balandin, A. A., "Modification of Graphene Properties due to Electron-Beam Irradiation", Appl. Phys. Lett., **94**, 013101 (2009).

77. Murakami, K., Kadowaki, T., Fujita, J., "Damage and Strain in Single-layer Graphene Induced by Very-low-energy Electron-beam Irradiation", Appl. Phys. Lett., **102**, 043111 (2013).

78. Fischbein, M. D. and Drndic, M., "Electron Beam Nanosculpting of Suspended Graphene Sheets", Appl. Phys. Lett., **93**, 113107 (2008).

79. He, Y. H., Wang, L., Chen, X. L., Wu, Z. F., Li, W., Cai, Y., Wang, N., "Modifying Electronic Transport Properties of Graphene by Electron Beam Irradiation", Appl. Phys. Lett., **99**, 033109 (2011).

80. Go, H., Kwak, J., Jeon, Y., Kim, S. D., Lee, B. C., Kang, H. S., Ko, J. H., Kim, N., Kim, B. K., Yoo, J. W., Kim, S., Kim, Y. W., Kwon, S. Y., Park, K., "Low-temperature Formation of Epitaxial Graphene on 6H-SiC induced by Continuous Electron Beam Irradiation", Appl. Phys. Lett., **101**, 092105 (2012).

81. Childres, I., Jauregui, L. A., Foxe, M., Tian, J. F., Jalilian, R., Jovanovic, I., Chen, Y. P., "Effect of Electron-Beam Irradiation on Graphene Field Effect Devices", Appl. Phys. Lett., **97**, 173109 (2010).

82. Yang, D. Q. and Sacher, E., "Carbon 1s X-ray Photoemission Line Shape Analysis of Highly Oriented Pyrolytic Graphite: The Influence of Structural Damage on Peak Asymmetry", Langmuir, **22**, 860 (2006).

83. Jones, J. D., Mahajan, K. K., Williams, W. H., Ecton, P. A., Mo, Y., Perez, J. M., "Formation of Graphane and Partially Hydrogenated Graphene by Electron Irradiation of Adsorbates on Graphene", Carbon, **48**, 2335 (2010).

84. Withers, F., Bointon, T. H., Dubois, M., Russo, S., Craciun, M. F., "Nanopatterning of Fluorinated Graphene by Electron Beam Irradiation", Nano Lett., **11**, 3912 (2011).

85. Woo, S. O. and Teizer, W., "The Effect of Electron Induced Hydrogenation of Graphene on Its Electrical Transport Properties", Appl. Phys. Lett., **103**, 041603 (2013).

86. Ferrari, A. C., Meyer, J. C., Scardaci, V., Casiraghi, C., Lazzeri, M., Mauri, F., Piscanec, S., Jiang, D., Novoselov, K. S., Roth, S., Geim, A. K., "Raman Spectrum of Graphene and Graphene Layers", Phys. Rev. Lett., **97**, 187401 (2006).

87. Vieu, C., Carcenac, F., Pepin, A., Chen, Y., Mejias, M., Lebib, A., Manin-Ferlazzo, L., Couraud, L., Launois, H., "Electron Beam Lithography: Resolution Limits and Applications", Appl. Surf. Sci., **164**, 111 (2000).

88. Graf, D., Molitor, F., Ensslin, K., Stampfer, C., Jungen, A., Hierold, C., Wirtz, L., "Spatially Resolved Raman Spectroscopy of Single- and Few-layer Graphene", Nano Lett., **7**, 238 (2007).

89. Wang, H. M., Wu, Y. H., Cong, C. X., Shang, J. Z., Yu, T., "Hysteresis of Electronic Transport in Graphene Transistors", ACS Nano, **4**, 7221 (2010).

90. Tuinstra, F. and Koenig, J. L., "Raman Spectrum of Graphite", J. Chem. Phys., **53**, 1126 (1970).

91. Ferrari, A. C., "Raman Spectroscopy of Graphene and Graphite: Disorder, Electron-Phonon Coupling, Doping and Nonadiabatic Effects", Solid State Commun., **143**, 47 (2007).

92. Magonov, S. N., Elings, V., Whangbo, M. H., "Phase Imaging and Stiffness in Tapping-Mode Atomic Force Microscopy", Surf. Sci., **375**, L385 (1997).

93. Arya, Atam Parkash, "Introduction to Classical Mechanics", 2nd edition, Benjamin-Cummings Pub Co (1997), ISBN: 0135052238.

94. Pethica, J. B. and Oliver, W. C., "Tip Surface Interactions in STM and AFM", Physica Scripta, **T19a**, 61 (1987).

95. Nagao, E. and Dvorak, J. A., "Phase Imaging by Atomic Force Microscopy: Analysis of Living Homoiothermic Vertebrate Cells", Biophysical Journal, **76**, 3289 (1999).

96. Levesque, P. L., Sabri, S. S., Aguirre, C. M., Guillemette, J., Siaj, M., Desjardins, P., Szkopek, T., Martel, R., "Probing Charge Transfer at Surfaces Using Graphene Transistors", Nano Lett., **11**, 132 (2011).

97. Romero, H. E., Shen, N., Joshi, P., Gutierrez, H. R., Tadigadapa, S. A., Sofo, J. O., Eklund, P. C., "N-Type Behavior of Graphene Supported on Si/SiO_2 Substrates", ACS Nano, **2**, 2037 (2008).

98. Joshi, P., Romero, H. E., Neal, A. T., Toutam, V. K., Tadigadapa, S. A., "Intrinsic Doping and Gate Hysteresis in Graphene Field Effect Devices Fabricated on SiO_2 Substrates", Journal of Physics-Condensed Matter, **22**, 334214 (2010).

99. Kim, W., Javey, A., Vermesh, O., Wang, O., Li, Y. M., Dai, H. J., "Hysteresis Caused by Water Molecules in Carbon Nanotube Field-Effect Transistors", Nano Lett., **3**, 193 (2003)/

100. Kalon, G., Shin, Y. J., Truong, V. G., Kalitsov, A., Yang, H., "The Role of Charge Traps in Inducing Hysteresis: Capacitance-voltage Measurements on Top Gated Bilayer Graphene", Appl. Phys. Lett., **99**, 083109 (2011).

101. Lafkioti, M., Krauss, B., Lohmann, T., Zschieschang, U., Klauk, H., von Klitzing, K., Smet, J. H., "Graphene on a Hydrophobic Substrate: Doping Reduction and Hysteresis Suppression under Ambient Conditions", Nano Lett., **10**, 1149 (2010).

102. Lohmann, T., von Klitzing, K., Smet, J. H., "Four-Terminal Magneto-Transport in Graphene p-n Junctions Created by Spatially Selective Doping", Nano Lett., **9**, 1973 (2009).

103. Oh, J. H., Lee, H. W., Mannsfeld, S., Stoltenberg, R. M., Jung, E., Jin, Y. W., Kim, J. M., Yoo, J. B., Bao, Z. N., "Solution-processed, High-performance n-channel Organic Microwire Transistors", PNAS, **106**, 6065 (2009).

104. Ennis, C. P. and Kaiser, R. I., "Mechanistical Studies on the Electron-induced Degradation of Polymers: Polyethylene, Polytetrafluoroethylene, and Polystyrene", Phys. Chem. Chem. Phys., **12**, 14884 (2010).

105. Ryu, S., Han, M. Y., Maultzsch, J., Heinz, T. F., Kim, P., Steigerwald, M. L., Brus, L. E., "Reversible Basal Plane Hydrogenation of Graphene", Nano Lett., **8**, 4597 (2008).

106. Jones, J. D., Hoffmann, W. D., Jesseph, A. V., Morris, C. J., Verbeck, G. F., Perez, J. M., "On the Mechanism for Plasma Hydrogenation of Graphene", Appl. Phys. Lett., **97**, 233104 (2010).

107. Puster, M., Rodriguez-Manzo, J. A., Balan, A., Drndic, M., "Toward Sensitive Graphene Nanoribbon-Nanopore Devices by Preventing Electron Beam-Induced Damage", ACS Nano, **7**, 11283 (2013).

108. Schneider, G. F., Kowalczyk, S. W., Calado, V. E., Pandraud, G., Zandbergen, H. W., Vandersypen, L. M. K., Dekker, C., "DNA Translocation through Graphene Nanopores", Nano Lett., **10**, 3163 (2010).

109. Aguirre, C. M., Levesque, P. L., Paillet, M., Lapointe, F., St-Antoine, B. C., Desjardins, P., Martel, R., "The Role of the Oxygen/Water Redox Couple in Suppressing Electron Conduction in Field-Effect Transistors", Adv. Mater., **21**, 3087 (2009).

110. Chakrapani, V., Angus, J. C., Anderson, A. B., Wolter, S. D., Stoner, B. R., Sumanasekera, G. U., "Charge Transfer Equilibria between Diamond and an Aqueous Oxygen Electrochemical Redox Couple", Science, **318**, 1424 (2007).

111. Farmer, D. B., Golizadeh-Mojarad, R., Perebeinos, V., Lin, Y. M., Tulevski, G. S., Tsang, J. C., Avouris, P., "Chemical Doping and Electron-Hole Conduction Asymmetry in Graphene Devices", Nano Lett., **9**, 388 (2009).

112. Ferrari, A. C. and Robertson, J., "Interpretation of Raman Spectra of Disordered and Amorphous Carbon", Phys. Rev. B, **61**, 14095 (2000).

113. Yu, Y. J., Zhao, Y., Ryu, S., Brus, L. E., Kim, K. S., Kim, P., "Tuning the Graphene Work Function by Electric Field Effect", Nano Lett., **9**, 3430 (2009).

114. Raseong Kim and Mark Lundstrom, "Notes on Fermi-Dirac Integrals (3rd Edition)", https://nanohub.org/resources/5475 (2008), Last date accessed: 10th July, 2014.

115. Tan, Y. W., Zhang, Y., Bolotin, K., Zhao, Y., Adam, S., Hwang, E. H., Das Sarma, S., Stormer, H. L., Kim, P., "Measurement of Scattering Rate and Minimum Conductivity in Graphene", Phys. Rev. Lett., **99**, 246803 (2007).

116. Cho, C., Lee, Y. G., Jung, U., Kang, C. G., Lim, S., Hwang, H. J., Choi, H., Lee, B. H., "Correlation between the Hysteresis and the Initial Defect Density of Graphene", Appl. Phys. Lett., **103**, 083110 (2013).

117. Dan, Y. P., Lu, Y., Kybert, N. J., Luo, Z. T., Johnson, A. T. C., "Intrinsic Response of Graphene Vapor Sensors", Nano Lett., **9**, 1472 (2009).

118. Liao, Z. M., Han, B. H., Zhou, Y. B., Yu, D. P., "Hysteresis Reversion in Graphene Field-Effect Transistors", J. Chem. Phys., **133**, 044703 (2010).

119. Klarskov, M. B., Dam, H. F., Petersen, D. H., Hansen, T. M., Lowenborg, A., Booth, T. J., Schmidt, M. S., Lin, R., Nielsen, P. F., Boggild, P., "Fast and Direct Measurements of the Electrical Properties of Graphene Using Micro Four-point probes", Nanotechnology, **22**, 445702 (2011)

120. Lee, J. S., Ryu, S., Yoo, K., Choi, I. S., Yun, W. S., Kim, J., "Origin of Gate Hysteresis in Carbon Nanotube Field-Effect Transistors", J. Chem. Phys. C, **111**, 12504 (2007).

121. Thomas, J. H. and Feigl, F. J., "Electron Trapping Levels in Silicon Dioxide Thermally Grown on Silicon", J. Phys. Chem. Solids, **33**, 2197 (1972).

122. Kalita, H., Harikrishnan, V., Shinde, D. B., Pillai, V. K., Aslam, M., "Hysteresis and Charge Trapping in Graphene Quantum Dots", Appl. Phys. Lett., **102**, 143104 (2013).

123. Itikawa, Y. and Mason, N., "Cross Sections for Electron Collisions with Water Molecules", J. Phys. Chem. Ref. Data, **34**, 1 (2005).

124. Itikawa, Y., "Cross Sections for Electron Collisions with Oxygen Molecules", J. Phys. Chem. Ref. Data, **38**, 1 (2009).